A STUDY OF FATIGUE CRACK INITIATION AND EARLY PROPAGATION

by

© **Zhen Hua Zhai**

Mechanical Engineering Department
McGill University
Montreal, Canada

A Thesis submitted to the Faculty of Graduate Studies and Research
in partial fulfillment of the requirements for the degree of
Doctor of Philosophy.

August, 1988

To:

Danny, Hou-Ren, Xiu-Tian, Xin-Hua, Wei-Hua, Jian-Hua, Ai-Hua,
The People's Republic of China.

Abstract

This thesis proposes a quantitative model of fatigue crack initiation and early propagation based on a plastic strain intensity factor ΔK_p. In this model, the crack growth rate in the initiation region is simplified as a straight line on the log-log scale of da/dN versus ΔK_p curve. A turning point which divides crack growth into the initiation and propagation regions is introduced as the plastic crack propagation threshold, ΔK_{pth}, whose value is determined by the plastic crack propagation threshold in the ΔJ-integral form, $\sqrt{\Delta J \cdot E_{pth}}$. The crack propagation style in the initiation region up to the plastic crack propagation threshold is Stage I propagation. This thesis also proposes a Stage I crack propagation model for cylindrical specimens which consists of a model of sub-microcrack propagation prior to the sub-threshold and a model of the subsequent microcrack propagation. Crack profile changes and closure effects in the initiation region are also qualitatively proposed. The results of an experimental study carried out on smooth cylindrical specimens of polycrystalline OFHC copper at room temperature are compared with the proposed models. The coated and shadowed replicas viewed by SEM traced a fatal or main surface crack in a specimen back to a size of less than one micron. A combination of the replication technique and post-mortem specimen surface and fractographic surface examination by SEM provided good information of crack initiation and Stage I propagation. The results support the proposed models. The integration of the crack growth rate as a function of the plastic strain intensity factor yields a fatigue crack initiation life estimate whose error is less that 5%. For comparison, the experimental data presented in this paper are also discussed on the basis of ΔK and ΔK_{eff} parameters proposed by other researchers.

Résumé

Cette thèse propose un modèle quantitatif d'amorçage de fêlure par fatigue et de propagation hâtive en se basant sur le coefficient d'intensité de l'effort exercé sur le plastique ΔK_p. Dans ce modèle, le taux d'accroissement de la fêlure dans la zone d'amorçage se trouve simplifié par une droite dans l'échelle de logarithmes (log-log) de da/dN versus la courbe ΔK_p. Un point tournant qui divise l'accroissement de la fêlure entre les points d'amorçage et de propagation représente le seuil de propagation de la fêlure dans le plastic ΔK_{pth} dont la valeur est déterminée par le seuil de propagation de la fêlure sous la forme intégrale-ΔJ: $\sqrt{\Delta J \cdot E}_{pth}$. Le type de propagation de la fêlure allant de la zone d'amorçage jusqu'au seuil de propagation de la fêlure du plastique constitue le stade I de la propagation. Cette thèse propose également un modèle de propagation de la fêlure au stade I pour les échantillons de forme cylindrique consistant d'un modèle de propagation de sous-microfêlures qui précède le stade de sous-seuil et d'un modèle répresentant la propagation des microfêlures subséquente. Les changements de profil de la fêlure et l'effet de clôture dans la zone d'amorçage sont aussi proposés de façon qualitative. Les résultats d'une étude expérimentale effectuée sur des échantillons lisses et de forme cylindrique de cuivre OFHC polycristallin à la température de la pièce sont comparés aux modèles proposés. Les repliques enrobées et ombragées visionnées par SEM ont provoqué une fêlure "fatale" ou principale sur la surface d'un échantillon mesurant moins qu'un micron. Une combinaison de la technique de réproduction et de la surface de l'échantillon "post-mortem" ainsi qu'une étude fractographique par SEM nous ont fourni de bons reseignements sur l'amorçage des fêlures et sur la propagation de celles-ci au stade I. Les résultats supportent les modèles proposés. L'intégration du taux d'accroissement de la fêlure

en tant que fonction du coefficient d'effort du plastique entraîne une estimation de vie d'amorçage de la fêlure qui comporte une erreur de moins de 5%. En guise de comparaison, l'information expérimentale présentée dans ce document est également traitée en se basant sur les paramètres ΔK et ΔK_{eff} déjà proposés par d'autres chercheurs.

Acknowledgement

Most sincere gratitude to the author's supervisor, Prof. James W. Provan, for his guidance, technical and financial support thoughout this work. Special gratitude to the author's husband, Dr. Charles B. Daniels for his consistant encouragement and help in writing the thesis.

Thanks extend to Mr. Arthur Clement and his staff at the Machine Tool Laboratory for carefully preparing the specimens and Ph.D candidate Mr. Eduardo Turcott for his assistance in SEM techniques. Thanks are also due to Ms. Michelle Vanier for the french translation of the abstract.

Contents

List of Figures

List of Tables

Chapter 1

INTRODUCTION

1.1 Introduction

Fatigue is one of the major considerations in engineering design. In a large number of industrially important applications, in turbines, automobiles, ships and aircraft, fatigue fractures of machine parts leading to final failure are prevalent, in fact, they account for a major part in all service failures in most engineering structures and components. The fundamentals of fatigue failure are based upon the incipient fatigue crack evolution process. Under fatigue loading, either pre-existing flaws or cracks initiated from a smooth surface at a highly stressed region slowly grow to a critical length and then propagate to a larger size that leads to the failure of the machine component. The science of fatigue fracture mechanics researches the mechanisms and rules of fatigue crack initiation and propagation, so that fatigue failure can be monitored and kept under control.

The total fatigue life N is composed of crack initiation N_i and crack propagation

N_p lives. At the present time the ASTM standard E 647 [1] covers only the determination of constant load amplitude fatigue crack growth rates above $10^{-8} m/cycle$, using specimens that are sharp-notched. A typical crack propagation curve obtained from ASTM standard E 647 is schematically shown in Figure 1.1, where the vertical axis is the crack growth rate and the horizontal is either the stress intensity factor ΔK, commonly used in the Linear Elastic Fracture Mechanics (LEFM) analysis (for negligible small scale yielding around the crack tip), or the ΔJ-integral developed for Elastic Plastic Fracture Mechanics (EPFM) analysis (for limited plastic deformation around the crack tip).

In engineering terms, Region I in Figure 1.1 is the crack initiation region corresponding to a crack initiation life N_i, Region II the propagation region corresponding to a propagation life N_p, and Region III the fast propagation region before failure. According to LEFM methods, a crack propagation threshold exists as a material property for each material, below which the crack does not grow. This does not apply to smooth specimens, however, since how can a zero stress intensity factor crack, that leads to failure, initiate and propagate on a smooth surface of a specimen?

Until recently, Region II propagation has been the most popular topic in fatigue fracture studies. For many materials, the propagation behaviour in Region II has been found roughly to follow Paris-Erdogan Law [2], given by the following formula,

$$da/dN = F\,(\,\Delta K\,)^m, \tag{1.1}$$

where F and m are experimentally determined constants, a is the crack depth,

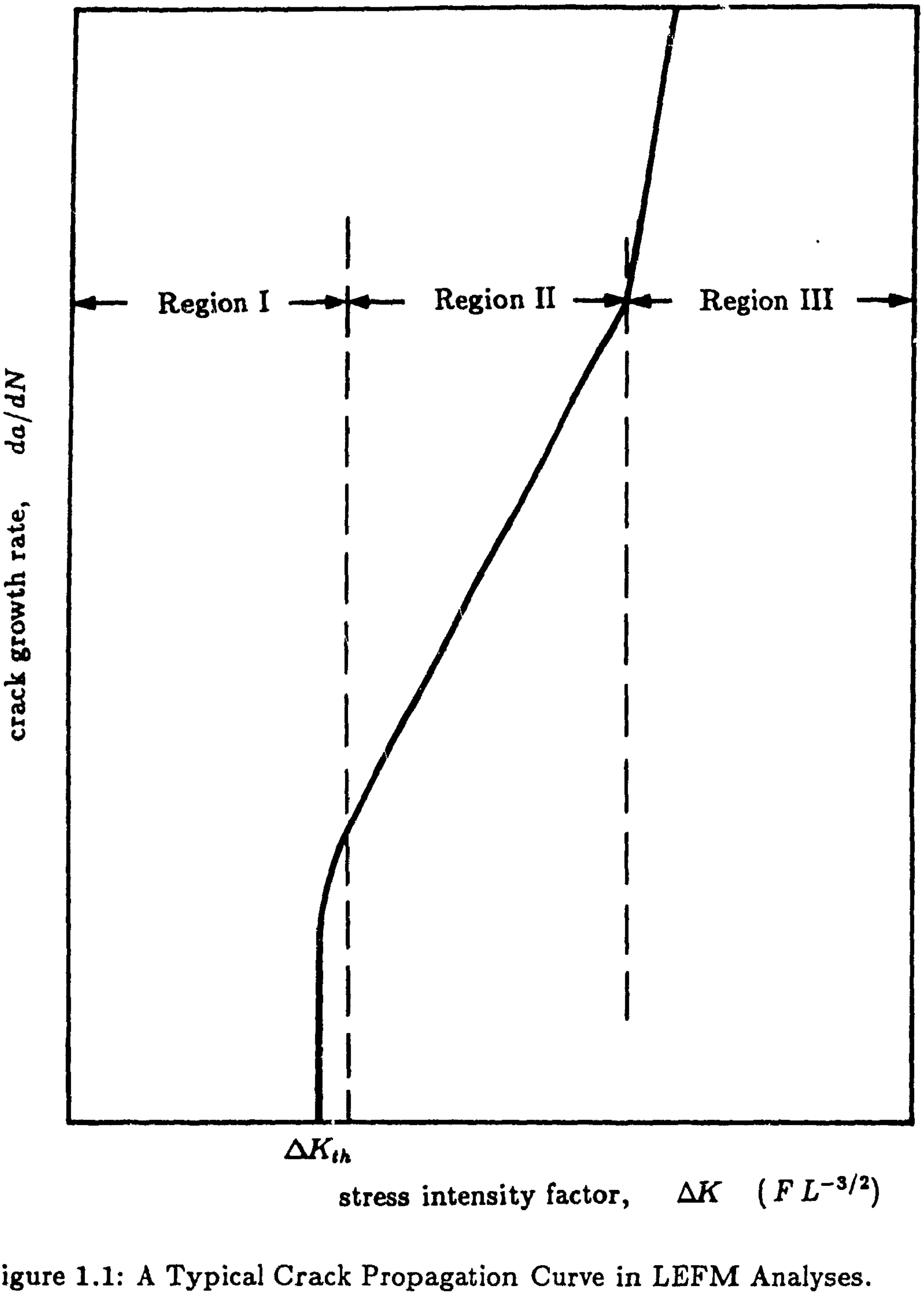

Figure 1.1: A Typical Crack Propagation Curve in LEFM Analyses.

da/dN the crack propagation rate, and ΔK the stress intensity level in LEFM analyses which is sometimes replaced by ΔJ-integral in EPFM analyses.

However, in practical engineering applications, the crack initiation part contributes significantly to the overall fatigue life. When the applied stress strain level is low, it takes more than 90% of the fatigue life to develop a crack [3,4]. Crack initiation studies remain a difficult problem not only because it is hard to follow a crack of microscopic dimensions but also because continuum mechanics cannot cope with the microscopic regime within which the material is inhomogeneous and the local stress strain is unevenly distributed in individual grains with complicated grain boundary interactions. Presently, crack initiation studies are mainly limited to the mechanism side while the mechanical engineering side is simply left behind. As yet, no empirical laws describe initiation, nor has an agreement ever been reached on a reasonable definition of crack initiation.

Even though the study of crack propagation is better developed than that of crack initiation, there are still problems. The curve and threshold values represented in Figure 1.1 are easily influenced by factors such as:

1. grain size — the curve shifts to the left and the crack propagation threshold becomes higher as the grain size increases [5,6],
2. stress ratio R — same changes in the curve as above as R decreases [7]-[9],
3. temperature — same changes in the curve as above as the temperature becomes higher [5]; (the fatigue branch especially developed for dealing high temperature fatigue is called creep fatigue), and

4. environment — the threshold increases as the environment becomes more active [9]; (the fatigue branch involving corrosive environment is called corrosion fatigue).

On the other hand, in the standard fatigue tests ASTM E466 [10] and E 606 [11] for obtaining the $S - N$ curve (stress or strain levels versus the total fatigue life N), the specimen designs are smooth cylindrical samples. It was believed that the results obtained from standard E 647 fatigue fracture tests of sharp notched specimens were applicable to crack propagation behaviour in smooth specimens, given that the applied stress-strain level at the tip of the notch equals the applied stress-strain level in the smooth specimen. But the applicability of the standard fatigue fracture tests to the more general situation, such as that with small flawed or smooth specimens, has been seriously challenged by the recent discoveries in "short crack" studies.

For over a decade, the so-called "short crack" problem has been formulated and studied. Despite inconsistent data, it has been observed that short cracks grow at stress intensity factor values lower than the threshold ΔK_{th} obtained from the standard fatigue fracture tests; and at the same stress intensity level, that short cracks usually grow faster than long through-thickness cracks. Researchers have been forced to reevaluate the results and recheck the experimental techniques in fatigue fracture mechanics and to seek better solutions.

Besides bringing out the limitations of conventional fatigue crack propagation tests, short crack problems are important in themselves in that they are closely related to crack initiation studies due to the small crack lengths involved. Actually, the results of short crack propagation studies reported in many articles can be considered as filling in the gap between Region II propagation and crack initiation mechanism studies. It is heartening to see that crack initiation research has been pushed one step forward by short crack studies; unfortunately the study is still at a preliminary stage and the published data much scattered. Moreover, most short crack observations have been made on artificial preflawed samples, while natural cracks initiating from smooth surfaces are expected to show much more short crack effect [12]. In the limited short crack literature concerning smooth surface, tension/tension tests involving thin plate samples [13,14] and reversed bending tests [15] prevail. The former often encounter a "corner effect", while the latter give results different from the axial tension and/or compression tests in the case of propagating cracks.

1.2 Research Objectives

Although, as mentioned above, there are problems throughout the field of fatigue studies, the most difficult are in the area of crack initiation. The ignorance of crack initiation and early propagation which is so important in fatigue fracture mechanics prompted the previously reported studies [16,17] by the author and is also the first and major motivation of this investigation.

The author believes that the choice between a smooth and a notched specimen is crucial in all fatigue studies, not only from the point of view of short crack propagation but also from the sense of crack initiation and the entire fatigue fracture process. A smooth sample demonstrates the complete process of crack initiation, propagation and fatigue failure, while a notched specimen hides part or all the crack initiation process by compressing it into a threshold region. Once the crack initiation and propagation behaviour is established in smooth specimens, a notched sample is likely to find its position in the crack propagation curve drawn from smooth samples, while a smooth sample is unlikely to fit in the crack propagation curve drawn from sharp notched specimens. Therefore, the second motivation for this research is to use smooth samples to study both crack initiation and propagation.

Finally, to account for the large scatter in fatigue data, statistical methods were also applied in fatigue analysis. The Provan reliability law was proposed [18] and partially verified by experiments. The discrepancy is attributed to a lack of knowledge of crack initiation. Therefore, the last motivation of this investigation is to help refine the Provan reliability law so that it may be modified in the future to take into account the statistical nature of fatigue crack initiation.

Specifically, the objectives of the present investigation are to use smooth cylindrical specimens under tension-compression loading:

1. to propose a realistic quantitative model that not only reflects the nature of fatigue crack initiation and microcrack propagation but also permits the development of a simplified rule for practical industrial and engineering purposes, so that the crack initiation life and the remaining life of machine parts can be predicted,

2. to define the crack propagation threshold and the critical crack length a_0 at initiation on a solid physical basis,

3. to propose systematic models of crack initiation and microcrack propagation mechanisms,

4. to carry out experiments that monitor the complete process of fatigue crack initiation and propagation so that the proposed models and definitions can be verified by analysing the experimental results both mechanically and metallurgically, and

5. to compare the existing short crack propagation models with the proposed model based on the experimental results analysis of this investigation.

1.3 Summary of Contents

A review of the existing theories and models in the field of crack initiation from both a metallurgical and mechanical point of view, and the developments in short crack propagation studies are presented in Chapter 2. Chapter 3 proposes and explains the mechanical model of crack initiation and propagation based on a new driving factor, ΔK_p, the Stage I propagation model consists of two models: the sub-microcrack initiation and nucleation model and the microcrack propagation model. The following Chapter gives the specimen design, test equipment, experimental technique, testing procedures, and some preliminary experimental results. Chapter 5 presents the results from: i) the computer controlled MTS tests; ii) the analysis of results are carried on in the following sequence: the stress intensity factor ΔK analysis, the ΔJ-integral analysis, the newly proposed plastic strain intensity factor ΔK_p and the proposed model analysis, and a modified ΔJ-integral method; and iii) the crack initiation and early propagation mechanism studies of both the replicas and post-mortem specimen surface and fractographic surface SEM eximination, each Section including a discussion whenever necessary. Finally, Chapter 6 presents the conclusions, original contributions and a discussion of future research.

Chapter 2

LITERATURE REVIEW OF FATIGUE CRACK INITIATION AND SHORT CRACK PROPAGATION

2.1 Introduction

For more than 100 years, researchers have been investigating why and how cracks initiate and cause failure of machine parts under repeated fatigue loading, what is the rule governing this phenomenon and how failure can be prevented by applying this rule to engineering design. Research concerning the first belongs to material science; it emphasizes the material microstructural changes from the metallurgical point of view. Research concerning the second belongs to mechanical engineering; it summarizes and formulates the basics of the phenomenon, so that engineers can use it in design.

Although the mechanical method is more practical, it has also long been recognized that a proper understanding of fatigue mechanisms should provide an efficient route both to improving the design of components to resist fatigue and to furnishing better technical methods for monitoring fatigue damage. Therefore, this Chapter reviews crack initiation first from a metallurgical viewpoint, then from the mechanical point of view, and at the end discusses the concept that short crack propagation is a subject closely related to crack initiation and early propagation.

2.2 Mechanisms of Crack Initiation and Early Propagation

2.2.1 Strain Hardening/Softening and the Cyclic Stress Strain Curve

The earliest modifications to the microstructure caused by fatigue loading are reflected macroscopically in the changes in the material flow properties, known as strain hardening or softening [19]-[21]. Depending on the initial state, the deformation resistance of most materials either decreases or increases. For a material hardened by the working process, or by other proper means for the purpose of strengthening the material, the maximum stress level becomes lower and lower at the same strain or plastic strain level, which is called strain softening [22]. For a material annealed to a certain degree, the stress level becomes higher and higher which is called strain hardening [22].

Typical hysteresis loop changes, as shown in Figure 2.1 [23], depict the strain hardening process for an annealed single copper crystal obtained from fatigue tests under constant plastic strain control. Under most of the loading conditions the softening or hardening process eventually gives way to a saturation stage when the stress is almost constant. The material spends a relatively long time in this stabilized state [24]. As can be seen also from Figure 2.1, the difference between each cycle becomes smaller and smaller as the cycle increases, reflecting the slowing down of the hardening speed.

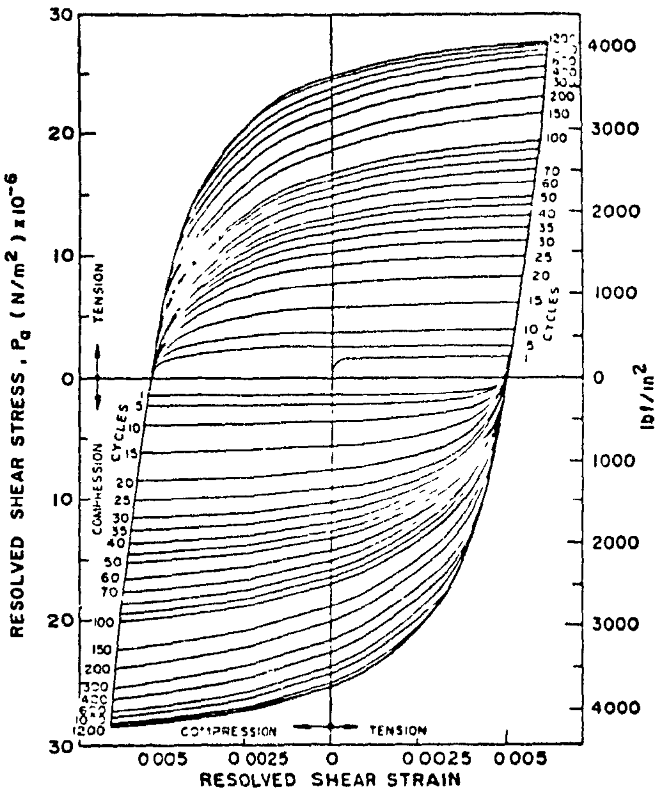

Figure 2.1: The Cyclic Hardening of an Annealed Copper Single Crystal. *ref* 23

During the process of strain hardening/softening, the dislocation structure changes rapidly to accommodate the change of the stress levels [25], and a fixed dislocation pattern is gradually formed. The subsequent cumulative dislocation movement in the dislocation structure leads to crack initiation, microcrack propagations, and final failure. By periodically annealing the specimen and keeping it in a work hardenable state, thereby destroying the fixed dislocation patterns, Alden and Bachofen [26] showed that crack nucleation can be prevented indefinitely.

For materials finally entering a saturation state, the corresponding saturation stresses can be obtained at different strain (or plastic strain) levels. By connecting these strains (or plastic strains) to the corresponding saturation stresses, a cyclic stress strain curve is obtained. The study of copper single crystals indicated that their cyclic stress-strain curves have three regions as shown in Figure 2.2 [27]. In the curve, Region B is known as the "plateau" where the stress remains almost constant as the strain varies. It is believed that in this region Persistent Slip Bands (PSBs) (to be discussed in more detail later in this Chapter) form in the material during fatigue loading.

The cyclic stress strain curves of materials are helpful in dividing fatigue into two categories: high and low strain fatigue. For strain levels on or below the plateau region, fatigue is considered as low strain, high cycle fatigue where fatigue lives are generally in excess of 10^5 cycles to failure, while for strain levels in the Region C, fatigue is considered high strain, low cycle fatigue [28]. Although this division is clear for single crystal materials, it is not so clear for polycrystals since their plateau regions are not always as obvious. For example, in a study involving polycrystalline copper,

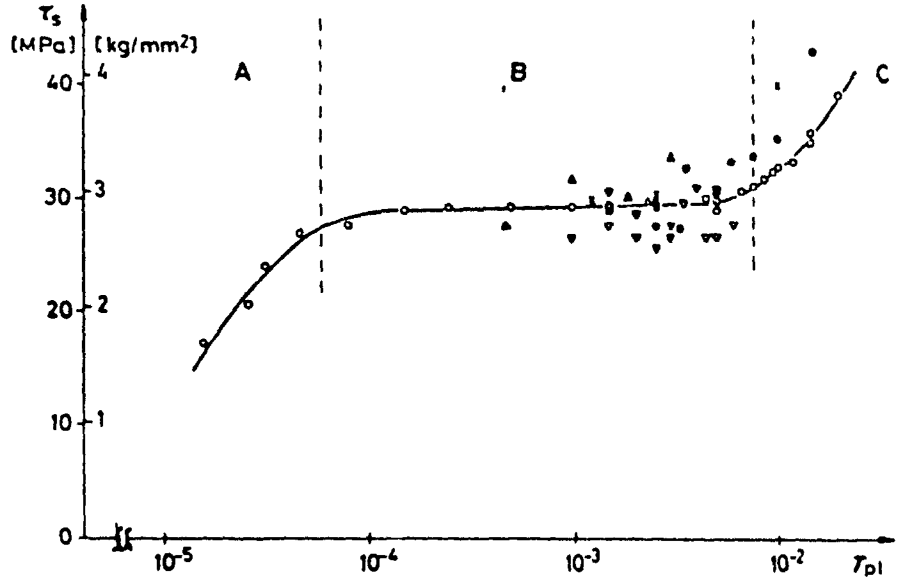

Figure 2.2: Cyclic Stress Strain Curve for Copper Single Crystal: Resolved Shear Stress Versus Plastic Resolved Shear-Stress Amplitude. *ref* 27

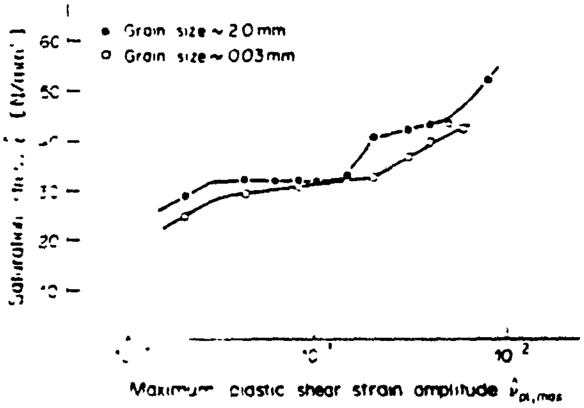

Figure 2.3: Cyclic Stress-Strain Curves of Polycrystalline Copper in Materials with Different Grain Sizes. *ref* 29

[29], it was found that for large grain sizes such as 2 mm, the cyclic stress-strain curve is similar to that of single crystals, in that it indeed showed a distinguishable plateau, while for small grain sizes of about 30 μm, a region with a flatter slope existed in the center of the curve instead of a real plateau, as demonstrated in Figure 2.3. Whether or not the division into of high and low strain fatigue in polycrystals can be determined by the cyclic stress strain curve is still an unsettled question.

The division into high and low cycle fatigue is necessary because the differences in the microstructure of materials formed in low and high strain fatigue cause major differences in the mechanisms of crack initiation and microcrack propagation. In low strain fatigue the microstructure of certain metals is characterized by PSBs with plastic strain highly localized in them (explained later in this Chapter), and fatal crack initiation is transgranular within grains, mainly along PSBs. As the strain amplitude increases, the dislocation pattern of material gradually changes to a cellular structure and the strain within grains becomes homogenized. Grain boundary steps were produced by irreversible slip at "persistent grain boundaries" which later became stress raisers and effective sites for crack initiation [30]-[32].

2.2.2 Persistent Slip Bands in Low Strain Fatigue

The term "persistent slip band" was introduced by Thompson *et al* in 1956 [33]. After various amounts of stress cycling in copper and nickel, a thin layer of the specimen surface was removed. Many of the slip lines on the surface disappeared, but some did not; instead they "persisted" and were given the name "Persistent Slip Bands"(PSBs).

PSBs have been found in most face-centered-cubic (fcc) structured materials, including copper and some of the body-centered-cubic (bcc) structured materials. They occur not only in single crystals but also in polycrystalline materials [34,35]. The structure and functions of PSBs have been widely studied [36]-[39] due to the fact that in low strain fatigue, cracks often initiate on PSBs at locations where the PSBs interact with surface boundaries, such as free surfaces or grain boundaries. Figure 2.4 [23] pictures typical PSB structures. The ladder like structure of PSBs is comprised by high dislocation density walls (black lines as the frame of the ladder) and low dislocation density matrix material (white region in the ladder structure).

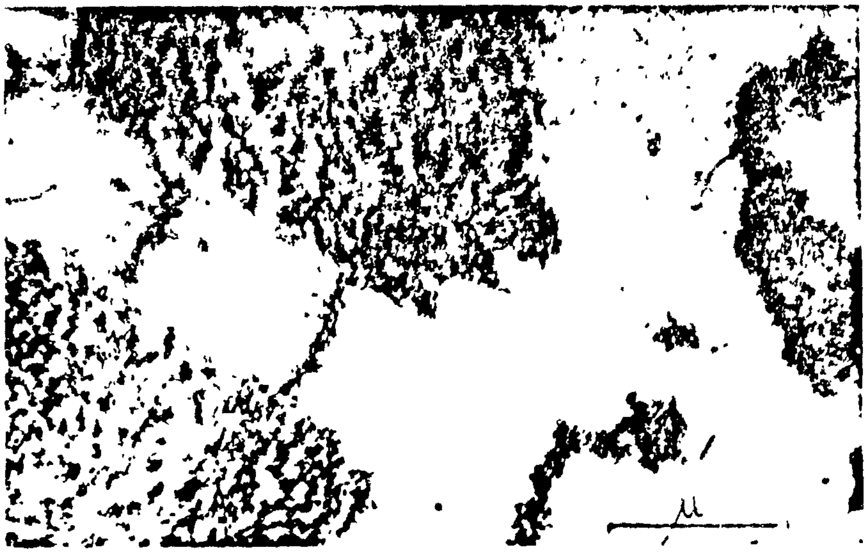

Figure 2.4: Typical Ladderlike Dislocation Structure of a PSB in a Copper Single Crystal. *ref* 23

Figure 2.5 [40] shows the structure of a material with PSBs in the bulk material where the dark parts are the veins with high dislocation density. Inside of PSBs, the screw dislocation density is $\sim 10^{13}m^{-2}$ between the walls and $\sim 10^{15}m^{-2}$ in the walls. Inside of the bulk material, the density is $\sim 10^{12}m^{-2}$ between the veins and $\sim 10^{15}m^{-2}$ in the veins [41,42], which is the same as in the walls of the PSBs. Since the volume fraction of hard walls in PSBs is only 0.1 compared to the 0.5 volume fraction of hard veins in the bulk matrix, the PSBs are much softer than the bulk material and hence the strain is highly localized in the PSBs. This is certainly favourable for crack initiation.

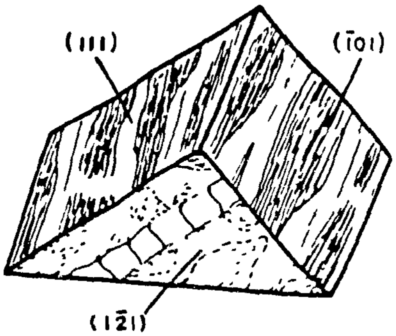

Figure 2.5: Three-Dimensional Configuration of Dislocations in Copper Single Crystals Strain-Cycled to Saturation. *ref* 40

PSB formation theories agree that the PSBs are evolved from the loop patchs or vein structures formed early in the fatigue process in annealed materials. Kuhlmann-Wilsdorf and Laird [39] proposed that early in the cyclic loading process of annealled materials loop patches form to block the dislocations. As the stress slowly increases to a new level, the formed loop patches are destroyed, accompanied by the occurrence of strain bursts [25,43,44]. As the cyclic loading continues, finer and stronger loop patches are established. At a higher stress level the new loop patches will be destroyed again. This build/destroy procedure repeats many times until the strain becomes so high that no loop patches can stop the movement of the dislocations, then the PSBs are formed.

A model for the dislocation motion inside PSBs was proposed by Kuhlmann-Wilsdorf and Laird [39]. Briefly, when a shear stress acts on a plane containing PSBs, the edge dislocations on one side of a PSB wall are "spun out" by many similarly signed screw dislocations to the nearby tilt wall containing edge dislocations of opposite sign, thereby causing the large strains observed in the neighbourhood of PSBs. For a stress reversal, the direction of the "spin" is reversed.

There are some unsettled problems concerning PSBs. One concerns how the PSBs are formed from the loop patchs or vein structure. Kuhlmann-Wilsdorf and Laird [39,44] support Winter's [45] proposal that PSBs are formed from the inside of the veins or loop patches. Mughrabi *et al* [37], on the other side, argue that PSBs are formed from outside of the veins. Another problem is the lower limit of PSB formation. Mughrabi *et al* [37] believe the veins cannot accommodate plastic strain in excess of $\sim 10^{-4}$. Only for plastic strains bigger than this value, will the structure undergo a rearrangement and PSBs form since, as discussed earlier, the PSBs are more capable of carrying large amounts of strain. Contrary to this, Kuhlmann-Wilsdorf and Laird [44] found that for copper single crystals, PSBs begin to form when the applied resolved shear stress reached about 30 MPa on the primary slip system despite the strain amplitude within the PSBs, and this critical stress appears to be triggered at a critical loop density. Only further experimentation can resolve these matters.

2.2.3 Extrusions/Intrusions from Smooth Surfaces

The extrusion and intrusion phenomenon was first reported by Forsyth in 1953 [46]. Typical extrusions and intrusions from an electrolytically polished surface of a copper specimen are shown in Figure 2.6 [47]. According to Forsyth, the ribbon-like extrusions, paired with fine "crevices" (which are now called intrusions) at the root, may occur when the fatigue stress produces local recrystallization in both annealed and cold-worked metals and alloys. Extrusions seem to be particularly associated with age-hardenable materials [48], while intrusions are generally in annealed copper [49].

The extrusion/intrusion of materials from smooth surfaces is fast at the begining of test, it slows down in a later stage of test [49]. It is hard to define the difference between a microcrack and an intrusion because, strictly speaking, an intrusion is a crack. Extrusions/intrusions are essential in the crack initiation process, especially in low strain fatigue. It has been proved that by eliminating extrusions/intrusions by repolishing the surface again and again during tests, the life of a specimen can be considerably extended [33].

All existing extrusion/intrusion models concern the irreversible sliding of material along maximum shear planes. Two representative models will be introduced here. In the first one [39], the extrusions or intrusions are formed by the gliding of the

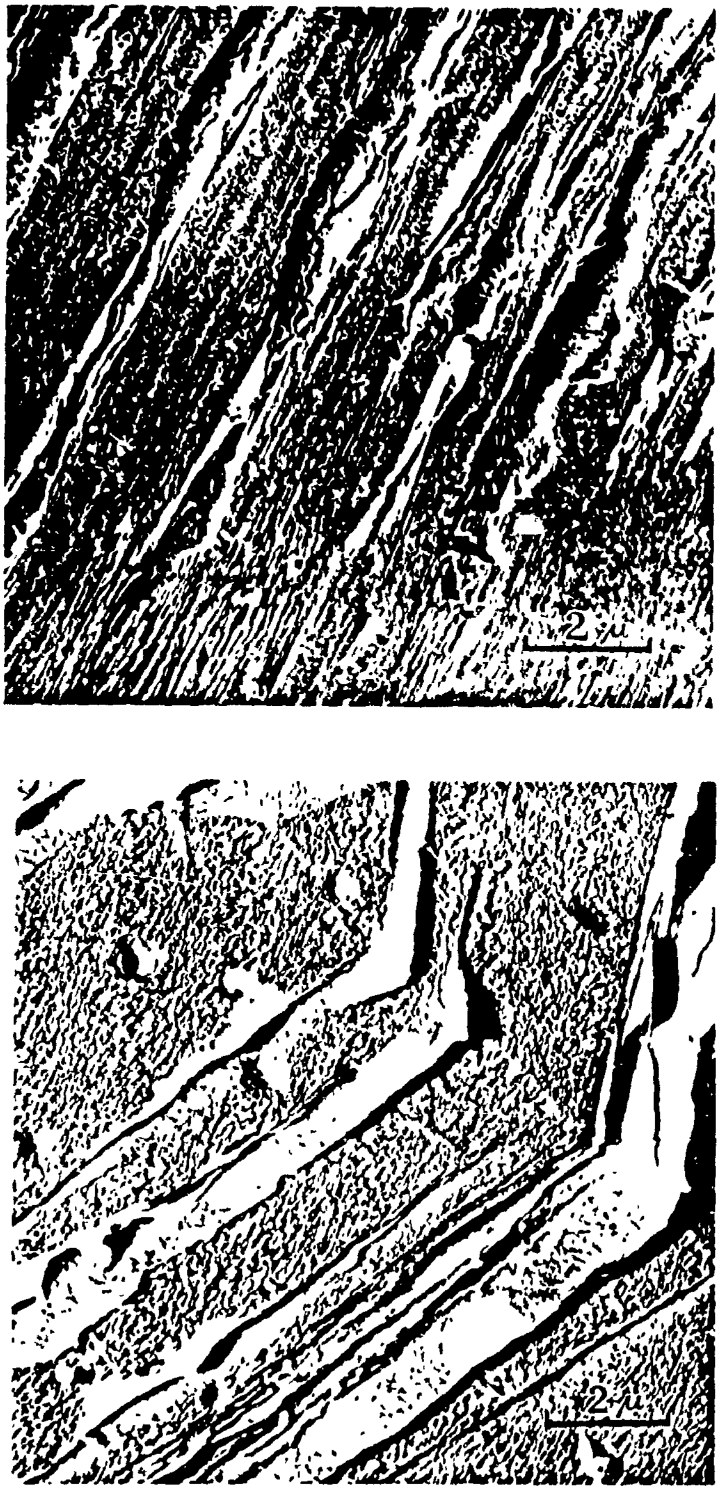

Figure 2.6: Extrusion and Intrusion Along Slip Bands. *ref* 47

edge dislocations, with the help of the motion of screw dislocations, respectively, out of or into the PSB boundaries. In another model [50], the extrusions/intrusions are interpreted as a combination of gliding and annihilation of dislocations with opposite signs wihin the slip bands.

2.2.4 Reversibility and Irreversibility of Cyclic Deformation

Finney and Laird [40] studied the localization of plastic strain in copper single crystals cycled into saturation and found that beyond a certain strain level there was an overall reversibility and some individual slip step irreversibility. What induces this irreversibility is not clear. Margolin *et al* [51] suggested that in the irreversible slip process, cross-slip is a control factor Some other authors [29,38,49] believe the mutual annihilation of unlike dislocations constitutes a major source of cycle irreversibility. This annihilation persists in cyclic saturation since a dynamic balance exists between dislocation multiplication and annihilation in steady-state cyclic saturation.

A parameter, β, associated with the annihilation distance, Burgers vector, the number of dislocations of the same sign and the shear strain amplitude, has been proposed to determine whether the motion of the dislocation is reversible or not [29,49,52] For $\beta < 1$, the dislocations move reversibly whereas for $\beta > 1$, slip becomes irreversible.

Slip irreversibility of material under fatigue loading plays a special role in fatigue failure. PSB formation, extrusion/intrusion, grain boundary opening, surface roughening, crack initiation and propagation are all based on the localized irreversible dislocation movements. For specimens under the fatigue limit stress, although some slip lines may still form on the surface [53,54], they are not Persistent Slip Bands and do not penetrate into the bulk material, thereby ensuring the specimen an indefinite life in fatigue tests.

2.2.5 The Microcrack Nucleation Process

The mechanism of microcrack propagation is the same as and a continuation of the surface extrusion/intrusion in low strain fatigue as discussed earlier, plus the coalescence of microcrack. The driving force of this early propagation is the highly localized shear strain on the maximum shear deformation plane (containing PSBs for surface grains).

Although it has been discussed by Provan [18] and Provan and Zhai [16,17] that the Stage I crack propagation, first introduced by Forsyth [55], is related to crack initiation, data on crack growth in this stage are scarce, and micro-mechanisms for crack growth have not been well elucidated. The definition of Stage I and Stage II crack propagation proposed by Forsyth is shown in Figure 2.7 where the direction of Stage I propagation is at a 45° angle to the applied load. As defined in the Metal Handbook [56], "Stage I is the initiation of cracks and their propagation by slip-plane fracture, extending inward from the surface at approximately 45° to the stress axis. A Stage I fracture never extends over more then about two to five grains around the origin. In each grain, the fracture surface is along a well-defined crystallographic plane". It is believed that the Stage I propagation part on the fracture surface is featureless.

The crack tip sliding displacement (CTSD) as a driving force in Stage I microcrack propagation has been discussed by Li [57]. However, discussions of the kinetics of Stage I propagation are scarce in the literature, and discussions of Stage I propagation in high strain fatigue in which cracks initiate at grain boundaries are nonexistant.

Stage II propagation is on the plane perpendicular to the applied load. The crack propagation changes directions only after it passes a critical length. In a study of copper single crystals fatigued at constant strain amplitudes [58], it had been found that this critical length depends on the Schmid factors of the specimen. The crack length at the transition from Stage I to Stage II ranged from $0.6mm$ to $3.11mm$ as the ratio of the second highest Schmid factor to the Schmid factor of the primary slip system changes from 97° to 78°. Small crack studies in some polycrystals of the transition from Stage I to Stage II propagation indicated that it takes place before the crack crosses boundaries in large grained materials (from 50 μm to 100 μm) and at grain boundaries in small grained materials [59,60].

2.3 Mechanical Engineering Studies of Crack Initiation

2.3.1 Quantitative Analyses of Crack Initiation

If the above review of the mechanism of crack initiation seems to have been systematic, the study from the engineering point of view of crack initiation is still at a preliminary stage. Although crack initiation has been studied widely and mentioned in countless papers, references [61] -[70] are but a few, mathematical models giving

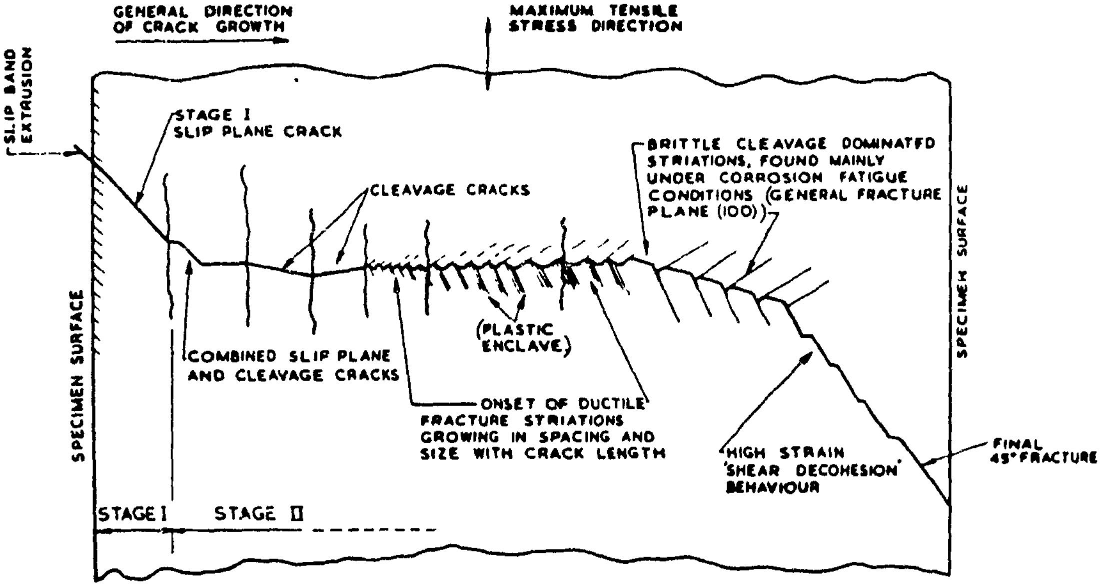

Figure 2.7: Stage I and Stage II Propagation Proposed by Forsyth. *ref* 55

quantitative estimation of the cycles to a certain crack length within the initiation and early Stage I growth region are lacking. Most of the published results are limited to qualitative observations of the crack initiation and microcrack nucleation process, such as the crack initiation sites (either on grain boundaries or inside the grain), the orientation and the density of the crack, or the stress strain cycle of producing a crack to an assumed initiation length a_0, etc.

The only quantitative analyses in crack initiation derived formulas relating the total crack initiation life N_i to the applied strain level, and produced the $S - N_i$ (stress or strain versus crack initiation life) curves. Both are based on an assumed crack initiation length a_0 [65]-[67]. For example, it was demonstrated [65,66] that the number of crack initiation cycles, measured using smooth hourglass-shape specimens of Type 304 stainless steel at 593° C, satisfied the following empirical formula:

$$N_o(S) = 0.0122\,(\Delta\varepsilon_p)^{-2.474}, \tag{2.1}$$

where $N_o(S)$ is the number of cycles to initiate a crack of length $0.1mm$ and $\Delta\varepsilon_p$ is the plastic strain range. This is not a bad idea for practical engineering applications, except that the initial crack length remains a problem. A change in the length may cause a big difference in the $S - N_i$ curve.

The definition of the initiated crack length a_0 is the subject of intensive study at the present time. From the perspective of fatigue design or lifetime prediction, the definition of an engineering-size crack is critical. Although it has been realized that this crack length should be a function of material, stress level, and notch geometry

[61], in the literature it has been taken to be a constant or a certain range such as:

1. any length detectable during tests (which can be very different, depending on test facilities and experimental technique),
2. a length from 0.1 mm (which is most common) to $1mm$,
3. the average grain diameter,
4. a constant length of the crack propagation threshold in LEFM studies divided by the fatigue limit: $a_0 = \Delta K_{th}/\Delta\sigma_f$.

Without a clear definition of the initial crack length, the correct $S - N_i$ cannot be derived; nor is it impossible to compare the crack initiation life N_i in extensive reports and draw correct conclusions of crack initiation and propagation. This is why proposing a new definition of crack initiation is listed as one of the objectives.

2.3.2 Crack Profile Changes in the Initiation Region

Changes in crack profiles in the initiation region are not really available in the present literature. So far, crack shape changes were mainly carried on for crack sizes larger than 1 mm. For example, semi-elliptical surface cracks in finite plates had been calculated in [71,72] and compared with experimental results in the literature, where the shortest crack length was 1.3 mm. The development of crack depth, c, to half of surface crack length, a, ratio, $\lambda = c/a$, was shown to be dependent on the initial ratio, λ_o. When λ_o started above 1, λ decreased as the crack length increased; when λ_o started below 1, λ increased. For many materials, λ converges close to unity.

The smallest crack involved in crack profile studies is a surface crack length of 60 μm in the report of Hoshide *et al* [73]. They studied the shape change for cracks initiated on smooth cylindrical specimens for several materials including a 99.99% pure copper containing 3 ppm oxygen annealed to a grain size of 97 μm. The technique that was employed to obtain the crack depth was to electropolish the specimens with several cracks on the surface repeatedly, until the crack disappeared. The variations in length were recorded by means of replicas while the depth c of a crack was calculated as half of the reduction in diameter due to electropolishing. This way they monitored the change of λ, starting from a surface crack length $2a$ of 60 μm. λ decreased from 1.2 to 0.8 when $2a$ increased from 60 μm to about 1 mm (the specimen diameter is 6 mm) before microcrack coalescence took place, while λ decreased from 0.6 to 0.4 when $2a$ increased from about 200 μm to 3 mm after crack coalescence.

2.4 Developments in Short Crack Propagation

2.4.1 Introduction

New developments in experimental techniques allow smaller and smaller crack lengths to be monitored and provide conditions for the new rapid developments in the study of short cracks. Today, the research of fatigue fracture has tended to shift from conventional, through thickness, long cracks to small cracks. Although the subject is relatively new, the literature is extensive. Some typical short crack propagation curves from references [15], [74]-[76] are selected and shown in Figure 2.8, where the abscissas represent the stress intensity factor and the ordinates are the crack propagation rates.

Some of the short crack curves merge, become part of long crack curves, and follow the long crack growth pattern, as is seen in (a) and (b) of Figure 2.8; but some of them don't, as shown in (c). It appears that the curve of short cracks starting at the tip of the relatively large notch has a tendency to merge with the curves for long cracks, and this transition depends on the plastic zone size at the notch root of the long cracks [77]. The bigger the plastic zone, the larger the length of the short crack at which the transition to the long crack curve occurs. On the other side, the curve for short cracks initiating from smooth surfaces does not always merge with long crack curves, although the transition from the short crack behaviour to a growth pattern similar to that of long cracks has been observed. It has been suggested that this transition takes place at a crack depth of 5-10 times the average grain size [12].

The most striking characteristics of the short crack propagation curves are:

1. crack propagation at stress intensity levels lower than the propagation threshold determined by LEFM methods,

2. fast propagation at the beginning of tests and a subsequent retardation of growth reflected as the valley in the curves, and

3. faster growth rate than the long cracks at the same stress intensity factor in a majority of short crack cases, as indicated by (a) to (c), where all the short crack curves are situated above the long crack curves. However, slower crack growth due to the deceleration of cracks at grain boundaries were also reported [74,78] and reviewed [79].

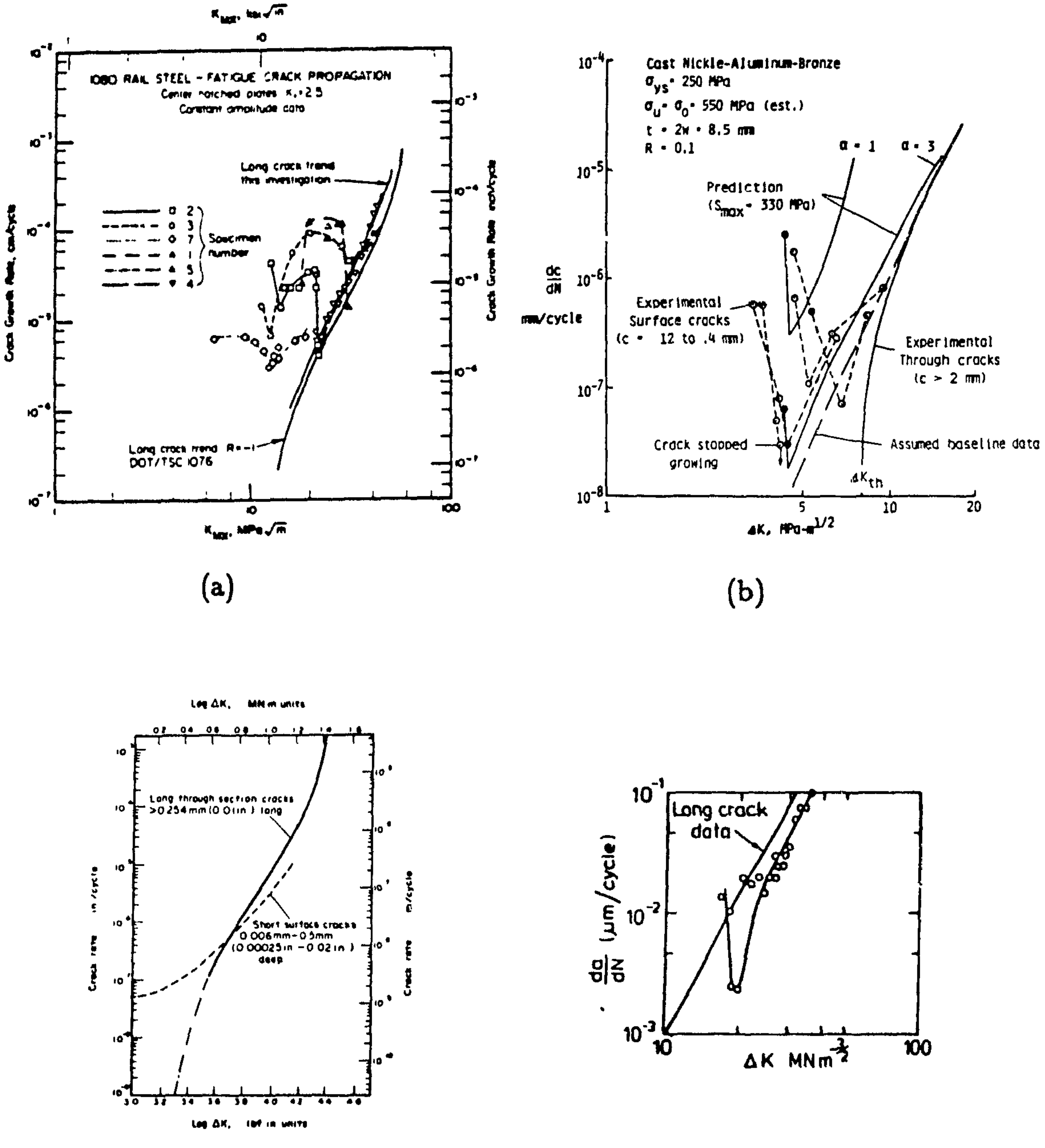

(a)

(b)

(c)

(d)

Figure 2.8: Different Short Crack Behaviours Reported in the Literature. (a) *ref* 76 (b) *ref* 75 (c) *ref* 15 (d) *ref* 74

The above-mentioned anomalous behavior of short cracks is termed the "short crack effect" and has been well reviewed by Leis *et al* [12] and Suresh and Ritchie [80,81].

2.4.2 Causes of the Short Crack Effect

Whether a crack will propagate at the same rate as another crack and in the same pattern depends on whether it satisfies all the similitude conditions. Failure to satisfy similitude conditions is essential to the apparent short crack effect. In summary, short cracks violate similitude conditions in the following ways:

1. Small plastic zone surrounding crack tip. In LEFM analysis, the surrounding stress field of a crack is adequately described by the stress intensity factor K, provided the size of the plastic zone is small compared to all length dimensions such as thickness, remaining ligament size of the specimen and the crack length, and is also small with respect to the distance over which the first term of the elastic stress field solution is dominant. For a crack of a size smaller than the grain size but with the same stress intensity K as that of a long crack, the plastic zone of the small crack should be the same as the long one, according to similitude condition. However, if the plastic zone of each is the same, the ratio of the plastic zone diameter to the short crack length is much larger than its comparable ratio. If the plastic zones are not the same, the similitude condition is also violated.

2. Metallurgical features surrounding crack tips. The front of long cracks (even for multiphase materials with high crystallographic anisotropy) is large enough to average out the differences of phase, grain orientation, dislocation density,

etc., to make the material metallurgically isotropic; while the front of short cracks with lengths of less than several grain sizes is strongly influenced by all these factors to make the material surrounding crack tip anisotropic.

3. Closure effect. The interference and physical contact between mating fracture surfaces in the wake of the crack tip lead to an effective closure of cracks. Plasticity induced closure [82] (the constraint of surrounding elastic material on the residual stretch in material previously plastically strained at the tip) and roughness induced closure [83]-[85] (some discrete points contact due to significant inelastic mode II crack tip displacements) are the two main forms of crack closure. Under the influence of the closure effect, the crack does not open until the applied load reaches a certain value, which is called, the crack opening load.

   It has been experimentally shown [85]-[87] that the stress intensity factor threshold in a long crack propagation curve can be explained by crack closure behavior. Minakawa and McEvily [88] conducted a threshold test on a compact specimen, measured the crack opening loads as the ΔK level approached ΔK_{th} and found that the ratio of the crack opening load and the maximum applied load P_o/P_{max} was around $0.15 \sim 0.35$ at high ΔK values and rose rapidly towards unity at the threshold as depicted in Figure 2.9. The same trend had been reported by Ohta *et al* as well [89]. The overload used in the load reduction scheme to arrive at the stress intensity threshold may well cause this abnormal behaviour by introducing excessive plastic deformation along the crack trail.

   On the other hand, in a study of small cracks about $10\mu m$ long by Newman [90], shown in Figure 2.10, the short cracks remained open even at the minimum applied compressive load. This phenomenon is termed as the "free surface effect", which is attributed to the absence of crack closure. It is seen from Figure 2.10 that the ratio P_o/P_{max} of the short cracks started from -1, increased rapidly to reach a turning point, and thereafter remains constant, about $0.3 \sim 0.4$. The violation in closure effect similitude is caused mainly by the incorrect or incomplete implementation of LEFM in the experimental method and the different natures of long and short cracks, where the former is precracked to a length beyond the scope of "free surface effect", while the latter either starts from a free surface or a small crack depth where it is still influenced by "free surface effect".

4. Crack propagation mechanisms. The stage II propagation (the growth on a plane normal to the applied load) is the only style applicable to long cracks, while short cracks may experience a transition from stage I (growth on a plane at 45° to applied load) to stage II, especially in the case of cracks initiating from a smooth surface.

5. All similitude conditions are violated in the absence of a dominant crack. For a short crack initiated from a smooth surface, where $a = 0$, not only the above-mentioned but also other similitude conditions are violated. In this case, the stress field surrounding crack tip in LEFM analysis cannot be defined for the zero crack length.

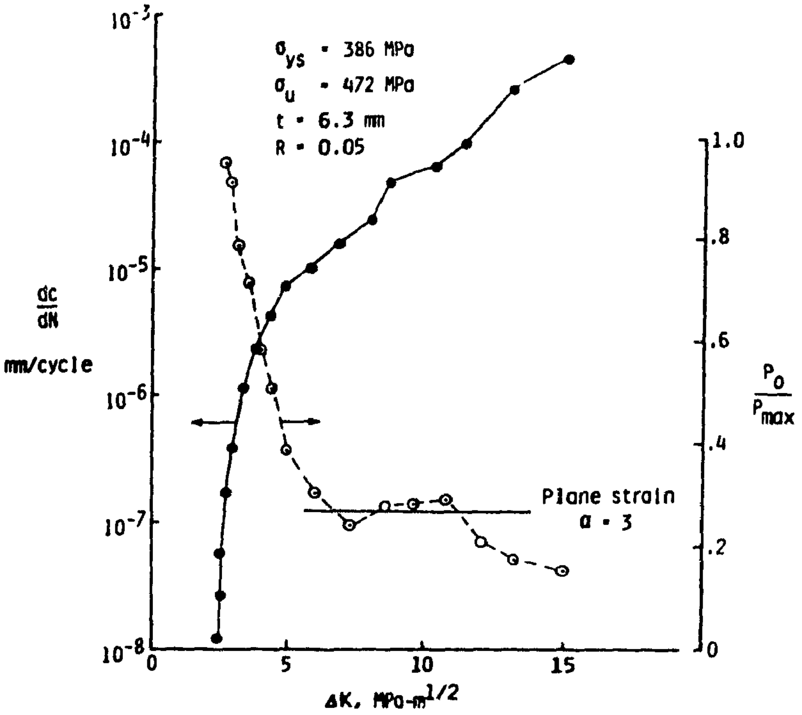

Figure 2.9: Comparison of Experimental Growth Rates and Crack Opening Stresses on a 2219-T87 Aluminum Alloy Compact Specimen. *ref* 88

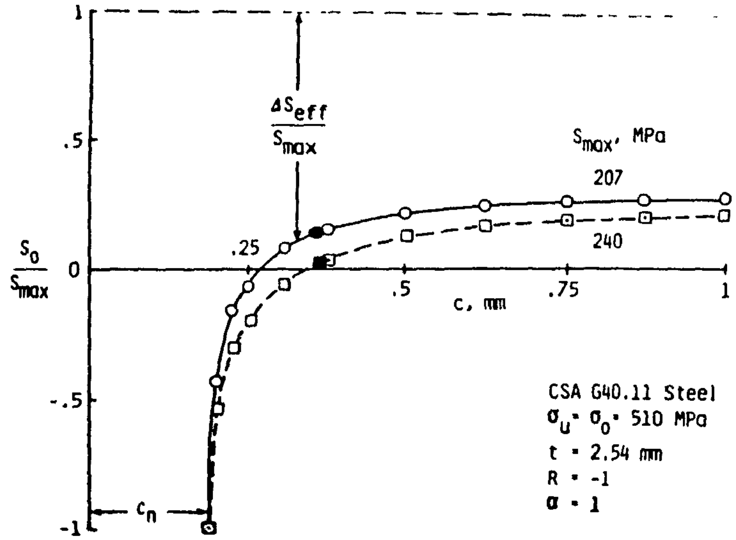

Figure 2.10: Calculated Crack Opening Stresses as a Function of Crack Length under Constant Amplitude Loading. *ref* 90

2.4.3 Different Models in the Analysis of Short Crack Propagation

Considering the almost complete breakdown of similitude conditions, the conventional stress intensity factor ΔK seems not to be a proper controlling parameter in short crack analysis. There have been attempts to remedy the inconsistency in short and long crack propagation by finding other driving forces.

The large plastic zone size compared to the crack length of short cracks has led to the adoption of an elastic-plastic fracture mechanics (EPFM) J-integral formulation. This path-independent line integral was originated by Rice [91] as a two-dimensional line integral for nonlinear elastic materials in fracture mechanics. In the special case of linear elastic materials, J-integral reduces to the strain energy release rate G which may be expressed as:

$$G = \frac{K^2}{E} = J_{elastic}, \tag{2.2}$$

where K is the stress intensity factor and E is Young's modulus. For elastic-plastic materials, J-integral loses its interpretation in terms of the potential energy available for crack extension, but retains physical significance as a measure of the characteristic crack-tip strain field and has been widely applied in elastic-plastic fracture mechanics.

In the field of short cracks, Dowling derived an expression of ΔJ for small semicircular surface crack and claimed to have brought the short crack data closer to those of the long crack [92]. The major improvement that the ΔJ approach brought to short crack analysis is that of cutting down violations of the plastic zone size requirement. However, the violations of other similitude conditions still remain, and thus ΔJ is unlikely to be the most suitable driving force for short crack propagation.

Another approach by El Haddad *et al* [93,94] was to assume that a "fictitious" crack length ℓ_o existed at the beginning of the test, with an expression of:

$$\ell_o = \frac{1}{\pi} \left(\Delta K_{th} / \Delta \sigma_e \right)^2, \tag{2.3}$$

where ΔK_{th} is the stress intensity threshold and $\Delta \sigma_e$ is the fatigue limit stress of the material. By adding this initial crack length ℓ_o to the actual crack length in the expression of ΔK, a modified effective ΔK is obtained:

$$\Delta K_{eff} = Q \, \Delta \sigma \sqrt{(a + \ell_o)}, \tag{2.4}$$

where Q is the usual geometric factor and ℓ_o is given in Eqn (2.3). In some cases, this effective stress intensity factor or effective ΔJ-integral was claimed to be successful. However, Lankford and coauthors [95] conducted experiments of both short and long cracks in a high strength precipitation-hardened aluminum alloy, $Al7075 - T651$, and found that although this ΔK_{eff} formulation brought the short crack propagation results closer to the long cracks in air environments, it did not improve the description of experiments involving inert environments.

The physical significance of ℓ_o in Eqn (2.4) was not elucidated; neither is there any convincing correlation between ℓ_o and any characteristic microstructural dimension. Even if it did bring short and long cracks together (which still needs a lot more experimental proof), how can one explain that a crack with such a fictitious length exists at the beginning of tests? How can it be put to serious engineering application when it is not established on a solid physical basis? Furthermore, if ℓ_o is entirely dependent on the threshold, when the determination of the crack propagation threshold by LEFM is obtained through improper means, how can this parameter be reliable?

Since the closure effect is one of the major factors in causing differences between the growth of small and large cracks, an effective stress intensity factor including the closure effect has been introduced. While the crack cannot propagate when it remains closed, the net effect of closure is to reduce the nominal stress intensity range ΔK. By deducting that part of the ΔK from the full value, a corrected form of the stress intensity factor becomes [96]:

$$\Delta K_{eff,cl} = \left[\frac{1 - P_o/P_{max}}{1 - R}\right] \Delta K, \tag{2.5}$$

where R is the stress ratio, P_o the crack opening load, and P_{max} the maximum applied load.

In the application of Eqn 2.5, the key is to find the right crack opening force. Analyses of the closure effect for small cracks are not often seen in the literature. Newman's closure analysis [90] had only been developed for through thickness crack (CCT) configurations. Besides the results of the "free surface effect" decaying process shown in Figure 2.10, where P_o/P_{max} changed from -1 to $0.3 \sim 0.4$, his analysis was also modified to suit small surface crack growth under bending situations. He suggested that the stress intensity factor ΔK for small surface cracks (not specifying how small they were) under bending may be obtained by multiplying the stress intensity factor for CCT specimen by a factor of 0.7, which implies that the ratio P_o/P_{max} is around 0.3. On the other hand, in the work of Lankford *et al* [95] who investigated short surface cracks initiated from smooth surfaces, the ratio P_o/P_{max} for short cracks with lengths from 40 to 100 μm fluctuated at $\sim$ 0.6 for the stress intensity range investigated. No conclusions can be drawn from present literature about the region where the ratio P_o/P_{max} starts from -1 and transfers to a constant value as shown in Figure 2.10, even though this transition may be essential in short crack analyses.

The ratio of crack opening load to maximum cyclic load versus the stress intensity factor for long cracks in Lankford and coauthor's work [95] could have been simplified as a linear function of the crack length. The ratio increased continuously as the stress intensity decreased and was nearly unity at the threshold, which is in agreement with other works concerning the closure analysis of long cracks. By applying the effective stress intensity factor in Eqn (2.4), however, the analyses of the short and long crack experimental data were not really improved [95].

An effective and necessary way to minimize violations of the similitude conditions between short and long cracks caused by closure effects is to modify the testing procedures in obtaining the LEFM crack growth rate data at low stress intensity levels. Either the load reduction scheme technique in threshold testing must be changed, or the residual deformations on the crack wake by overloading must be eliminated through proper means such as annealing before threshold testing, or machining away the plasticly deformed parts.

The last possible driving force to be discussed is the Crack Tip Opening Displacement, CTOD, which seems to be the most promising parameter since it has the advantage of being able to account for both the large local plastic deformation around the short crack front and the closure effect as well. Also, to the extent that crack growth is a geometrical consequence of slip, CTOD is certainly a measurement of crack extension.

However, a direct measurement of CTOD is difficult and virtually impossible in a routine test, not to mention its measurement from a smooth surface for the study of crack initiation, when one does not even know where cracks are going to start. It is usually obtained indirectly through a theoretical model involving ΔK, which is, unfortunately, still limited to a collinear representation of the plastic zone. But short cracks do not follow this representation. For example, it has been found that the measured CTOD values are much higher than those theoretically obtained for short cracks [95]. The discrepancy lies in the theoretical expression itself, insofar as it is based on ΔK. Even if a better expression of CTOD can be found, it is doubtful whether da/dN for small cracks with short fronts can be uniquely related to CTOD due to interference of the microstructural crystallographic orientation, phase, etc.

In summary, none of the existing models describing short crack propagation are considered as being entirely satisfactory. They either account for only one or two of the factors, in violation of the similitude condition, or have no solid physical basis.

Chapter 3

MODELLING OF FATIGUE CRACK INITIATION AND EARLY PROPAGATION

3.1 Introduction

The future of crack initiation and short crack studies seems dubious after the previous review. While continuous testing of the proposed parameters carries on and other driving forces are being sought, the study of crack initiation and short crack problems may benefit from a fresh look from alternative points of view. For example, why should a macroscopic parameter be expected to describe in every detail material behaviour in the microscopic region? What if an average can be found that faithfully describes the crack initiation and propagation features in the microscopic range and can be implemented in engineering analyses? Suppose that the crystal orientation of the grains containing the short crack and the directions of the surrounding grains are known and the plastic zone size around the crack tip can be measured, so that the exact local stress strain distribution can be evaluated. Suppose the closure effect and Stage I to Stage II propagation transition are known. Suppose further that the crack initiation and early propagation can be expressed by a driving force which includes all these factors. The formula describing crack initiation and propagation must be very complicated. After all, the results of research are meant to be applicable in engineering practice, and a simple and relatively reliable method would be most welcome.

On the other hand, it is also true that a short crack will transit to normal long crack behaviour although the transition point has yet to be found. As complicated as it promises to be, there must be rules controlling crack initiation and short crack propagation processes from the macroscopic point of view. As long as a model is proposed from a proper understanding of fatigue crack mechanisms and is proved by experimental results, it will be accepted by the engineering profession.

In this Chapter, a series of models of crack initiation and early propagation are proposed and discussed. These models apply only to fatal cracks, since main cracks and non-propagating cracks have different behaviour and propagation mechanisms.

3.2 The Engineering Model

3.2.1 Plastic Strain Intensity Factor ΔK_p

As mentioned in the review, irreversible plastic deformation plays a special role in fatigue crack initiation and early propagation. In light of this, a new driving force, the *plastic strain intensity factor*, ΔK_p, is proposed for fatigue crack initiation and early propagation analysis. Its general form is given by:

$$\Delta K_p = \mathcal{F}(y,t,r,e,c)\, Q\, (2\,\Delta\varepsilon_p\, E)\,\sqrt{a}; \quad (FL^{-3/2}) \tag{3.1}$$

where $\Delta\varepsilon_p$ — half of the plastic strain amplitude,

Q — the conventional geometry factor that depends on a,

a — half of the surface crack length,

E — the Young's modulus,

and $\mathcal{F}(y,t,r,e,c)$ is a function of the strength and microstructure of the material y, the temperature t, the stress ratio r, the environment of the tests e, and a measure of the closure effect c.

The function $\mathcal{F}(y,t,r,e,c)$ is included in the formula because the plastic strain intensity factor is meant to be a general driving force in fatigue analysis under any condition. These factors should also largely affect the crack initiation behaviour for, as mentioned in the Introduction, they affect the crack propagation and short crack propagation properties. Whenever possible, the influence of these factors should be determined for each material.

3.2.2 The Engineering Model of Fatigue Crack Initiation and Propagation

Based on this driving force, the model further proposes that the growth rate of a fatal crack, da/dN, be a function of the plastic strain intensity factor as schematically shown in Figure 3.1 where the abscissa is the new driving force ΔK_p and the ordinate is the crack growth rate da/dN.

In Figure 3.1 the curve also has three distinct regions. The crack propagation region, Region II, and the fast propagation region, Region III, are the same as in LEFM analysis, while Region I_p is quite different. In LEFM analyses, Region I is virtually a single value of the crack propagation threshold; the whole crack initiation region is compressed into a single vertical line at the so-called ΔK_{th}. In contrast, Region I_p, in the present model, spreads to another straight line with a slope flatter than that for Region II. This more accurately reflects the true nature of crack initiation.

As mentioned earlier, microcrack propagation in Region I_p is strongly affected by the microstructure and violates many similitude conditions; as a consequence the crack growth pattern during this period is rather complicated under any description of a macroscopic driving force. However, the abnormal behaviour of the crack especially at the very beginning (fast growth at the beginning and a subsequent valley) is covered by the present model since:

1. a crack within this region is small. In most engineering cases, whether a machine part or component should be removed from service is a question that arises only when the crack has advanced through a certain propagation thresh-

old;

2. the whole crack initiation and microcrack propagation process, even after the early abnormal stage, is an average of separate sub-microcrack or microcrack initiation and nucleation processes. The microcrack grows, stops, grows and stops again, prior to passing the crack propagation threshold. As long as the average is reasonable and an overall rule is generally true, it can be accepted as reflecting the essence of the phenomenon.

Therefore, the straight line simplification for Region I_p proposed in this model is reasonable. Further investigation of this straight line will be carried out in Chapter 5.

The turning point where the crack propagation transition from Region I_p to Region II takes place is defined as ΔK_{pth}, the *plastic crack propagation threshold.* Below this threshold the crack is in the microcrack initiation and nucleation region and the increase of the crack growth rate as a function of the plastic strain intensity factor ΔK_p is very slow. Above this threshold the increase of the growth rate of a fatal crack is fast and becomes compatible with the LEFM analysis.

Similar turning points exist for curves of fatigue crack growth rates versus some other macroscopic driving forces such as the conventional stress intensity factor, ΔK, and the driving force in EPFM analysis, ΔJ-integral, whose comparative form with ΔK_p is $\sqrt{\Delta J \cdot E}$. All these turning points are defined as different forms of the plastic crack propagation threshold. To distinguish the plastic propagation threshold from other existing propagation thresholds, the turning point in the crack growth rate versus the conventional stress intensity factor ΔK curves is defined as the *LEFM*

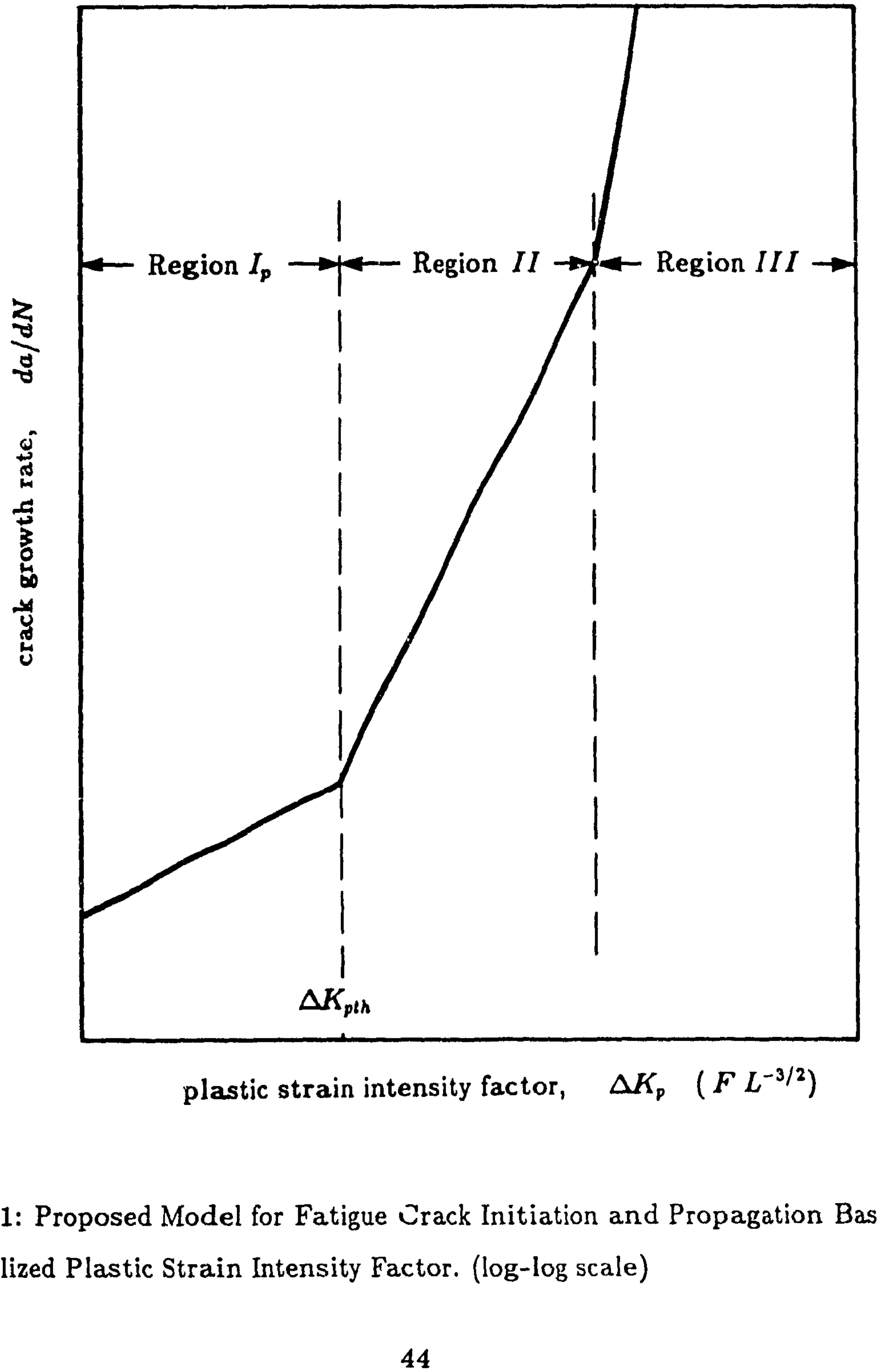

Figure 3.1: Proposed Model for Fatigue Crack Initiation and Propagation Based on a Generalized Plastic Strain Intensity Factor. (log-log scale)

crack propagation threshold, ΔK_{zth}; and the turning point in crack growth rate versus $\sqrt{\Delta J \cdot E}$ is defined as the *energy crack propagation threshold,* $\sqrt{\Delta J \cdot E}_{pth}$.

The plastic crack propagation threshold, ΔK_{pth} is in one way similar to the conventional ΔK_{th}, that is, they are both influenced by material properties, grain sizes, stress ratio R, etc. However, ΔK_{pth} is different from ΔK_{th} since it is also influenced by the applied stress/strain level. Among the three crack propagation thresholds, ΔK_{pth}, ΔK_{zth}, and $\sqrt{\Delta J \cdot E}_{pth}$, the $\sqrt{\Delta J \cdot E}_{pth}$ is a constant for a material with fixed function $\mathcal{F}$, and can be considered as a material property. Therefore, although ΔK_p monitors the crack initiation behaviour, ΔK_{pth} is determined by both elastic and plastic strains and is controlled by the energy crack propagation threshold, $\sqrt{\Delta J \cdot E}_{pth}$.

The crack length obtained at $\sqrt{\Delta J \cdot E}_{pth}$ is defined as a_0, the *initial engineering crack size,* whose value is the same at all the newly proposed crack propagation thresholds with different forms. Under this definition, as the applied stress-strain becomes lower, the initial engineering crack size becomes larger prior to the occurrence of crack propagation. This is compatible with the definition of the initial crack length in LEFM analysis which is not a constant either, but a function of stress level determined at ΔK_{th}, although the method proposed here is different from the LEFM analysis.

3.2.3 Calculation of Crack Initiation and Propagation Lives

Since, in this model, the crack growth rate in the initiation region at all strain levels falls into the same line under plastic strain intensity factor ΔK_p control, a quantitative prediction of fatigue crack initiation life is now possible.

Noticing the logarithmic scale, the expression of the straight line in Region I_p (the crack growth rate) in the initiation region has the form:

$$\frac{da}{dN} = A\,(\,\Delta K_p\,)^{\alpha}, \tag{3.2}$$

where A, α are constants to be determined from experiments; and the Region II Paris-Erdogan Law, Eqn (1.1), is replaced by:

$$\frac{da}{dN} = B\,(\,\Delta K_p\,)^{\gamma}, \tag{3.3}$$

where B and γ are other material constants.

Following Eqn (3.2), the life the specimen spends to initiate a crack with the initial engineering crack size a_0 can be predicted by integrating the crack propagation rate,

$$\begin{aligned} N_i &= \sum_{i=2}^{n} \int_{a_i}^{a_i+1} dN/da\; da \qquad (3.4) \\ &= \sum_{i=2}^{n} \int_{a_i}^{a_i+1} A^{-1} \Delta K_p^{-\alpha} da \\ &= \sum_{i=2}^{n} \int_{a_i}^{a_i+1} A^{-1}\,(\,\mathcal{F}\;Q_i\,(\,2\,\Delta\varepsilon_p\;E\,)\;\sqrt{a}\,)^{-\alpha} da \\ &= A^{-1}\,(\,\mathcal{F}\;(\,2\,\Delta\varepsilon_p\;E\,))^{-\alpha}\;\sum_{i=2}^{n} \int_{a_i}^{a_i+1} (Q_i\;\sqrt{a}\,)^{-\alpha} da. \\ &= C\sum_{i=2}^{n} \int_{a_i}^{a_i+1} (Q_i\;\sqrt{a}\,)^{-\alpha} da. \end{aligned}$$

In the derivation of Eqn (3.4), a_2 is equal to a zero crack length and a_n is equal to the initial engineering crack size, a_0, $\Delta\varepsilon_p$ is taken as the cyclic half plastic strain amplitude in the saturation region and $\mathcal{F}$ has been simplified as being independent of the crack length a.

Similarly, the crack propagation life in Region *II* is derived as

$$\begin{aligned} N_p &= \sum_{j=0}^{N} \int_{a_j}^{a_{j+1}} dN/da \, da \qquad (3.5) \\ &= B^{-1} \left(\mathcal{F} \left(2 \, \Delta\varepsilon_p \, E \right) \right)^{-\gamma} \sum_{j=0}^{N} \int_{a_j}^{a_{j+1}} (Q_j \sqrt{a})^{-\gamma} da \\ &= D \sum_{j=0}^{N} \int_{a_j}^{a_{j+1}} (Q_j \sqrt{a})^{-\gamma} da \end{aligned}$$

where a_N is the critical crack size at the transition from Region *II* to Region *III* in Figure 3.1.

Since the crack propagation rate in Region *III* is very fast (how fast depends on the loading condition and other factors such as the material properties), the corresponding number of cycles the specimen spends in Region *III* is relatively insignificant. Therefore, it is neglected in the present total life calculation. The total fatigue life can now be predicted as the sum of crack initiation life N_i and propagation life N_p, as:

$$\begin{aligned} N &= N_i + N_p \qquad (3.6) \\ &= C \sum_{i=2}^{n} \int_{a_i}^{a_{i+1}} (Q_i \sqrt{a})^{-\alpha} da + D \sum_{j=0}^{N} \int_{a_j}^{a_{j+1}} (Q_j \sqrt{a}) \, da. \end{aligned}$$

3.3 Modelling of Stage I Crack Propagation in the Initiation Region

3.3.1 Definitions

Under the new definitions of the crack initiation region and the plastic crack propagation threshold, it is proposed that *Stage I crack propagation governs the crack propagation and nucleation in the initiation region up to the plastic crack propagation threshold.* Stage I crack propagation is of necessity part of the evolution of a crack. Due to different Stage I propagation mechanisms, it is necessary to divide the crack initiation region further into two sub-regions, as shown in Figure 3.2. In the Figure, the abscissa is again the new driving force, ΔK_p, and the ordinate is the crack growth rate.

The abnormal region with hill and valley at the beginning of the curve is defined as the sub-microcrack initiation and nucleation region, marked as Region I_i in the Figure. The valley in the curve is defined as the *sub-threshold*, marked as ΔK_{sth}. Similar to the plastic crack propagation threshold having different forms under different driving forces, ΔK_{sth} also has different forms under other driving forces and is controlled by the *energy sub-threshold*, $\sqrt{\Delta J \cdot E}_{sth}$. However, since the name "sub-threshold" is introduced here for the first time in fatigue analysis, its use should not cause any confusion. The region between ΔK_{sth} and ΔK_{pth} is defined as the microcrack propagation region, marked as Region I_{ii}. The Stage I crack initiation and propagation mechanisms in these two sub-regions are proposed separately in the following Sections.

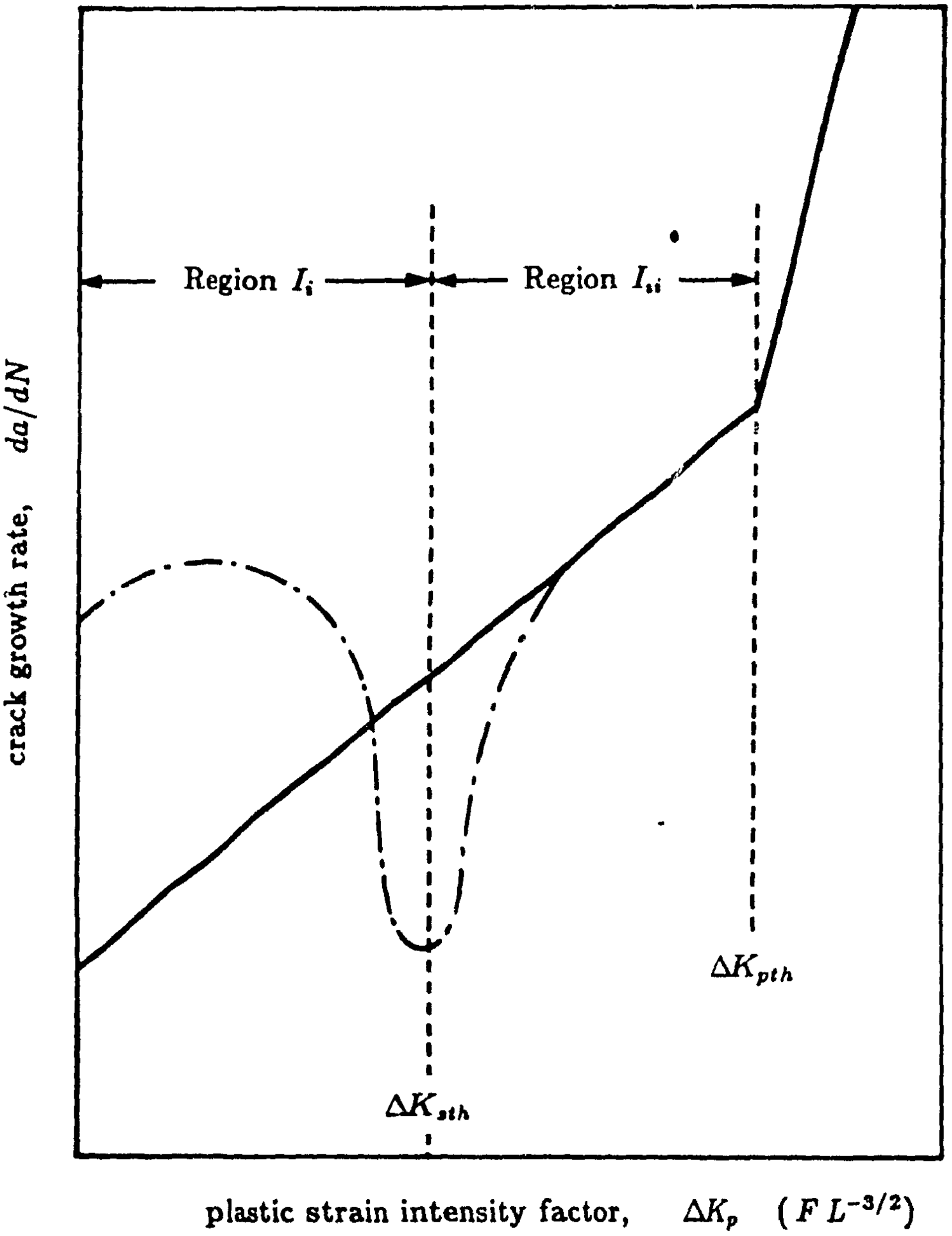

Figure 3.2: Definition of Sub-Regions in Crack Initiation Region.

3.3.2 The Model of Stage I Sub-Microcrack Initiation and Nucleation

Being exposed to the outside, the surface layer of the material lacks "dislocation and breakage stoppers", which are either grain boundaries or mutual atomic bonds inside the material. These stoppers serve to restrict the movement of dislocations and breakage of atomic bonds inside the material. Crack initiation and propagation on the surface is much easier than from the inside of the material. This is the "free surface effect".

For polycrystalline materials under fatigue loading, applied plastic strain level is not the only standard in determining fatigue lives. It is more precise to divide fatigue into low cycle and high cycle fatigue. Low cycle fatigue covers fatigue lives up to $\sim 2\times 10^5$ cycles while high cycle fatigue covers fatigue tests with specimen lives longer than $\sim 2\times 10^5$. In high cycle fatigue, crack initiation is transgranular and the initiation sites are on surface PSBs or slip bands within the grain. In low cycle fatigue, fatal crack initiation is mainly intergranular and the initiation sites are often at surface grain boundaries or PSB (or slip band) interfered grain boundaries. The fatal crack initiation is much earlier in high cycle fatigue than in low cycle fatigue, in terms of the percentage of the total fatigue life.

Earliest extrusion/intrusion on PSBs or any slip bands and the weakest linkage break-up at grain boundaries on the specimen surface compose sub-microcracks. The mechanisms of sub-microcrcak initiation from PSBs are as proposed by Mughrabi, Kuhlmann-Wilsdorf and Laird and Newman *et al* [37]-[44] (refer to Chapter 2). The mechanism of sub-microcrack initiation from grain boundaries is the opening up of weakest links at the grain boundaries by excessive plastic shear strain. Those grains under high strain concentration are especially prone to grain boundary cracking. A high strain concentration at a grain boundary is introduced when the deformations within the grain or grains at one or both sides of it are very limited.

A model of the Stage I sub-microcrack initiation and nucleation mechanism is proposed in Figure 3.3. Figure 3.3 (a) describes the early sub-microcracks either along slip bands or grain boundaries. There are usually several sub-microcracks at the initiation site of a microcrack. They are smaller than the length of the grain boundary or the size of the grain that contains them. They may initiate on the same plane or on different planes, depending on grain boundaries or slip bands.

If the sub-microcracks are initiated on one grain boundary and the grain boundary is straight, the sub-microcracks are on one plane. However, if the sub-microcracks are initiated on a grain boundary that has been interfered with by a slip band, the sub-microcracks will be on both the band and the grain boundary, so they are not on one plane. The sub-microcracks will not be on the same plane either if they are on grain boundaries which are not straight. As for sub-microcracks initiated on slip band, if they are all on one side of the band, they will be on the same plane. However, sub-microcracks of a fatal crack usually initiate in grains larger than the average size and initiate on both sides of the band; in this case, they are not on the same plane.

Due to the free surface effect, the sub-microcracks expand fast and independently, as shown in Figure 3.3 (b). The nucleation of sub-microcracks takes place mainly along a line, although it is an irregular line, as illustrated in (c) and (d). This line is on a maximum shear stress plane with an angle of roughly 45° to the applied load on the specimen surface, reflecting the characteristics of Stage I propagation. The time needed for sub-microcrack nucleation is different for high and low cycle fatigue.

In low cycle fatigue, once the sub-microcracks are initiated at the grain boundaries, the strain becomes even more concentrated in the unbroken parts of the grain boundaries containing the sub-microcracks. As a consequence, the nucleation of the sub-microcracks to form microcracks is fast. In high cycle fatigue, where fatal cracks are initiated either on PSBs or slip bands, the sub-microcrack nucleation process takes much longer to complete. Since the momentum of crack initiation and early propagation is mainly the dislocation motions in PSBs or slip lines (refer to Chapter 2), nucleation of sub-microcracks on different planes is much more difficult than in low cycle fatigue. To cross the layer that separates the sub-microcracks, dislocation motions on planes that are not favourable for slip are needed. The barrier could be either the grain boundaries or the width of the slip band containing the sub-microcracks.

Upon the completion of the sub-microcrack nucleation in Region I_s, a microcrack is initiated and the crack encounters its sub-threshold. Similar to the determination of ΔK_{pth}, ΔK_{sth} is determined at $\sqrt{\Delta J \cdot E}_{sth}$. Therefore, the size of the initiated microcrack at the sub-threshold is also determined at $\sqrt{\Delta J \cdot E}_{sth}$, which may be less than or greater than the average grain size. Low cycle fatigued specimens only have one sub-threshold at microcrack initiation while high cycle fatigued specimens may have more than one sub-threshold, one at the microcrack initiation and others during the sub-microcrack nucleation process prior to the coalescence of some sub-microcracks across planes.

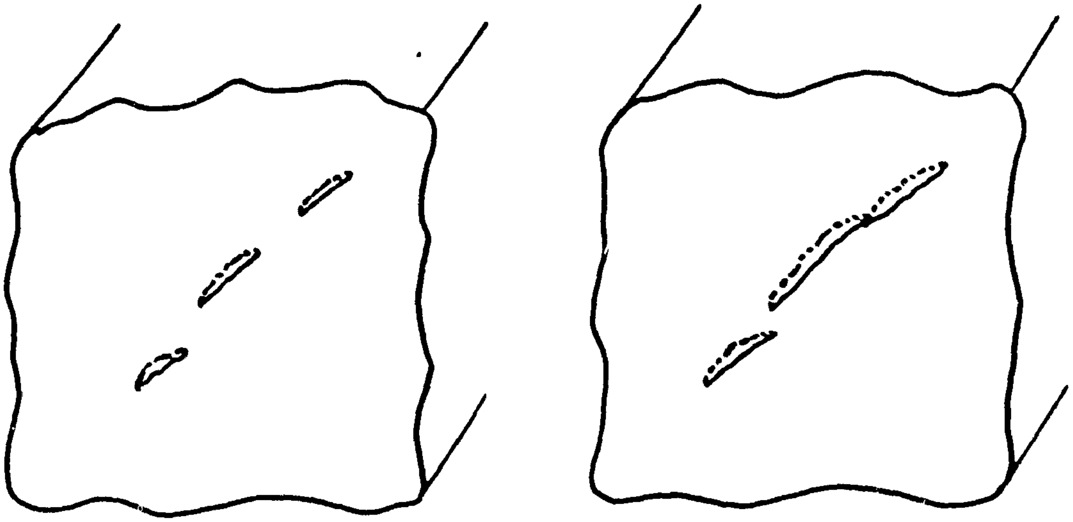

(a) sub-microcrack initiation (b) sub-microcrack growth

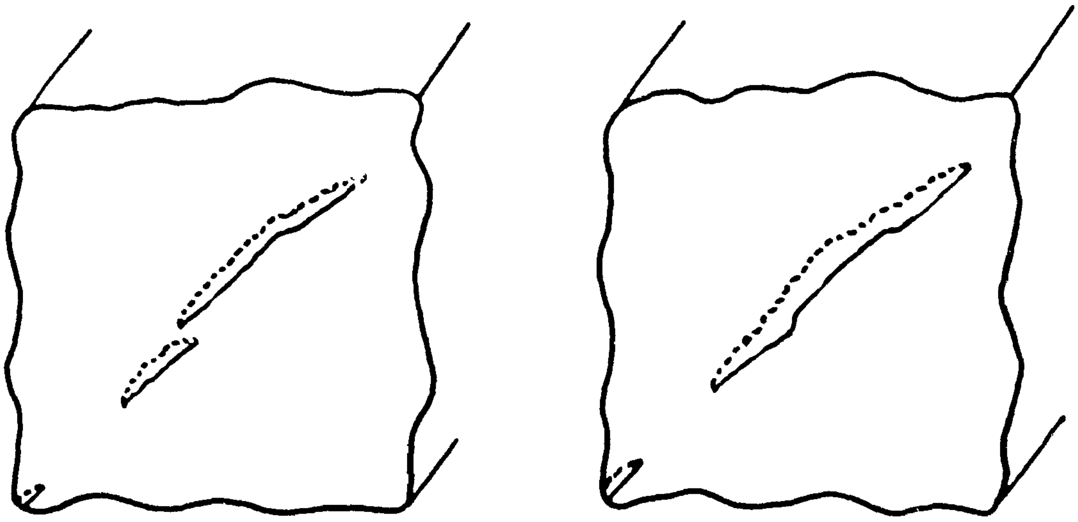

(c) sub-microcrack growth (d) sub-microcrack formation

Figure 3.3 Model of Stage I Sub-Microcrack Initiation and Nucleation in a Cylindrical Specimen. (load direction vertical in the plane of the Figure)

The sub-microcrack initiation and nucleation takes place mainly on the surface of the specimen and is, therefore, a pure surface phenomenon. The crack propagation in the sub-microcrack region is the most complicated in the the entire crack initiation and propagation process. All the factors influencing the short crack propagation (refer to Chapter 2) have their strongest effects on the crack behaviour in this region. The hill and valley of the crack growth curve in this region is but a natural consequence of these influences on the crack growth behaviour.

The Sub-Threshold of Crack Propagation

The sub-thresholds in microcrack initiation are crucial in the crack propagation process. Suppose the neighbourhood is not favourable for a microcrack to continue its growth. It will come to rest and becomes a non-propagating "dormant" microcrack [18]. There are usually many cracks of this type found on the surface of a specimen after tests. Even if the environment is favourable, there being other microcracks in adjacent grains or grain boundaries, the growth rate of cracks that later proved to be fatal will be still considerably retarded at the sub-threshold before its microcracks can amalgamate. The causes for this retardation are:

1. The shallow depth. Although a microcrack may have relatively large surface dimensions, its depth is shallow. According to theoretical analyses [97,98] of the stress intensity along the circumference of elliptical surface cracks in an infinite body, the smaller the ratio of the depth to half surface crack length, the bigger the stress concentration at the crack tip inside the material as opposed to on the surface. Although these analyses are based on continuum mechanics and are derived from the linear elastic fracture mechanics, the combination of these

theoretical analyses and the influence of microstructural factors such as local yielding, closure effect, etc, will provide a special equilibrium condition for the sub-microcracks to grow. At a certain ratio of the crack depth and half the crack length, which is unlikely to be the same as the ratio from LEFM, the stress concentration at the crack tip inside will become bigger than on the surface. This happens when the coalescence of the sub-microcracks has just ended. The higher stress concentration at the crack tip inside serves as a driving force for the tiny cracks to expand into the material. While the crack seems to cease growing on the surface for a long time, it actually never stops progressing. The growth towards the inside continues until a certain depth, where the stress concentration factors along the crack circumference become uniform and surface crack growth resumes.

2. The closure effect. As mentioned earlier in the review, the P_o/P_{max} value of a short crack is -1 at the beginning and converts quickly to a positive value. The retardation of the growth rate at the sub-threshold may correspond to a certain stage of the closure effect.

3. Changing of planes. The initiated microcracks may be or may not be on the same plane. To further coalesce across planes, time is needed.

After overcoming the sub-threshold barrier, the crack enters Region I_{ii}, the microcrack propagation stage.

3.3.3 The Model of Stage I Microcrack Propagation

As at the microcrack initiation site where several sub-microcracks initiate at the same time, the fatal crack initiation site also contains several microcracks. The crack tip at the edge of the infinite body in Figure 3.3 (c) and (d) indicates the existence of another microcrack developing in the neighbourhood. Microcracks are also aligned on a plane with an approximate angle of 45° to the applied load.

Microcrack propagation is a continuation of the sub-microcrack nucleation. Viewing from the surface, the microcrack propagation is similar to the sub-microcrack propagation, which is an independent microcrack growth and coalescence. However, a stereoscopic view of the crack shows an essential difference between the crack propagation mechanisms in the two sub-regions. Sub-microcrack nucleation is two-dimensional and is a pure surface phenomenon, while microcrack propagation is three-dimensional and is a transition from pure surface crack propagation to bulk material crack propagation.

The model of Stage I microcrack propagation in cylindrical shaped specimens is proposed in Figure 3.4 and Figure 3.5. While Figure 3.4 gives the stereoscopic view of Stage I crack propagation along planes approximately 45° to the applied load, Figure 3.5 explains the two typical geometrical surface configurations which have a 45° angle to the applied load direction.

After the Stage I propagation, the initiated crack has a "V" shape on the specimen surface. The line along which the sub-microcracks nucleate is one arm of the later formed "V" shape. Figure 3.4 (a) shows several microcracks formed during the sub-microcrack initiation and nucleation stage. In early microcrack propagation,

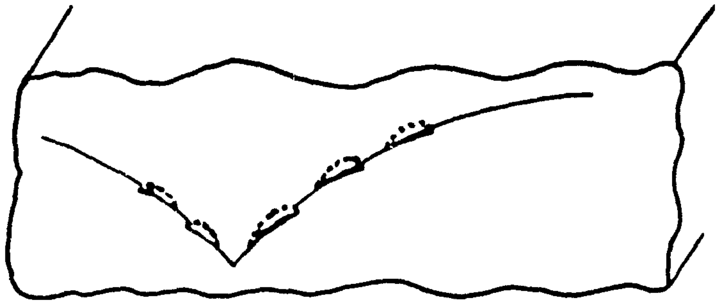

(a) microcrack initiation (b) microcrack growth

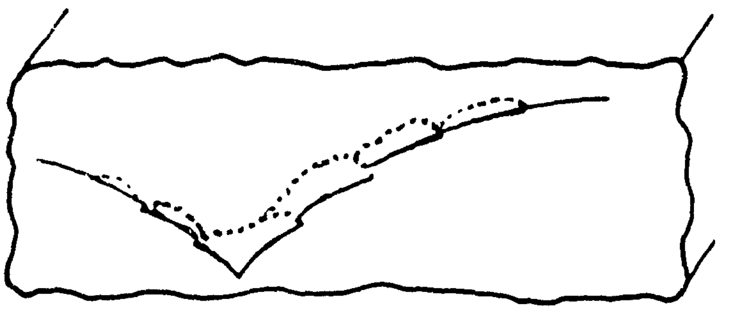

(c) three-dimensional microcrack growth (d) three-dimensional microcrack growth

Figure 3.4: Model of Stage I Microcrack Propagation in a Cylindrical Specimen. (load direction vertical in the plane of the Figure)

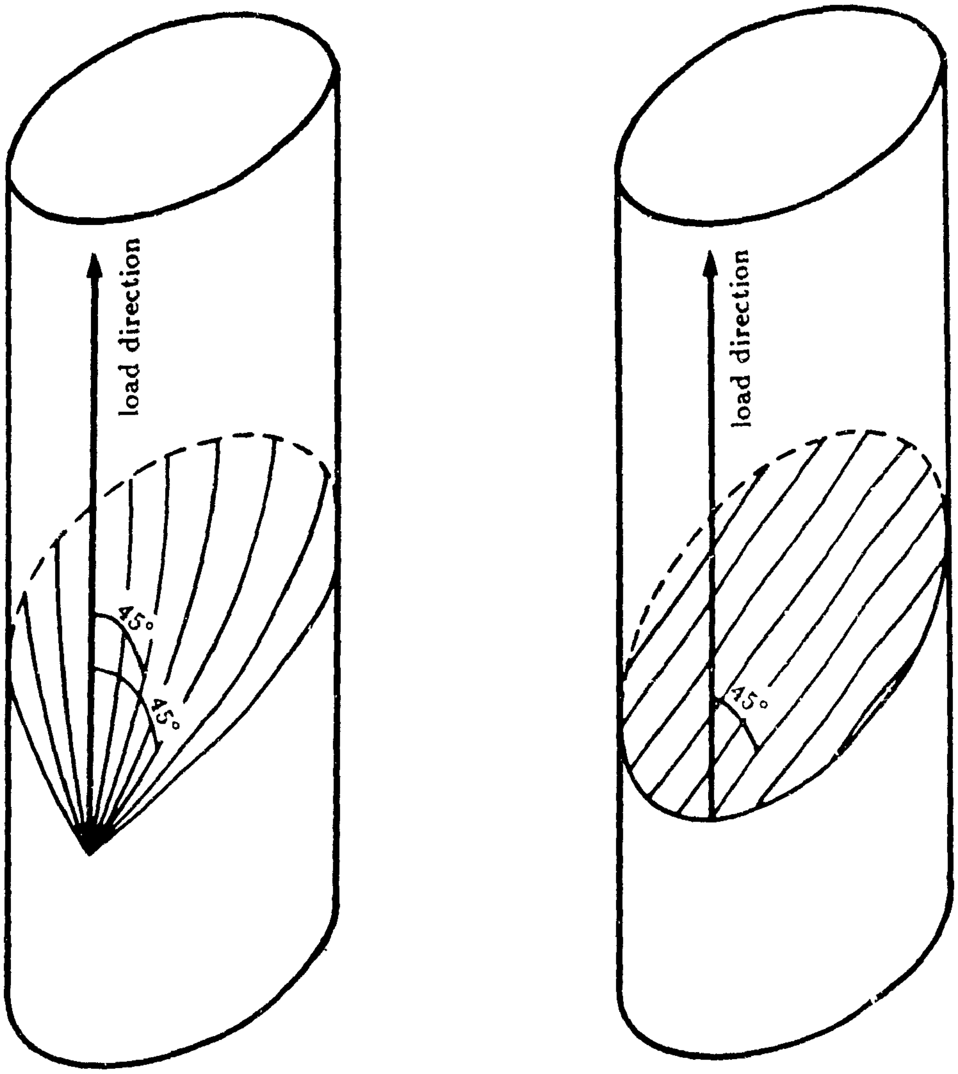

(a) a cone surface

(b) a two-dimensional plane

Figure 3.5: Two Configurations of Surfaces Intersecting a Cylindrical Shaped Specimen on which Stage I Propagation Takes Place.

these microcracks grow and join each other in a two-dimensional manner on one or both sides of the "V", until the size of the joined microcrack on one side reaches such a limit that three-dimensional microcrack propagation is ready to take over, as shown in Figure 3.4 (b). Figure 3.4 (c) reveals that the bottom part (a formerly independent microcrack) of one end of the joined microcrack has expanded along a surface over to the other bank of the "V" on the specimen surface, forming the first semi-elliptical shaped crack. The surface on which the expansion takes place will be discussed shortly. At the same time as the surface crack lengths increase, the second expansion process is completed as shown in Figure 3.4 (d). Similarly, the third and the fourth expansion processes are completed. As shown explicitly in Figure 3.4, the microcracks may not always initiate on the same plane. Owing to the steps formed when microcracks on different planes join, ripple lines are left at the initiation site. The ripple lines help the recognition of Stage I propagation on a fractographic surface.

Theoretically, there are two possible configurations of planes that have a 45° angle to the applied load, as shown in Figure 3.5. One of them is a cone surface configuration. A representative cone surface is depicted in Figure 3.5 (a). Its vertex is at the tip of the "V" on the specimen surface. All the elements on the cone surface have an angle of 45° to the line passing the vertex in the loading direction. The intersection of this cone surface and the specimen surface around the vertex of the cone forms a "V' shape curve when viewed from a point on a line perpendicular to the specimen surface at the crack tip.

Figure 3.5 (b) demonstrates a representative plane of another surface configuration that has a 45° angle to the applied load. It is a two-dimensional plane whose normal direction $\vec{N}$ has a 45° angle to the applied load. The intersection of this plane and the specimen surface forms an elliptical curve when viewed from above-mentioned point. This curve is much smoother than the "V" shape.

The Stage I propagation actually takes place on both surfaces presented in Figure 3.5. The earliest expansions from one side of the "V" to the other are along the cone surface. There are reasons why Stage I microcrack propagation starts on the cone surface. On the specimen surface, the angle between microcracks on the two arms of the cone surface is around 90°, while the angle of microcracks on the two-dimensional plane in Figure 3.5 (b) is much bigger than that. The smaller angle between the microcracks on the cone surface is favorable for further crack expansion by microcrack coalescence. However, the intersection of the cone surface and the plane perpendicular to the applied load is too sharp for the crack to transit smoothly from Stage I to Stage II propagation. On the other hand, the intersection of the two-dimensional plane in Figure 3.5 (b) and the plane perpendicular to the applied load is much milder. The expansion is therefore forced to shift gradually to the two-dimensional plane in Figure 3.5 (b), and crack propagation gradually becomes uniform along the crack circumference.

In low cycle fatigue, Stage I propagation is normally intergranular, with a path mainly along those grain boundaries having an favourable angle (close to 45°) to the applied load, but occasionally along an favourable slip plane. In high cycle fatigue, Stage I propagation is mainly transgranular with a path mainly along favourable slip planes ("well-defined crystallographic planes" [56]), but occasionally along favourable grain boundaries. However, due to the larger crack size, the later part of the Stage I propagation path in high cycle fatigue may encounter grains with unfavourable main slip systems. These grains are then torn open in the Stage II propagation manner and fine "step marks" are left at the crack initiation site on the fractographic surface. They are called "step marks" to distinguish them from "striations" which are a one-to-one manifestation of damage occurring during one fatigue cycle.

In the very special manner of Stage I crack propagation, the microcrack enlarges itself both on the surface and the inside of the material until it reaches the plastic crack propagation threshold. Then Stage I crack propagation comes to an end and Stage II, the crack propagation perpendicular to the applied load, takes over.

The Plastic Crack Propagation Threshold

The transition of crack initiation to propagation takes place at the plastic crack propagation threshold, ΔK_{pth}, after which the crack growth style changes to Stage II and the growth rate increases steadily. On reaching ΔK_{pth}:

1. a crack with a rough semi-elliptical shape is formed, although the aspect ratio of this semi-ellipse may be small,
2. a macroscopic stress concentration field at the crack front is established, and
3. Stage I propagation gives way to Stage II propagation.

The first few semi-ellipses formed during Stage I microcrack propagation are not regular ones because of the long handles sticking out from their major vertices. The handles are the already coalesced shallow surface cracks as shown in Figure 3.4 (c). As the crack shape changes from a line crack to a semi-elliptical crack with a long handle at one of its major vertices and then to a regular semi-ellipse, the crack propagation changes from a surface phenomenon to a bulk phenomenon. The establishment of the macroscopic stress-strain field is based on the semi-elliptical crack shape formation, while the subsequent Stage II crack propagation compatible to that predicted by LEFM or EPFM method is ensured by this macroscopic stress-strain field

3.3.4 Crack Profile Changes and Closure Effect Analysis in the Initiation Region

In proposing the two models of sub-microcrack and microcrack nucleation, the profile of cracks inside the material at very short crack lengths was implicitly proposed as well. Figure 3.4 can be used to define crack profiles in the initiation region.

The crack profile study is also divided into the two sub-regions shown in Figure 3.2. In Region I_i, the crack profile is long and narrow, lying on an irregular line, as shown in Figure 3.4 (a) and (b). The crack profile in this sub-region is approximately on a two-dimensional surface. The aspect ratio λ is very small and the crack does not really have a semi-elliptical shape.

In Region I_{ii}, cracks start to grow more to the inside. After the first expansion from one side of the "V" to the other side, the first semi-elliptical shaped crack profile appears, as shown in Figure 3.4 (c). This is a turning point in the crack profile because it now becomes three-dimensional. At the early stages of Stage I microcrack propagation, however, the semi-ellipses are not regular because i) they have long handles sticking out from their major vertices; and ii) they are not plane semi-ellipses but are on the cone surface described in Figure 3.4 (a).

As the Stage I propagation shifts to the plane in Figure 3.4 (b), the crack profile advances one step towards a regular semi-ellipse, for it is on a two-dimentional plane.

By the end of Stage I propagation, the crack profile has developed even further towards a real semi-ellipse. However, reaching the end of Stage I propagation does not mean that the crack has gained a semi-elliptical shape with the aspect ratio λ close to unity. Although the aspect ratio λ keeps increasing during the entire crack initiation, the semi-ellipse at the end of Stage I propagation may still have a small λ ratio, especially in low cycle fatigue. Besides, the handle at one major vertex of the crack does not necessarily disappear at the end of Stage I propagation. In high cycle fatigue, λ may increase to a value close to unity at the end of Stage I propagation.

The crack profile change is a measure of the "closure effect" or the "free surface effect" which are important in both crack initiation and short crack propagation studies. In fact, the closure effect is so important that it has to be included in the function $\mathcal{F}$ in Eqn (3.1). The closure effect is the reverse of free surface effect. At a free surface, the closure effect is zero while the free surface effect is at the maximum. The shallower the crack, the stronger the free surface effect, hence the faster the crack growth. A change from a line crack to an approximate semi-circular crack indicates a change in the free surface from the maximum to zero.

In low cycle fatigue, since the aspect ratio λ is still small at the plastic crack propagation threshold, ΔK_{pth}, λ keeps increasing in the Stage II propagation until it gets close to unity. That means the free surface effect does not decay completely at the plastic propagation threshold but carries on into the Region *II* crack propagation. The knowledge of the free surface effect will greatly help solving problems in predicting Stage II crack propagation life.

Chapter 4

TESTING APPARATUS, EXPERIMENTAL TECHNIQUE AND PRELIMINARY RESULTS

4.1 Introduction

Experimentation is the only reliable way to test scientific theory. In many complicated situations where theoretical calculation is not possible, experiments become the only way to reveal the nature of the basic physical process being studied. This is especially true in fatigue analysis. No existing analytical analysis is available that involves all the areas of continuum mechanics, micromechanics, elastic-plastic fracture mechanics and material science. Most formulas in fatigue analysis accepted by engineers are empirical laws obtained through experimentation.

Closely tied to the evolution of the empirical model for fatigue crack initiation and early propagation described in last chapter was the development of an experimental program. This chapter describes the experimental techniques adapted and developed during this investigation, the procedures finally adopted in the experiments and some preliminary testing results.

4.1.1 Test Outline

The test outline was drawn from the "standard practice for conducting constant amplitude axial fatigue tests of metallic materials"—ASTM designation: E 466-82 and the "standard recommended practice for constant amplitude low cycle fatigue testing by American Society for Testing and Materials"—ASTM designation: E 606-80. Both cover the procedures for the performance of axial fatigue tests to obtain the fatigue strength of metallic materials by the use of uniaxially loaded test specimens in any environment and temperature.

The two standards contain certain apparatus requirements. First of all, a tension-compression fatigue testing machine with well aligned fixtures for grasping the two ends of the specimens is required. The load and deformation transducers should be placed in series with the test specimen for the purpose of sensing and measuring the magnitude of the axial load transmitted through the specimen. The test recording facilities should at least include a cycle counter and hysteresis loops of load versus deformation or stress versus strain recording facilities, such as an X-Y recorder. Finally, it is suggested that calibration of the machine should be done often to maintain required accuracy.

The major difference between the two standards is that while the range of E

466, the tests have to be under load control and the report mainly requires the information of a $S - N$ (stress versus life) curve; whereas E 606 tests have to be under total strain control through extensometers (one of which is electromechanical, including the strain gauge extensometer adopted in this investigation) measuring the deformation in the gauge area throughout the cycles. What are expected from the report of E 606 tests are the:

1. determination of the cyclic stress-strain curve,
2. determination of the strain-life relationship, and
3. post-mortem examination—metallographic examination of the fractographic surface of failed specimens.

Since the purpose of this investigation concerns the study of fatigue damage and these two standards are the most relevant, the testing program used them as guidelines. The specimen design, testing apparatus, etc., were chosen under the guidelines of these two standards. However, it could not follow them entirely since several modifications had to be made to meet the investigation's objective fatigue crack initiation studies. For example, to reveal the relation between fatigue life and the cyclic stress-strain curves for polycrystals, tests had to be performed under plastic strain control instead of total strain control. Besides, results obtained under plastic strain control are more compatible, since constant plastic strain controlled tests are often reported in the literature of fatigue mechanism studies.

Due to the choice of smooth cylindrical specimens for testing, the large testing area made it impossible for either the optical microscope or the scanning electron microscope to observe the crack initiation and early propagation directly. Therefore, the crack initiation and early propagation history of specimens had to be recorded by plastic replicas for post-mortem studies. Replication technique will be discussed in detail later in this Chapter. Finally, the results of this investigation concern only the mechanisms and analysis of crack initiation and short crack propagation, not the determination of the cyclic stress-strain curve or the strain life relationship.

4.2 Specimen Design

4.2.1 Testing Material—OFHC Copper

As described in the review Chapter, many fatigue crack initiation mechanism studies have been carried out on copper single crystals owing to copper's typical face-centered-cubic (fcc) structure which is favourable to PSB formation. The distinguishable striations left on fractographic surfaces and easy availability have made copper alloys a commonly used material in general fatigue propagation studies. Since the present study is a fundamental research of degradation processes under fatigue loading, it was considered advisable to choose a material possessing typical fatigue crack initiation and propagation properties such as copper, since the results obtained from experiments are not only more easily summarized, but also easily compared to those found in the literature. It was for these reasons that certified oxygen-free high conductivity copper (OFHC) was chosen as the testing material.

The 12.7 mm diameter round bars of OFHC copper were in hard drawn condition when received from AMAX Base Metal Research & Development, Inc. of New Jersey, U.S.A. Their chemical composition is a minimum of 99.99% copper with the impurity analysis listed by the company in Table 4.1. The mechanical properties of each specimen after annealing will be dealt with individually in Chapter 5.

element	ppm	element	ppm	element	ppm
Ag	13	As	<3	Sb	4
Pb	5	P	<3	Bi	0.6
Te	<2	Sn	1	Zn	<4
Ni	3	Cd	<1	Mn	2
S	15	Fe	<5		

Table 4.1: Impurity Analysis of the Tested Material—OFHC Copper.

4.2.2 Specimen Design

The basic specimen configurations recommended in both standards are cylindrical in shape with a solid circular cross-section in the test area, as shown in Figure 4.1. One is a uniform-gauge specimen and another has a hour-glass profile. Specific cross-sectional dimensions of the uniform testing section configuration, as indicated in Figure 4.1 (a), are given in the E 606 only because they have been predominant in the generation of the low-cycle fatigue data that exist in the open literature. The standards also suggest alternative specimen designs for sheet specimens.

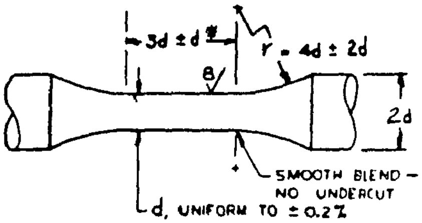

(a) UNIFORM-GAGE TEST SECTION

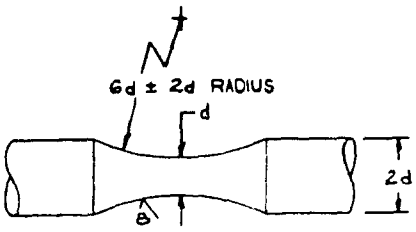

(b) HOUR-GLASS TEST SECTION

NOTE—Dimension *d* is recommended to be 6 35 mm (0 25 in).

Figure 4.1: Recommended Low-Cycle Fatigue Specimens.

The selection among these specimen shapes depends on the purpose. The sheet specimens were discarded with a clear reason: unwanted corner effects. The advantage of the hourglass cylindrical specimen design is the buckling resistant shape for withstanding higher strain amplitudes. However, it is difficult to manage the strain controls in this specimen shape. Besides, the influence of stress concentration due to the shape on the crack propagation path cannot be evaluated. Thus the uniform cylindrical specimen shape was the remaining option.

As pointed out by the standard, although the recommended uniform gauge specimen is frequently suitable for strain ranges up to about 2%, soft material or elevated temperatures may dictate lower strain ranges, which is what occurred in the preliminary testing of some dummy specimens. Copper is a soft material, and annealed copper even softer. When the specimens were tested in the hard drawn condition, tests ran easily to 0.4% of total strain without any buckling problems. When it came to annealed copper specimens, the tests could not be performed above 0.3% because of specimen buckling. That means the uniform gauge specimen configuration can only accommodate a very limited high strain level.

Dummy specimens were machined to the specified cross-sectional dimensions recommended by the standard E 606 (refer to Figure 4.1 (a), and tested. In this manner the standard configuration was found not to be appropriate for this investigation. With a strain extensometer gauge length of a quarter inch (the same as the testing section diameter), the replica making and observation of the specimen surface in the test section became too difficult. Fortunately, E 466 mentions that the grip cross-sectional area should be at least 1.5 times, although preferably 4 times the test section area. Considering that the testing range in this investigation is between high strain and low strain fatigue, with material conditions determined by the physical dimensions of the supplied material, it was decided that the minimum ratio of 1.5 would be appropriate for this work.

This requirement and others for specimen dimensions from E 466 dictated that the specimen design should satisfy the following;

$$\frac{D^2}{d^2} \geq 1.5, \tag{4.1}$$

$$\frac{R}{d} \geq 8, \tag{4.2}$$

$$3 < \frac{L}{d} > 4, \tag{4.3}$$

where D is the diameter of the two ends of the specimen, d the diameter of the testing section, R the blending fillet radius and L the length of the testing section.

The first relation has already been discussed. The second requirement is to minimize the theoretical stress concentration of the specimen, and the last is to minimize buckling or excessive bending during tests. For round bars of 12.7 mm diameter, the parameters are calculated to be d = 9.5 mm, R = 76.2 mm and L = 29.5 mm. The final dimensions of the specimen are shown in Figure 4.2.

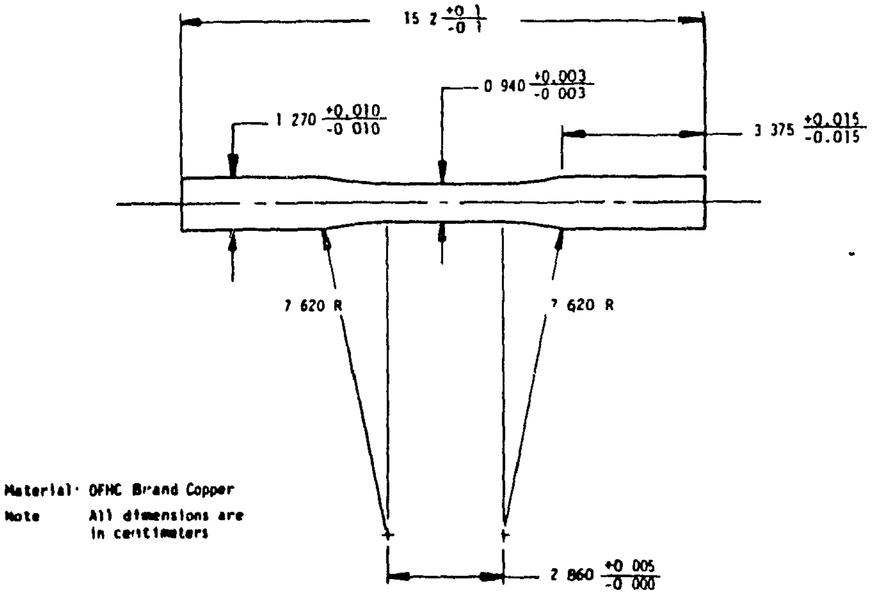

Figure 4.2: Specimen Dimensions Used in this Investigation.

4.2.3 Specimen Preparation

Machining

The condition of the specimen and the method of specimen preparation are of the utmost importance in tests. Improper methods of preparation can greatly bias the test results. The specimen preparation procedures for this investigation followed the guideline of the standards, yet were not restricted to them. Different methods of the preparation were tried and compared. As long as they were considered as favourable to the objectives of this job, they were accepted.

First, the machining of the specimens was performed by the Machine Tool Lab. in McGill university on a numerically controlled lathe to a precision described in Figure 4.2. Heat treatment was performed after machining so that the residual stresses left on the surface by machining could be avoided.

Heat Treatment

Annealing of cold worked metal to obtain a good combination of ductility and strength is accomplished by heating to a temperature that produces recrystallization. In order to remove the residual stresses left on the specimen surface by machining and to show typical properties of OFHC copper in its annealed condition, all specimens were annealed in a Lindberg Hevi-Duty furnace preheated to the desired temperature and cooled in air. No attempt was made to prevent the specimen from oxidizing since the specimens were to be polished. The annealing time for the four successfully tested specimens was 25 minutes, while the annealing temperature was 400°C for three of the specimens and 450°C for the remaining one.

It must be mentioned here, that the material is very sensitive to annealing time and temperature in the range involved; for small variations in either the temperature or annealing time, the material properties could be very different. This point will be further discussed in Chapter 5.

Polishing

The preparation of the specimen surface was especially crucial in this investigation. Great attention had to be paid to make sure that the specimen cross-sectional area was as uniform as possible. Due to the softness of copper there is a tendency, in machining as well as polishing, to overcut at the area of transition from the uniform test section to the fillet. Before the overcut was corrected, it was found while testing dummy specimens that cracks always started at this part of the testing section.

Secondly, no scratches normal to the applied load can be left on the surface; otherwise the crack would certainly start at the scratches, so the study would pertain to "short crack propagation" instead of "crack initiation". Moreover, the observation of the crack initiation and propagation mechanisms requires a very fine finish of the specimen surface. It was found that with a surface finish stopped at a step of metallurgical paper 0000, almost no slip lines could be located; while for the same strain level, many slip lines were observed at a finer surface finish with diamond paste with an average size of 1 μm.

To achieve a perfect smooth surface, the first choice was electropolishing, as suggested by the standard E 466. The principle of electropolishing is that by charging the specimen as an anode the electrons on the surface of the specimen are attracted by the cathodes through the electrolyte. The peaks on the surface have a higher current than the valleys; therefore the peaks dissolve faster than the valley. A typical electropolishing device is shown in Figure 4.3. The advantages of electrolytic polishing of copper are listed as:

1. it is excellent for revealing grain size and shape on all sides of specimens,
2. it is especially well-adapted to use on single-phase copper alloys, and
3. it reveals the true microstructure with less difficulty, compared with mechanical polishing.

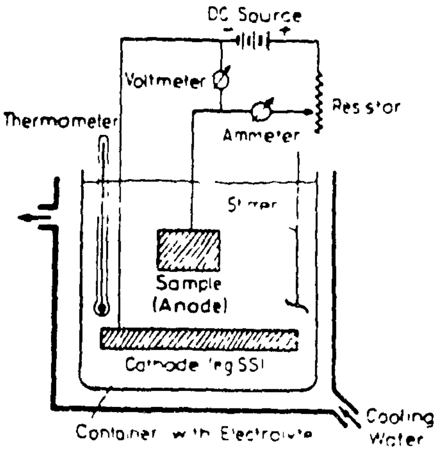

Figure 4.3: Electropolishing Equipment.

A simple electropolishing device was designed in the laboratory: a stainless steel container holding electrolyte. Two copper sheets were curled and inserted as the cathodes and the specimen stood in the center as the anode. With this device, specimens were electropolished with several electrolyte groups that are recommended for copper; the major chemicals in these are phosphoric acid (H_3PO_4) and distilled water.

After electropolishing, the specimens were bright, shiny, and seemed to be perfect to the naked eye. Unfortunately, a closer examination under the optical microscope with a magnification of 70 revealed many pits on the surface, most of which were small, but some were as big as 10 μm. This could not be improved by just changing the shape of the device or electrolytes.

These pits could not be permitted in the present study, and therefore electropolishing was not employed. Although mechanical polishing cannot avoid leaving polishing lines behind at the final step, the orientation of the lines can at least be controlled so that they run parallel to the applied load. Therefore, all specimens were mechanically polished by hand.

Polishing started with 220 emery paper and went down in sequence of 400, 600 emery papers; then metallurgical paper 0, 00, 000, 0000; after that the diamond pastes in the sequence of 12, 9, 6, 3, 1, 0.5 μm; and then a final polish of 0.1 μm. At each step, the polishing direction was perpendicular to the previous one. The specimens were continuously examined by an optical microscope to make sure that no trace of the last polishing step remained. The examination was extremely careful at the last steps to make sure that no polishing lines perpendicular to the load, the direction of crack initiation, were left.

The final dimension of specimens after polishing were measured by means of a Nikon V-16 profile projector, because any other kind of measuring tools would have left scratches on the specimen surface. The final testing area diameter is around 9.3

mm with an error of less than 0.05 mm.

To prevent excessive air corrosion of specimens, polishing was usually finished the night before testing and then the specimens were stored in an airtight plastic container with desiccant.

4.3 Testing Apparatus and Experimental Technique

4.3.1 Material Testing System MTS 880.14

Introduction

The test rig in this investigation was a servo-controlled hydraulic unit, Material Testing System (MTS) automated test system 880.14. Figure 4.5 is a photograph of the overall system. The system is composed of a loading unit where specimens are subjected to fatigue loading, a hydraulic power supply which provides the energy the actuator rod requires to move up and down and a control console cabinet. The block diagram of the MTS working system is given in Figure 4.8. The following sections describe the functions of the loading system, the power supply and the control cabinet.

The loading Unit

The load frame model 312.21 of the MTS system with a capacity of 100 kN is the major component of the MTS system. It consists of grips for holding the specimen, a stiff load cell for monitoring the load on the specimen, a hydraulic service manifold providing hydraulic filtration, an actuator which applies the loading to the test specimen within the load frame, and servovalves mounted on the actuator for monitoring the hydraulic flow into the actuator.

In the MTS system, a test can be performed in any of the three controls:

1. load control, where the load level is transferred to and measured by the load cell fixed on the cross head,
2. strain control, where the strain level is measured by the strain extensometers attached on to the specimen, and
3. stroke control, where the displacement at one end of the specimen (the same as the displacement of hydraulic cylinder) is measured by the Linear Variable Differential Transformer (LVDT) transducer situated inside the hydraulic cylinder (piston rod).

Fatigue testing requires precisely controlled levels of force, strain or displacement to obtain meaningful test data. The key to this is precisely and accurately controlled hydraulic cylinder movement, speed and direction, all of which depend on the hydraulic flow to the test actuator throughout the test. This was accomplished by the closed-loop control in MTS.

The amount and direction of hydraulic flow to the hydraulic cylinder is regulated by the servovalve and is directly proportional to the electrical input current from the controller. The controller generates one output signal to the servovalve and accepts two input signals, the program signal as the output from the program function generator and a selected feedback signal which is generated by the load cell sensor, the LVDT position sensor, or the strain extensometer. After receiving the command signal and generating the first controlling signal to the servovalve, the controller continuously measures the feedback signal and compares it with the desired command input. The difference between the measured value and the command value from the program provides a continuous correction signal to the servovalves. The servovalves balance the signals by regulating the direction and rate of flow of hydraulic fluid to the actuator. Thus the closed-loop control allows a precise execution of the program command.

To make the closed-loop control work well, the hydraulic oil flowing into the actuator must be of high quality. The MTS Model 294.11 Hydraulic Service Manifold is designed for this purpose. It is connected in the hydraulic lines between the hydraulic power supply and the servovalves, and consists of two piston accumulators, a pressure filter, and a check valve. It provides hydraulic filtration and suppresses line-pressure fluctuations in high-response, hydraulic actuators.

The maintenance of the manifold includes periodically changing the filter element, cleaning or replacing the associated "O" ring, and checking the precharge on the accumulators. Before and during tests, the filter element MOOG Inc, 071-60299 was checked and changed; the "O" ring No. OR-136 for sealing was replaced before tests. Following the steps listed in MTS Service Bulletin 930.02-5, the return line accumulator was replenished to 3.45 bars and the high pressure line accumulator to 68.9 bar with dry nitrogen and maintained during the tests.

The following gives some concrete information of the load cell, the self-aligning grips, and the extensometer used during the tests. The load cell 661.21A-03 (strain gauge type) manufactured by Lebow Associate Inc. has a matching capacity with

Legend

(1) Digital Decwriter II Terminal (2) Tektronix 4631 Hardcopy Unit (3) Tektronix 4010-1 CRT (4) MTS 880.14 Automated Test System (5) MTS 22 Kip Loading Frame (6) Specimen in Grips with COD Gauge attached (7) COD Gauge Calibration Apparatus (8) Tektronix Oscilliscope

Figure 4.4: The MTS System.

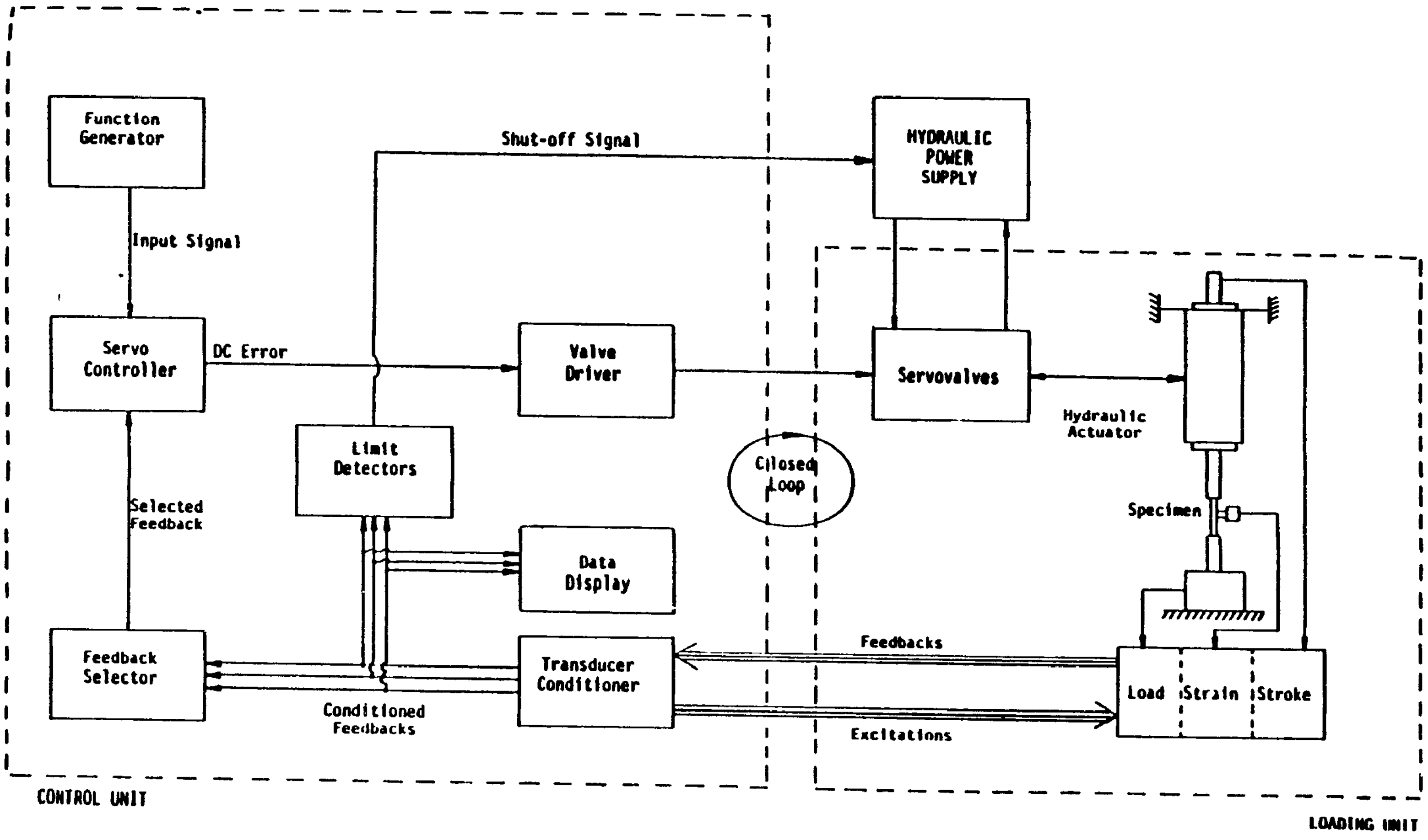

Figure 4.5: The Block Diagram of MTS 880.14.

the load frame of 100 kN. A Morehouse Proving Ring #843 (91 kN capacity) was used to calibrate the load cell. The deviation from linearity was less than 1%.

The self-aligning Model 641.1X Hydraulically-Operated Grips were used in the experiments for this investigation. The specimen can be cycled from full tension through zero to full compression with no backlash. Accurate specimen alignment is assured through symmetrical grip design and the spherical seat angular alignment.

The strain amplitude of the specimen was controlled by a uniaxial extensometer 632.11c-20 with a gauge length of 25.4 mm. This extensometer has a capacity of 0.15 strain and maximum operating frequency with negligible distortion of 100 Hz. The precision of the extensometer was checked by means of a micrometer having a 2.54 μm accuracy. The errors were all within the recommended calibration ranges from the MTS manual.

Hydraulic Power Supply

MTS Model 506.20 hydraulic power supply possesses a 50 HP electric motor and a 50 gallon capacity reservoir. The motor drives a pump to provide a source of hydraulic power at 76 liters/min. The output pressure for the low or bypass state is approximately 2 MPa, and the high condition is adjustable up to a maximum continuous pressure of 20 MPa.

The accumulator was often checked during tests and, when necessary, recharged with dry nitrogen to the required level. The high pressure filter was replaced before testing, and the hydraulic fluid was replaced a month prior to the experiment, following the MTS Service Bulletin 930.22. After the reservoir was completely drained and cleaned, fresh Mobil DTE 25 fluid was pumped into the reservoir through a Model 590.01 Fluid Transfer Pump which provides 10 micron filtration. Filtration of hydraulic oil is an important step since all commercial hydraulic fluids, as supplied, have a contamination level above that recommended for MTS systems.

MTS 880.14 Automated Controller

The controller contains the electronics necessary for controlling the above mentioned closed loop electro-hydraulic testing system. The "automation" in an MTS automated testing system is due to the 433 Processor Interface and a computer. It contains the servo controller and valve amplifier, transducer conditioners, feedback selection, control unit, PDP 11/04 control processor, DEC RX11 Disk System with RX01 Desk Drive, DECwriter, graphics terminal Tektronix, and a Tektronix 4631 hard copy unit.

The Control Unit is an MTS 436.11 control panel that contains all hydraulic, counter, console power, and program run/stop controls. The hydraulic controls allow the hydraulic system to come on-line slowly, minimizing starting transients, by starting the system first in LOW PRESSURE at 2 MPa (refer to Section 4.3.1). HIGH PRESSURE up to 20 MPa is applied after the system has stabilized. The function generator provides a positive or negative-starting triangular, square or sine program waveforms.

The Model 442.11 Controller is a major part in the cabinet which fulfills all of the major functional electronic requirements of the closed-loop control function. Almost all of the controls and indicators located on the front panel of the 442.11 Controller are associated with a particular module located inside the Controller, their functions will be introduced together with the modules in the following paragraphs.

1. Model 440.21 DC and 440.22 AC Transducer Conditioners control the range selection and zero balance of the transducer. By setting the range to 4 in the DC Transducer for strain control, the 10 volt output from the strain extensometer 632.11c-20 corresponds to a strain range of 0.015. Before testing, calibration of the LVDT AC Transducer, the strain and load DC Transducers was carefully done following recommended MTS procedures.
2. The major executor of the closed-loop control is the 440.13 Servo Controller. Its primary function is to develop a DC error signal by comparing a composite command signal with a feedback signal. The DC Error signal serves as an input to a valve driver which in turn applies an output to the servovalve. The polarity and magnitude of the valve driver output causes the servovalve to open in the direction and amount required to move the actuator in the direction that reduces the DC Error. When the DC Error is reduced to zero, the valve driver output reduces to zero and the servovalve closes.

The SET POINT and SPAN 1 are used to adjust the static and dynamic levels of the program input to the value desired by the operator. The "set point" is calibrated at 500 when the piston is at a position with an electronic output of 0 voltage. According to the output voltage, which is reflected both in the output from the Digital Indicator 430.41 and in the null meter situated in the center of the control panel, the later position of the piston can then be determined relative to the calibrated position. After installing the specimen at set point 500, turning the set point knob left and right causes a compression and tension force on the specimen.

SPAN 1 controls the limiting amplitude of vibration, in our case the strain amplitude. The calculation of the SET POINT and SPAN value to meet the desired stress or strain amplitude is demonstrated in MTS Reference Manual, Volume 1, Servo Controller section. Calibration of SET POINT and SPAN, adjusting of the Null Detector, and Comparator Zero were also performed following the manual before tests.

The error signal from the servo controller is amplified by the 440.14A Valve Driver which drives the servovalves. Servovalve balance was frequently checked and adjusted during tests. The position of REMOTE/LOCAL switch in the Model 440.32 Feedback Selector decides whether the system is going to be in computer control or manual control. The CONTROLLER GAIN in the Feedback Selector determines the speed of system response to a specific error signal. The adjustments of controller gains in the Feedback Selector panel are necessary to optimize system speed of response to the control signal derived from the test program and the selected feedback source. The controller gain for load, strain and stroke were all adjusted to make sure that they were neither too high nor too low. The safety lock in MTS is the Model 440.41 Limit Detector. By detecting an upper and a lower limit in load, strain and stroke, the hydraulic system shuts off automatically, thus preventing unwanted damage to the machine or specimen.

Series 433.3X Processor Interface Unit is used to provide computer control of MTS closed-loop electrohydraulic testing systems. The Interface Unit is the communication link between a small general purpose computer and the testing system. It includes all of the functions necessary to operate a system in real time and to carry on communications between the computer and the testing system. Basic requirements for 433 configurations include a chassis, a power supply, a Power Fail Detector circuit card, and the PDP-11 Computer Bus Converter subsystem. Individual circuit cards are added to suit the particular system. The interface devices also contain a Data Buffer Register (DBR) which retains data until the computer or interface device can use it. DBRs may be read only, write only, or read/write registers. It is through this hardware interface unit, the Digital Equipment Corporation Model PDP-11/04 Computer is connected to the MTS 880.14 Control Unit.

The PDP 11/04 is used for controlling command profiles, acquiring data from the specimen and computing test results. It contains an input/output bus which interconnects the 433 Processor Interface and all peripherals. It has a cycle time of 725 nanoseconds with a storage capacity of 16,384 sixteen-bit words. The operating system once loaded interacts with the keyboard from the Tektronix Graphics Terminal or the DECwriter to set up test parameters.

The combination of 433 Processor Interface (built in the control console), Digital PDP11/04 Computer (built in the control console), and the peripheral devices includes the RX01 Disk Drive, the DECwriter, the Tektronix 4010-1 Terminal, and a Tektronix 4631 Hard Copy Unit, as shown in Figure 4.4, comprises the hardware required for the computer control of the MTS system.

Tektronix 4010-1 Terminal permits direct on-line communication with the computer through a keyboard and readout. The output may be transferred to DECwriter for print out or to a CRT display which can operate in alphanumeric mode or combination alphanumeric and graphic mode displaying data in the form of graphs and pictures. Furnished with the 4631 Hard Copy Unit, a permanent copy of displayed data can be obtained at any time.

MTS has implemented a number of real-time routines, written in assembly language MTS BASIC/RT-11, which is a single-user, conversational programming language, that interfaces with the MTS 433 Hardware Interface Unit. Among them, the "Constant Amplitude Low Cycle Fatigue Test" is the most relevant to this research. In fact, the program controlling all the tests in this investigation, CATMP — The Constant Plastic Strain Amplitude Fatigue Test, is a modification of this program.

4.3.2 The Controlling Software

Constant Plastic Strain Amplitude Fatigue Testing Program—CATMP

The "Constant Amplitude Low Cycle Fatigue Test—CAMP.BAS" was supplied by The BASUS Users Society operated by the Software Products Division of MTS Systems Corporation. It is written for fatigue tests with smooth cylindrical specimens cycled between constant amplitude, completely reversed, strain limits conducted under strain control at a constant rate. In the program, stress, strain and plastic strain amplitudes are calculated and printed for logarithmic and numeric cycle intervals.

CAMP was modified by L. Achard, of Dominion Engineering Works Ltd. and called CATM. It has a slightly different plotting format, as well as the ability to conduct tests at a higher frequency than CAMP. The procedures for running CATM can be found in Reference [99].

Based on the program CATM, the Constant Plastic Strain Amplitude Fatigue Testing Program (CATMP) was developed for the present investigation. In this program, the plastic strain control is accomplished through the same principle as described for the MTS system—closed loop control.

Since MTS only receives and issues commands of total strain for the strain extensometer, plastic strain control has to be governed by the correct total strain amplitude control. During the first loading cycle, the plastic strain is continuously calculated from the formula:

$$\varepsilon_p = \varepsilon_t - \varepsilon_e, \tag{4.4}$$

where ε_p is the plastic strain, ε_t the total strain and ε_e is the elastic strain calculated in the program as:

$$\varepsilon_e = \sigma / E, \tag{4.5}$$

where E is Young's modulus and σ the present stress level calculated from the load cell output divided by the cross-sectional area of the specimen. Once the calculated plastic strain reaches the desired level, loading is stopped and the total strain level is saved as the program command for the next cycle. By continuously comparing the command and feedback plastic strain calculated for each cycle, an adjustment is made and the tests are run under the control of the exact plastic strain wanted.

A function of automatic pause during the tests was added to the program, so that the replicas could be made. The operator can input through the terminal keyboard the time interval, i.e., the number of cycles, and the new frequency required during the next period. Another difference between CATM and CATMP is that all hysteresis loops in CATMP are displayed in one figure, so that the strain hardening and softening process can be clearly seen. The CATMP program is given in Appendix A.

4.3.3 Scanning Electron Microscopy

Compared to the optical microscope, a Scanning Electron Microscope (SEM) not only expands useful magnification to 10,000 X in routine instruments, but also increases the depth of focus to 1 μm at 10,000 X and 2 mm at 10 X, larger by more than two orders of magnitude than any optical microscope. The working principal of an SEM is briefly described as follows. An electron beam is emitted from a heated tungsten cathode, whose energy depends on the acceleration voltages, and focused by a system of magnetic lenses to a small diameter (approximately 10 nm). The beam reaches the specimen and scans it in much the same way as in a CRT used for image formation on a television screen. The magnification is changed by adjusting the current in the deflection coils. The electrons excited by the electron beam and emitted from the specimen surface are collected in an electron detector, then amplified by direct electron multiplication and conventional electron amplifiers before being sent it to the CRT. In addition to image displayed on a screen, a high-performance CRT is used to "write" the image with typically 1000 lines on a photographic film.

When the primary electron beam interacts with the specimen, electrons and other radiations are produced. Among all these electron modes, the secondary electron mode, backscattered electron mode, and the X-ray spectroscopy are used routinely with a high level of sophistication. The secondary electron mode, used in this investigation, provides information of surface topography, material contrast, and crystal orientation contrast.

The SEM employed was the Autoscan Scanning Electron Microscope manufactured by ETEC Corporation and situated in the Micromechanics Lab of McGill University. The major components of Autoscan SEM are:

1. the electron optical column including the electron gun, the condenser lens and the final condenser lens,
2. the specimen chamber,
3. the electron collection system,
4. the vacuum system,
5. the viewing CRT (cathode ray tube) and recording CRT (the camera), and
6. the control console.

All controls of the electronic system such as mode selection, accelerating voltages, magnification, the lens current, and focus, etc, are located on the control console board and can be adjusted. The acceleration voltage range is from 2.5 kv to 30 kv, magnification ranges from 10 X to 100,000 X, total emission current of the gun 0 to 300 microamps full scale.

4.3.4 Replication Technique

Replication of Specimen Surfaces

A replica is a reproduction of a surface to be studied. It is usually made by depositing a thin film of suitable material onto the specimen surface. This film copies the surface features and is subsequently removed. Major application areas of the replica technique are in Scanning Electron Microscopy (SEM), Transmission Electron Microscopy (TEM), and light microscopy. Replication techniques offer the unique capability of allowing a fracture surface, for example, to be studied when direct observation of the specimen is inconvenient. In this investigation it is particularly helpful, since it is otherwise impossible to follow the crack initiation/propagation process during a test.

Figure 4.6 illustrates the two major techniques in producing a replica. The two-stage method is mainly applicable to the analysis of service fractures where portability and integrity of the replicas are of paramount importance, while the single-stage replication process is applicable to laboratory investigations. There are three methods of producing single-stage replicas:

1. a plastic film can be applied or formed on the surface,
2. a film of carbon can be formed directly on the fracture surface by vacuum vapor deposition, and
3. a conversion oxide film can be formed on the fracture surface by chemical or chemical-plus-thermal treatment of the surface.

Both carbon and conversion oxide replicas are stronger and more accurate than plastic replicas. But the underlying metals of these two replicas have to be destroyed (dissolved by either chemical or electrochemical etching), which is intolerable for this research. Therefore the plastic single replica technique was used in the experiments.

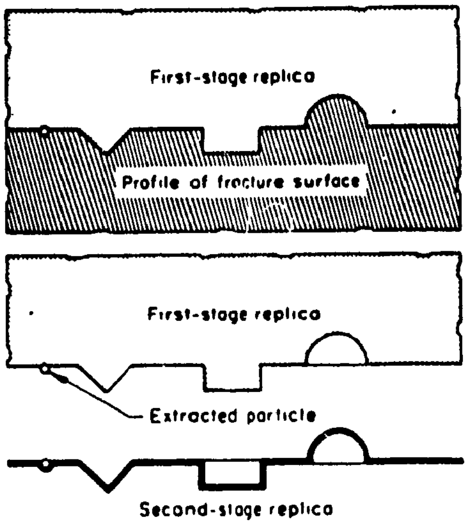

Figure 4.6: Single Stage and Two Stage Replication Technique.

The thickness of the replica needed depends on the roughness of the specimen. Usually, a rougher surface needs a thicker replica. Thin plastic replicas, from 0.1 to 0.15 μm, are mainly limited to polished and etched specimens since, normally, they cannot be stripped without chemical assistance from a rougher surface. The thickness of thick plastic replicas ranges from about 25 to 305 μm, corresponding to the commercially available range. Considering that the sensitivity of the replica is reduced as its thickness increases, it is important to find the right thickness when the replica must not only provide a detailed surface image, but also must not be torn when stripped off.

In the present case, the specimen surfaces are smooth (well polished), yet rough around the crack. Replicas with different thicknesses were tried, and the best were found to be 34 μm thick Bioden R.F.A. acetylcellulose replicating film supplied by

Oken-Shoji Co., Ltd., in Tokyo, Japan.

This plastic film has excellent film-formation properties: it easily dissolves in the solvent—methyl acetate, less air bubbles form under it during replica application, and yet it easily separates from the surface of the specimen. The resolving power of this replica is about 0.01 μm and the working temperature may be up to 100°C. Bioden R.F.A. is an SEM replica material; it is also excellent for observation through the optical microscope or with the naked eye. When the replica is viewed against the light, cracks can be easily located by the naked eye; this greatly helped the preparation of replicas for SEM viewing.

To prepare the plastic replica, a strip is cut from the plastic sheet, and one side softened by being soaked in solvent for a few seconds. The softened face of the strip is immediately placed on the specimen surface with the center touching first, then carefully rolled out to the two sides to prevent air bubbles. The half liquidized plastic film follows the contour of the surface in detail and forms a mirror image of the surface topograph which remains when the plastic dries. The time required for drying for this particular film is from 5 to 10 minutes. After the solvent is volatilized, the replica is carefully stripped off the specimen with tweezers.

Coating and Shadowing of Replicas

If the replica is only going to be observed by the naked eye, or under the optical microscope, it is now ready. However, if details of the replica are to be revealed under high magnification in a scanning electron microscope, an untreated plastic replica does not provide enough contrast to permit full realization of the features of the surface with maximum fidelity resolution. Furthermore, impingement of the electron beam causes an electrical charge to build up locally and intermittently. Therefore, the replica must be treated to possess sufficient electrical conductivity, at least on its surface, by applying a thin but continuous metallic film of good electrical conductivity.

When metal evaporation takes place in a high vacuum at 10^{-4} torr or higher, the vaporized metal atoms travel in straight lines from the evaporation source to the subject to be coated. If the replica surface is at a right angle to the evaporation lines, a uniform layer of the metal is deposited on the surface. This process is called "coating". If the replica surface has an angle of 15° to 45° to the lines, facets on the replica will receive different amount of vaporized metals depending on their tilt and orientation. This is called "shadowing". The principle of coating is further illustrated in Figure 4.7.

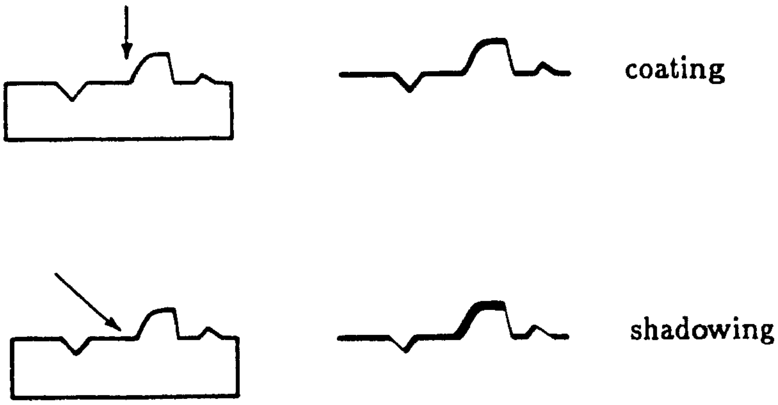

Figure 4.7: Coating and Shadowing of Replicas.

Coating and shadowing of the plastic replicas was performed in the Denton Vacuum DE-502 High Vacuum Evaporator. The purpose of coating the replicas with a thin layer (about 0.01 μm) of carbon is to provide support to the replica and enough conductivity to avoid charging. While evaporating the carbon rod, the platform holding the specimen mounts with replicas glued on them was tilted and rotated so that they could be uniformly coated.

After coating, replicas were shadowed to a thickness of 0.005 μm at 45° with a heavy metal alloy, gold-palladium. The main purpose of shadowing was to enhance the contrast by increasing secondary electron emission. Shadowing also provided information (within certain limits) about the depth of the crack. Once the shadowing angle is known, the depth of the crack can be estimated from the measured length of the shadow behind a hill in the replica.

4.4 Experimental Procedures

Specimen machining and preparing were as introduced in Section 4.2.3. To protect the material from cutting by the knife edge of the strain extensometer (otherwise the fatal crack always initiated under the knife edge), two drops of epoxy were deposited where the knives were to be attached. This was usually done in the evening before testing to allow complete drying. The extensometer was fastened tc the specimen with a pair of rubber bands.

The MTS machine warm up and the specimen mounting followed the operating procedures available in the Fracture Mechanics Lab. Since copper, especially annealed copper, was feared to be too soft to make the self-aligning grips swivel without the specimen being plastically deformed, the alignment of the grips was performed beforehand on a straight steel bar. The copper specimens were then mounted with the grips in rigid condition relative to the piston and the cross head. This way the specimens often were broken by cracks in the testing area and confidence was gained concerning the alignment of the test apparatus.

Tests were performed in air environment at room temperature with a humidity of 40 – 60%. Samples were under reversed tension-compression with stress amplitude ratio $R = -1$, and under constant plastic strain control through the program CATMP. The plastic strain levels were $\Delta\varepsilon/2 = 0.15\%$ at a frequency of 1.3Hz and $\Delta\varepsilon/2 = 0.05\%$ at a frequency of 11Hz, and the loading function had a triangular waveform.

To start the programme CATMP, the RT-11 Monitor on a PDP-11/04 had to be loaded first, following the procedures prescribed in MTS Software Manual; then the CATMP was loaded, following the procedures described in [99]. The program is interactive, and the operator has to answer the questions that appear on the terminal screen by typing and pressing "enter". The program was written in such a way that tests could be stopped at a load level slightly lower than maximum. This enabled replicas to be taken with a crack being almost fully open. When the replica was dry, the approximate position of the specimen was carefully marked at the corner of the replica with a felt pen so that the location of the crack could be recognized. Replicas peeled off the specimen were then stored in identifiable containers for later processing and evaluation.

Every time the tests stopped, new commands have to be put in to restart. The question appears on the left corner of the screen as "S7,R1,N5" followed by a blinking question mark. S7 is the number of cycles at which the operator wants the test to be stopped, R1 is the new frequency, and N5 is a function of the frequency. The relation of R1 and N5 is given in Table 4.2.

R1 (Hz)	N5	R1 (Hz)	N5	R1 (Hz)	N5
1-2	6	2-5	5	5-10	4
10-20	2	20-50	1	50-100	0

Table 4.2: N5 as a Function of Frequency R1.

In all experiments, except #1, the replication procedure continued until a crack developed large enough to cause a 10% load reduction. Specimen #1 was allowed to run further in order to reveal typical hysteresis loop changes. If the fatal or a main crack did not start on the part of the surface covered by replicas the test was discarded.

For successful tests, the locations of the fatal or main crack on the replicas were identified by marks made during tests with the help of observation by the naked eye. The portion of the replicas containing the crack were cut to a dimension of less than 1 cm^2 and carefully fixed at four corners by crazy glue on specimen mounts made for SEM observation. Coating and shadowing were performed as described earlier.

The operation of SEM had its polarity switch on the Video Amplifier Control Module as negative in order to convert the mirror image replica into a form more representative of the actual crack. For example, instead of seeing a white crack in positive polarity, the negative mode changed it back to black which is easier to interpret.

Starting from the replica containing the largest macrocrack that corresponded to the highest number of fatigue cycles and tracing the crack back towards the first replica corresponding to the lowest number of cycles, the Autoscan SEM followed the fatal (or main) crack back to its first discernible beginnings. The fatal crack initiation and early propagation history is thus recorded. Polaroid 55 instant photographs of each replicated macro-, micro- and sub-microcrack were taken by the camera installed in the SEM and catalogued for further analysis.

To further ensure the replication technique and to fulfill the ASTM E606 requirement of post-mortem examination, metallographic examination of successfully tested specimens was performed as the last step of the experiment. First the specimen surfaces were viewed to gain more information concerning the general surface features at failure, and then the specimens were pulled apart and the portions containing the fracture surfaces subjected to a fractographic surface analysis.

Chapter 5

RESULTS, ANALYSIS AND DISCUSSION

5.1 General Results from CATMP Controlled Fatigue Tests

5.1.1 Strain Hardening/Softening

The CATMP controlled testing results of specimen #1 (it is #3 in the Appendix) is presented in Appendix B which gives a general form of the program output. By superimposing all hysteresis loops, the strain softening or hardening of specimens is clearly visible. Among all the four specimens, specimen #1 is the only one that experienced strain softening, specimens #301 and #302 experienced strain hardening while specimen #2 did not really experience strain hardening or softening. Since specimen #1 is the only example for strain softening, it will be discussed. In the two examples for strain hardening, specimen #302 is much more typical than #301, therefore, the strain hardening of specimen #302 will also be discussed.

The strain softening process of specimen #1 is clearly visible from its hysteresis loop changes presented in Appendix B. Besides the hysteresis loops, its strain softening is also indicated by the maximum stress versus number of cycle curve in Appendix B. However, instead of a steady decrease, the maximum stress rose at the beginning before it started to decline. Although the maximum stress did not stop decreasing until the end of the test, it became quite stable after 500 cycles when it was considered to have entered the saturation stage.

Duplicated hysteresis loops indicating strain hardening of specimen #302 are given in Figure 5.1. The hardening rate was rapid at the first few cycles, the first cycle alone had a maximum stress increase of 2.5 MPa, and the total increase in the first eight cycles was more than 10 MPa. The hardening rate per cycle decreased as the cycles increased and the stress level became stable at about 1000 cycles, which was considered as the saturation state of that specimen.

In all specimens tested, the stress versus number of cycle curves revealed two characteristics.

1. <u>The tendency of the stress elevation before strain softening.</u> For strain softened materials, as shown in the stress versus cycle curve of specimen #1 in Appendix B, the maximum stress level increased at the beginning of test before strain softening started. For strain hardened material, such as the case of specimen #302, slight strain hardening occurred until about 2000 cycles when strain softening started to occur. In the stress versus cycle curves of all

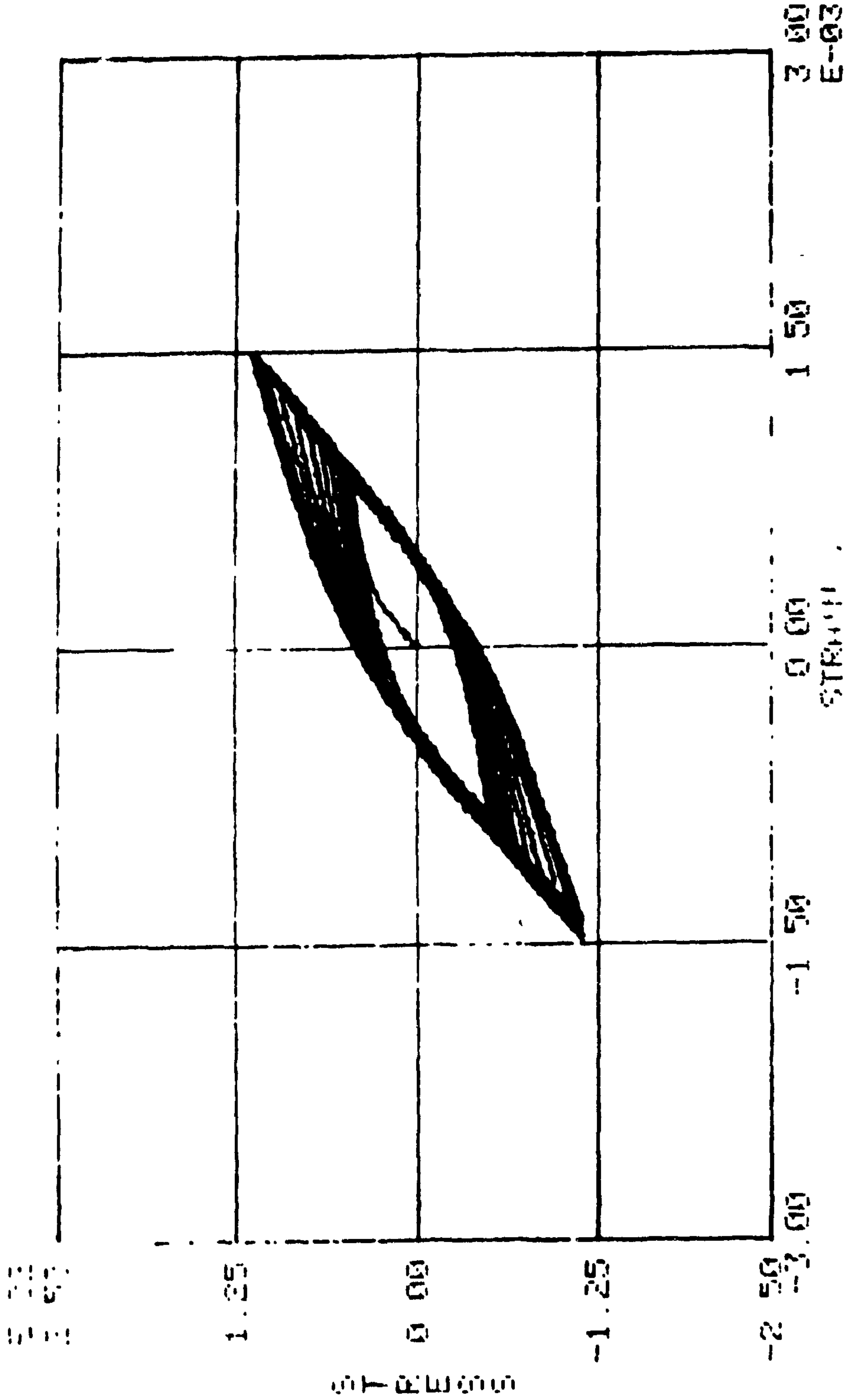

Figure 5.1: Strain Hardening Process of Specimen #302.

specimens, this mild peak was apparent.

The slight over-hardening in the strain hardening of annealed copper has also been observed by Kuokkla and Kettunen [29], who studied the strain hardening behaviour of annealed 99.98% purity OFHC copper polycrystals with both small grain sizes of 30μm and large sizes of 2 mm. They stated that this effect was too indefinite for further conclusions.

2. The tendency of maximum stress decline in the saturation stage. In all specimens tested, it was generally observed that the stress versus cycle curves were not at the same level in the saturation stage for both strain hardened and strain softened materials. The stress versus cycle curves showed a slight negative slope, as was also reported by Kuokkla and Kettunen, [29].

The decrease of maximum stress in the saturation stage is related to the fatal crack initiation and propagation. However, a quantitative analysis between the crack length and the applied stress level decrease cannot be carried out since, not only is a quantitative analysis of the microcrack distribution and growth unavailable, it is also hard to determine the exact transition from strain softening at the saturation state. As has been mentioned above in 1, strain hardening and softening processes are complicated by microstructure adjustment. Therefore, stress decrease can only be considered as a qualitative measure of crack initiation and propagation.

5.1.2 Hysteresis Loop Character Prior to Failure

As is seen from the hysteresis loops recorded after 10% load reduction, once the specimen entered this stage, the decrease of tensile stress became more pronounced and the specimen broke in less than two hundred cycles, which is about one percent of the total fatigue life. While the tensile stress decreased drastically, the maximum compression force was relatively stable. As a consequence, the "kick-in" close to the maximum compression load (often seen in fatigue literature) became more prominent. This can be explained from the closure point of view: on the compression cycle, the crack remains open until a certain compressive load level. After crack closure, the capability of the specimen to stand compressive stress is close to that of one without a crack. Therefore, only the part of hysteresis loop above the "kick-in" point is the true loop of the specimen with reduced cross section.

5.1.3 Metallurgical and Mechanical Material Properties of Specimens

The annealing conditions (time and temperature) have a subtle influence on the material properties. Based on CATMP outputs, the mechanical properties of the specimens including the monotonic (taken at the first loading cycle) and cyclic material properties (taken after saturation), and the metallurgical properties (the grain size of specimens associated with the annealing temperature) are summarized in Table 5.1. The annealing time is 25 minutes and is the same for all specimens.

As shown in Figure 5.2, for a minor alloy of copper and zinc [100], a transient region exists where the material's tensile and yield strength changes drastically as the annealing temperature changes with a fixed annealing time. Although the annealing curves of OFHC copper are not available, the principle applies. The annealing temperature for copper alloys suggested by the handbook is from 375° to 650° C. When some samples were annealed at 500° C for 30 minutes, they showed a yield strength

Spec. No.	Anneal. Temper. (°C)	0.2% Offset Yield Str. (MPa)		Modulus of Elasticity (GPa)		Approx. Grain Size (μm)
		Monot.	Cyclic	Monot.	Cyclic	
#1	400	236	194	143	126	20
#301	400	131	183	113	125	20
#2	400	180	186	127	125	20
#302	450	57	145	110	123	22

Table 5.1: Annealing Conditions and Mechanical Properties of Specimens.

of about 35 MPa, that did not significantly change as the annealing temperature and time increased. It seems that the transition takes place in between 375° and 500° C which covers the region chosen for this investigation.

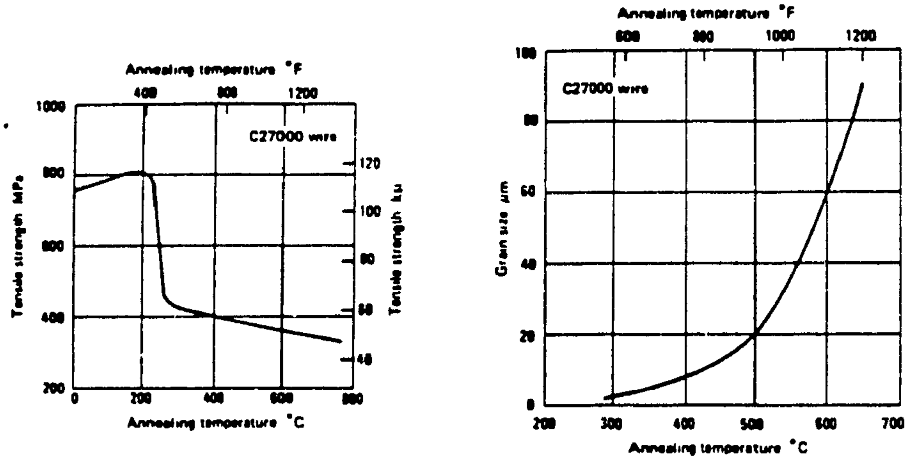

Figure 5.2: Material Response to Annealing Time and Temperature. *ref* 100

The monotonic 0.2% yield strength of the specimens had a big range, from 57 to 236 MPa. As a consequence of the strain hardening/softening, the cyclic yield strengths became closer, especially for specimens #1, #2, and #301 which were annealed at the same temperature and time, despite the large variation in plastic strain of specimens #1 and #2. Among these three specimens, #2 is distinguished by its similar monotonic and cyclic yield strengths. It is in a particular state in which it experiences neither strain hardening nor softening and, hence, its yield stress will be used as a reference in the later plastic strain intensity factor ΔK_p analysis. On the other hand, since the annealing conditions of specimen #302 are much closer to the lower end of the annealing curve in Figure 5.2, #302, it started with a much lower monotonic yield strength and ended with a lower cyclic yield strength than the other three specimens.

That the annealing temperature causes material property differences should be borne in mind, since this brought about big differences in fatigue life, crack initiation data and propagation information. This will be mentioned in later discussions of the results.

Another material property related to the transition of annealing time and temperature is on the metallurgical side, namely the grain size. Grain sizes were determined by estimation. Since the real specimen to be tested cannot be etched, etching was carried out on some of the dummy specimens to reveal the microstructural features of the material. The etchant was composed of

1. 100 ml distilled water,
2. 20 ml sulphuric acid (H_2SO_4), and
3. 2 g potassium dichromate ($K_2Cr_2O_7$),

which yielded a good grain contrast. Under optical microscopic examination, the etched samples annealed to different degrees revealed uneven grain sizes and a tendency for there to be long and narrow grains along the drawing direction of the bars. Based on this optical microscopic study, the grain size of the tested samples was estimated from examination of the specimen surfaces after the test. Although the grain boundaries were not always explicit, the slip lines in different grains gave a good indication of the grain boundaries from which the grain sizes could be averaged.

While recrystallization influences the mechanical properties of a material, further heating beyond the recrystallization temperature produces grain growth, as indicated in Figure 5.2 where the grain sizes start to show distinct change only after the transition temperature. Since the annealing conditions of all four specimens are within the transition region, their grain sizes are very similar, despite the fact that the yield strengths of the specimens are so different.

5.1.4 Cyclic Stress Strain Levels and Fatigue Lives

Basically, two plastic strain levels were involved in this investigation, 0.15% and 0.05%. However, due to the differences in the material properties, the cyclic stress-strain levels and fatigue lives varied. As listed in Table 5.2, the changes of stress and strain levels from monotonic to cyclic show the same features as the 0.2% offset yield strength change discussed in last Section. The three specimens annealed at 400° C had similar maximum applied stresses at two very different plastic strain amplitudes, implying that the two plastic strain amplitudes chosen are in the quasi-plateau of this material. The total strain amplitudes of specimens #1 and #301 (with the same plastic strain level of 0.15%) are also similar at the first cycle, the subsequent cyclic softening of #1 and cyclic hardening of #301 bringing them even closer together.

Under the same 0.05% plastic strain level as in specimen #2, specimen #302 exhibited a much smaller monotonic maximum stress and total strain due to the differences in annealing conditions; and even though the fatigue cycling again brought them closer together, the cyclic maximum stress and total strain of #302 was still much smaller than specimen #2.

The fatigue lives of specimen #1 and #301 are very similar. Having the same plastic strain amplitude, these two specimens had fatigue lives of 2×10^4, with #301 (slightly softer than #1) having a longer life. Similar fatigue lives of around 2×10^4 cycles were also recorded for several failed samples (where a crack did not start in the replica covered region) at a plastic strain amplitude of 0.15% with the same annealing conditions of 400° C for 25 minutes, indicating reliable experimental techniques, stable testing machine with good alignment, and repeatable specimen and testing conditions.

As proposed in Chapter 3, plastic strain is not the only factor that determined the fatigue life of specimens. This is proved here by specimen #302 which had a much longer life than #2 under the same plastic strain level. Following the definitions proposed in Chapter 3, specimens #1, #301 and #2 are therefore under the scope of low cycle fatigue while specimen #302 is alone under the scope of high cycle fatigue. In later discussions, specimen #1 will be often quoted as the representative of the three specimens.

Comparing the percentages of cycles to the completion of strain hardening/softening to their total fatigue lives, the ratio was less than 2.5% for all specimens, there being a tendency for the ratio to decrease as the ductility of the material increased. The softest specimen, #302, attained a stable loop after only 0.4% of its total fatigue life.

Specimen Number	$\Delta\varepsilon_p/2$ (%)	Stress Amplitude $\Delta\sigma/2$ (MPa)		Total Strain Ampl. $\Delta\varepsilon_t/2$(%)		Fatigue life (cycles)
		Monot.	Cyclic	Monot.	Cyclic	
#1	0.15	230	186	3.48	3.12	1.98×10^4
#301	0.15	128	178	2.57	2.99	2.13×10^4
#2	0.05	161	166	1.82	1.79	1.22×10^5
#302	0.05	46	112	0.92	1.37	2.58×10^5

Table 5.2: Stress Strain Amplitudes and Fatigue Life of Specimens.

5.2 Analysis of Results and Testing of the Mechanical Model

5.2.1 Relation of Crack Lengths to the Number of Cycles

The first step in the analysis is to measure surface crack lengths. The carbon coated and gold-palladium shadowed replicas provided clear images of cracks even at small crack lengths, thus making an accurate measurement of crack lengths possible. However, the rules for determining the lengths of cracks need to be well defined, since any obscure or inconsistent interpretations of crack length could give erroneous results. Problems in defining this measurement may well be one of the major reasons for the scatter exhibited by fatigue crack or short crack propagation studies. In this investigation, the crack lengths are measured from photographs of replicas following the rules:

1. the projected lengths on the plane perpendicular to the applied load are measured,
2. no matter how long the crack spreads, only the already coalesced part of the crack is considered, and
3. at the beginning, when several sub-microcracks or microcracks exist at the crack site, the length of the longest of them is taken as the crack length.

The focus of the replica study was to trace a fatal or a main crack back to its origin, while at times observing the specimen surface. Starting from the last step, the crack was traced back to the smallest crack lengths of less than 1 μm measurable from the replicas. The half surface crack length thus obtained versus number of cycles are plotted in Figure 5.3.

The cracks recorded in specimen #1 and #2 are the fatal cracks that led to final failure of the specimen and, in #301 and #302, are main cracks which did not proceed to fast propagation. The different nature of these two kinds of cracks is reflected in the Figure: the two curves of fatal cracks show sharp crack length increases and a curvature change at the end of tests, while the propagation of the two main cracks stopped when the fatal cracks in these two samples progressed to cause a 10% load reduction, i.e., before the curvature change could have taken place. The curvature change of the fatal cracks is the most prominent feature reflected in this Figure.

Since at this scale, the crack lengths in the initiation stage are not displayed, due to the extended range of the crack lengths, crack length versus cycle curves were transformed into a log scale, as presented in Figure 5.4. Several characteristics of crack lengths can be summarized from this Figure. These are:

1. in the curves of specimens #1 and #2, an approximate division of three regions of crack life, i.e., the two sub-regions in the crack initiation region, I_p, namely, I_i and I_{ii}, and the crack propagation region, II, is revealed, and

2. since replicas of specimens #301 and #302 were taken more frequently than they were in specimens #1 and #2, in the former case, crack lengths stayed at one level for a considerable number of cycles, showing the crack nucleation process described in Chapter 3.

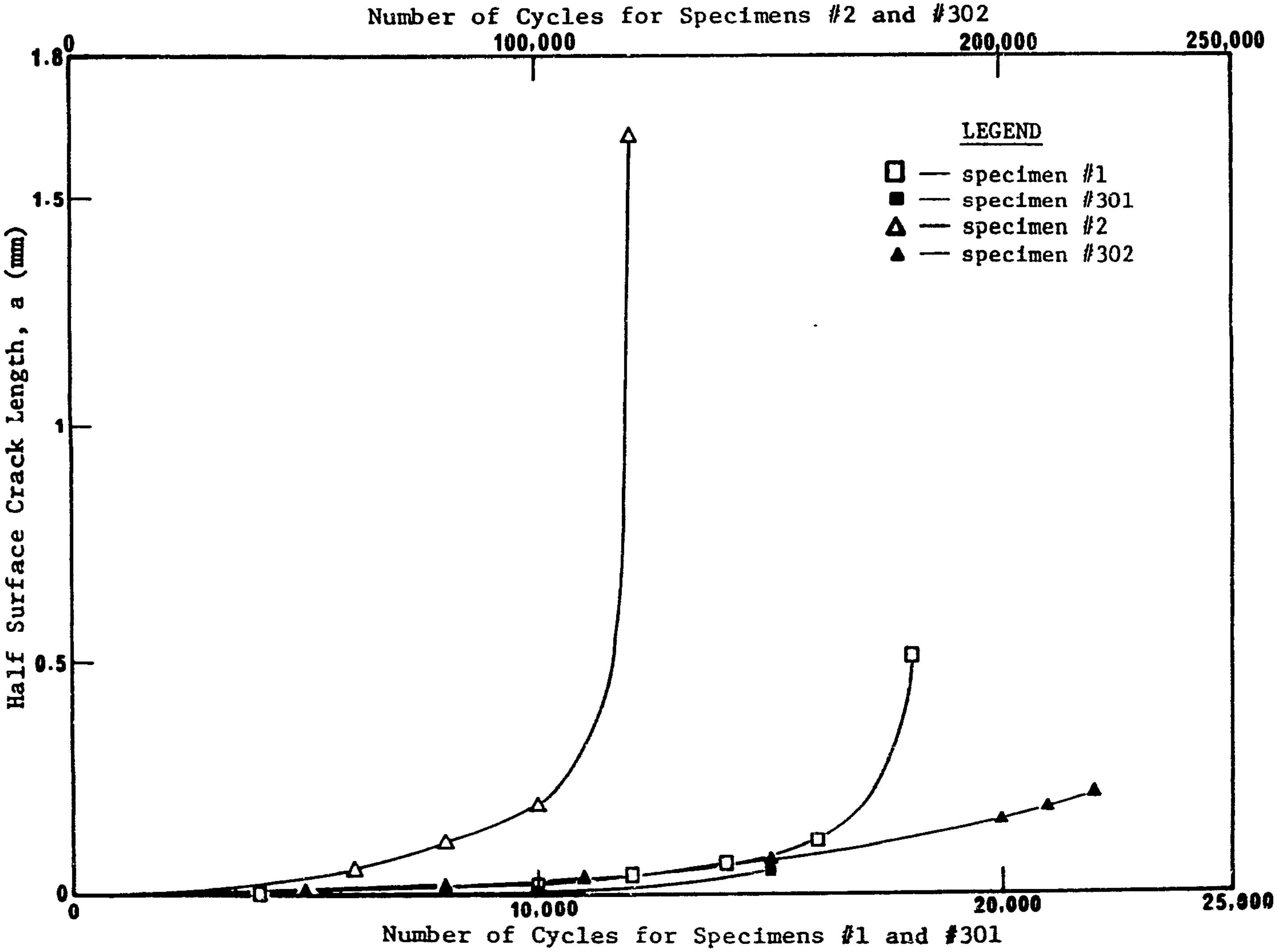

Figure 5.3: Half Surface Crack Lengths as a Function of the Number of Cycles. (Semi-log scale)

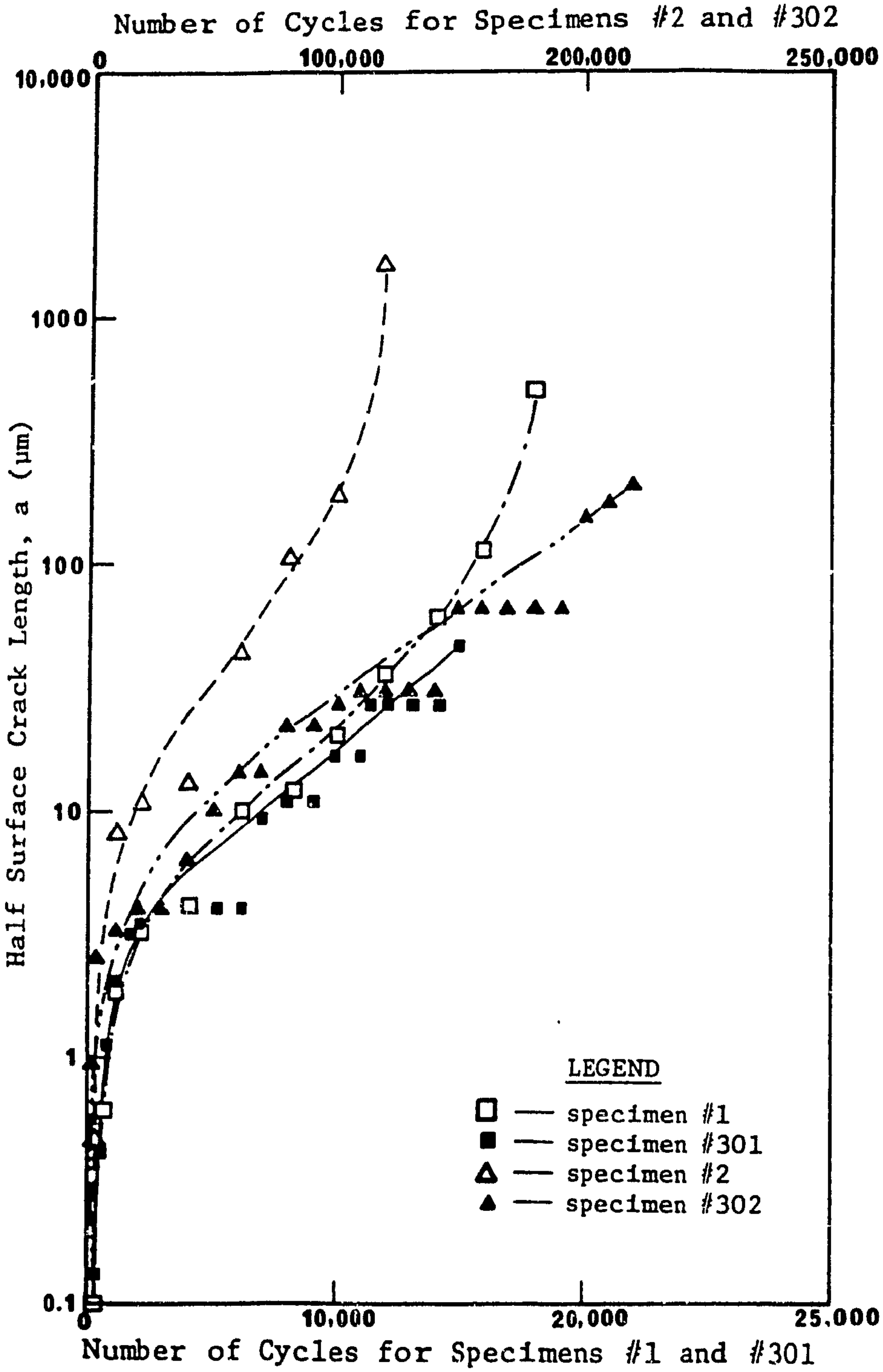

Figure 5.4: Half Surface Crack Lengths (log-log scale) as a Function of the Number of Cycles.

5.2.2 Stress Intensity Factor ΔK Analysis

Although the crack length versus cycle curves in Figure 5.4 reveal some qualitative characteristics of crack initiation, there were not enough to deduce any quantitative relations of crack initiation and early propagation. After the crack growth rates were calculated as the half surface crack length increase divided by the number of cycles, the investigation of the driving forces for crack initiation and early propagation may commence.

The expression of ΔK was derived for semi-elliptical surface cracks in infinite bodies by numerical methods in [97,101] as:

$$\begin{aligned} \Delta K &= Q\,\sigma\,\sqrt{a} \\ &= \kappa\,(2/\sqrt{\pi})\,\sigma\,\sqrt{a}, \end{aligned} \tag{5.1}$$

where Q — geometry factor,

a — half surface length,

σ — remote stress level,

and κ — a stress concentration factor along the crack periphery.

The factor κ varies along the crack periphery for a fixed aspect ratio λ and takes different forms as λ changes. Determination of κ is a major subject in the study of semi-elliptical surface cracks. Through different numerical methods, κ has been given different forms for the same λ value.

Figure 5.5 is duplicated from [101] to illustrate different evaluations of κ for a semicircular surface crack (when $\lambda = 1$). It increases from 1.025 at the deepest point of the crack to a maximum of 1.25 near the corner point where the periphery of the surface crack intersects the free surface of the body containing the crack, and decreases to zero as the corner point is approached.

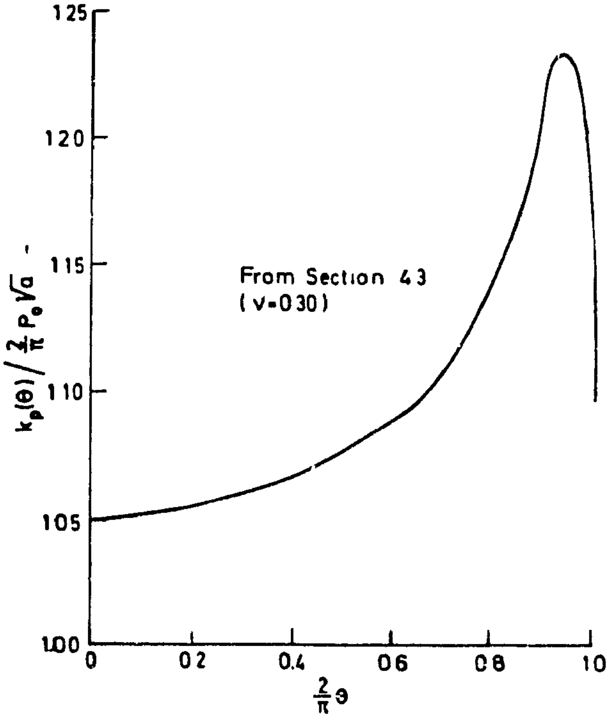

Figure 5.5: Stress Intensity Factor along the Crack Periphery of a Semicircular Crack. *ref* 101

In the calculation of ΔK, the crack is assumed to have a half penny shape. An average of κ was taken as 1.2, close to the maximum value of 1.25. The crack growth rates were then correlated with the conventional stress intensity factor ΔK, calculated in this manner, and the results are shown in Figure 5.6.

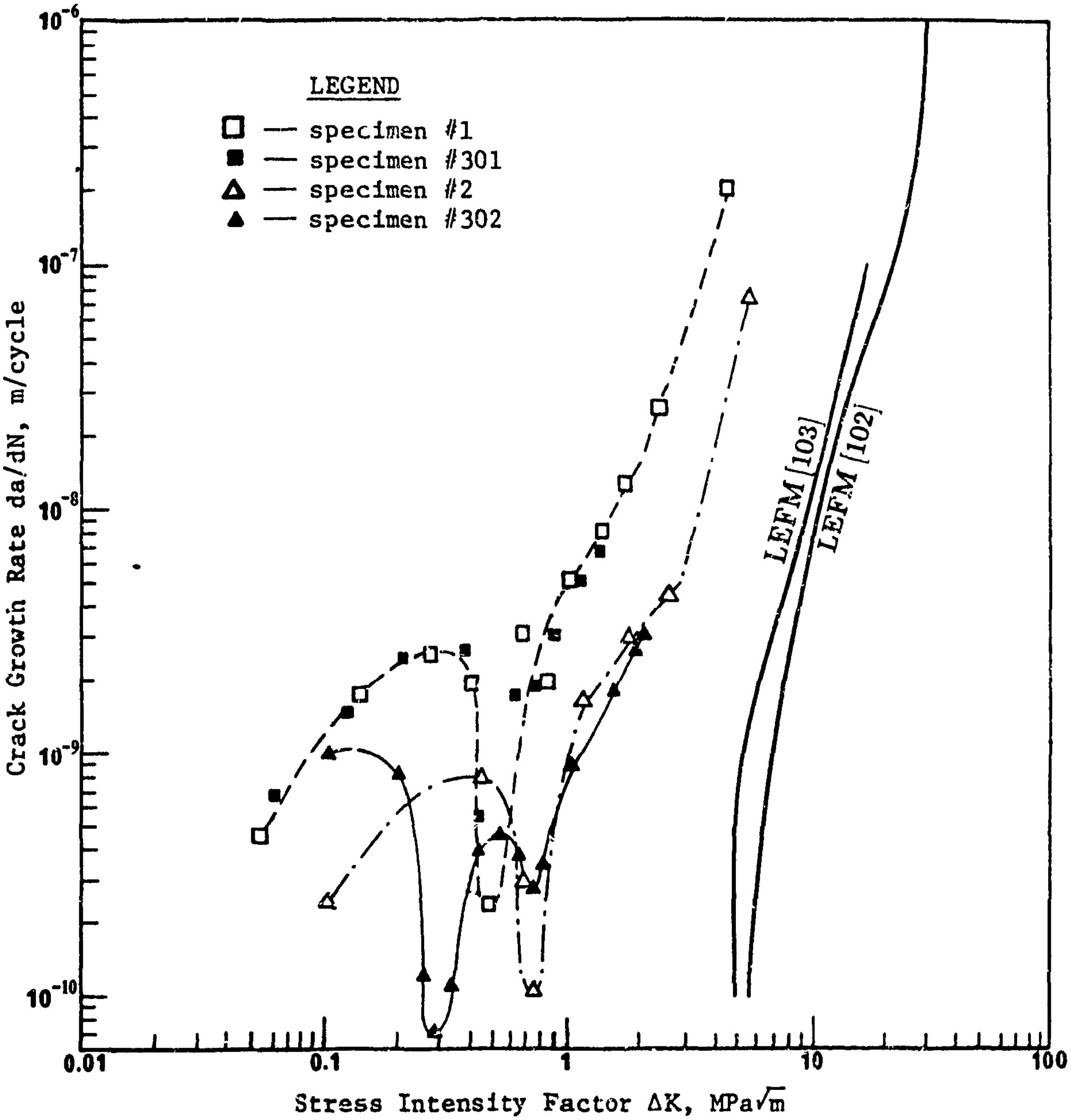

Figure 5.6: Crack Growth Rate versus the Stress Intensity Range ΔK.

For comparison, two long crack growth curves of copper are also included in the Figure. One is from the work of Usami [102], who studied the crack propagation of several materials including a 99.97% pure copper, annealed to a 25 MPa, 0.2 % proof stress (softer than the material of the present investigation) with a stress ratio $R = 0$ at room temperature; and another is from an associate work of Pandher [103], who determined the crack propagation threshold of 99.9 % pure commercial copper following the ASTM standard E 647 instructions for constant load fatigue crack growth tests at $R = 0.1$ and at room temperature. In both of them, values for ΔK_{th} was obtained by successively decreasing the load by steps until the crack growth rate was lower than 2×10^{-9} and 1.3×10^{-7} mm/cycle, respectively.

The data of crack growth rates from specimens #1 and #301 are similar enough to be correlated into one curve while the other two specimens have their own curves. In general, all curves in Figure 5.6 have certain things in common:

1. the hill and valley at the beginning of the curves, which typify the sub-microcrack nucleation mechanisms and the sub-thresholds discussed in Chapter 3,
2. a turning point, the LEFM crack propagation threshold in conventional stress intensity form, ΔK_{zth}, which divides the curves into the crack initiation regions and propagation regions, and
3. two steady growth periods, one after the sub-threshold and before the LEFM propagation threshold, ΔK_{zth}, and another after ΔK_{zth}.

In the initiation region, the three specimens in low cycle fatigue regime, #1, #301 and #2, started with a moderate crack growth rate during the sub-microcrack initiation. The sub-microcracks quickly enlarged themselves to form microcracks, reflected as hills in the Figure. At the microcrack formation, the growth rates were reduced and the cracks reached the sub-thresholds which are the valleys in the curves.

Although all curves have valleys as a common feature, specimen #302, the high cycle fatigue example is distinguished from the others. It not only started with a higher growth rate but also experienced two sub-thresholds before it gained the steady growth rate in the initiation region. However, the steady growth period after the sub-threshold is clear in all four specimens before the cracks reached their turning point.

After the turning point, while the main cracks in specimens #301 and #302 essentially stopped growing, the crack growth rates of the two fatal cracks in specimens #1 and #2 shifted to another line with a much steeper slope. Although there were not enough data from specimen #2, the fatal crack in specimen #1 indeed showed a much more normal growth behaviour.

Despite the trends shown individually by each curve, their combination is not entirely satisfactory. In fact, the data are rather discrete under the control of the LEFM parameter ΔK as indicated in Figure 5.6. The curves are not only far removed from the conventional long crack curves but also very far from each other, it is impossible to find a common expression in any region. Therefore, the conclusion is that the conventional stress intensity factor ΔK is not a suitable driving force in crack initiation and early propagation studies for materials within the transition region of high and low cycle fatigue.

5.2.3 ΔJ-Integral Analysis and the Plastic Crack Propagation Threshold

Considering that the present study involves both low and high cycle fatigue, the ΔJ-integral, the driving force in EPFM fracture, is naturally considered to be more appropriate. At the present time, a rigorous J-integral solution for the exponential-hardening plastic case is not available, and quantitative expressions of the J-integral have been estimated by various numerical methods under different considerations. Mowbray [104] derived an expression for an edge crack in an infinite body as:

$$\Delta J = 7.88\, \Delta W_{\infty}\, a\,, \tag{5.2}$$

where a is the crack depth and ΔW_{∞} is the total strain energy density at infinity obtainable from the shaded area under the cyclic hysteresis loop, as shown in Figure 5.7; whereas Dowling [92] derived an expression based on the elastic strain energy ΔW_e and the plastic strain energy ΔW_p for a small semi-circular surface crack in an infinite body given by:

$$\Delta J \simeq 3.2\, \Delta W_e\, a + 5.0\, \Delta W_p\, a\,, \tag{5.3}$$

where a equals half the surface crack length and ΔW_e and ΔW_p are the elastic and plastic energies respectively, as illustrated in Figure 5.8. His derivation of this formula is given in Appendix C.

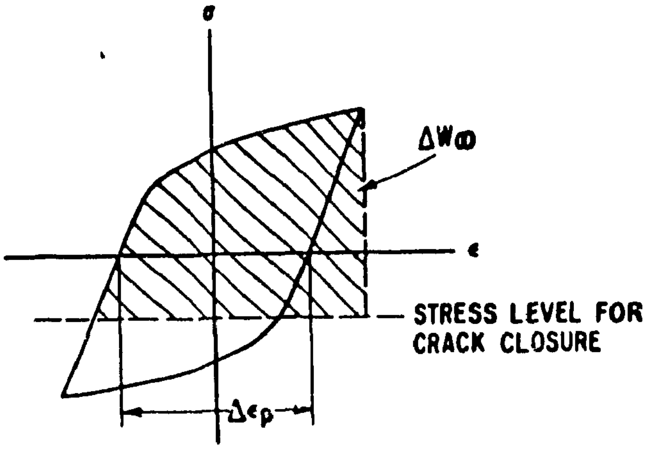

Figure 5.7: Total Strain Energy ΔW_∞ in Calculating ΔJ.

Although Eqn (5.2) could have been changed to a form corresponding to the semi-circular surface crack configuration and employed in the present analysis, Eqn (5.3) is favoured not only because the assumptions made during its deduction are more reasonable, but also because the plastic energy plays a bigger role than the elastic energy in the formula, this being more appropriate than the total energy method.

A problem remains in the application of Eqn (5.3) which concerns the strain hardening exponent, n. In Reference [104] the derivation of the elastic energy contribution to the ΔJ value was not affected by n. However, the determination of coefficient 5 in the plastic part was based on a cyclic strain-hardening exponent, $n = 0.165$.

The cyclic strain hardening exponent of the specimens in this investigation is not available, and although a hardening exponent, $n = 0.187$, for annealed OFHC copper was obtained in a previous laboratory investigation [105], the original hard

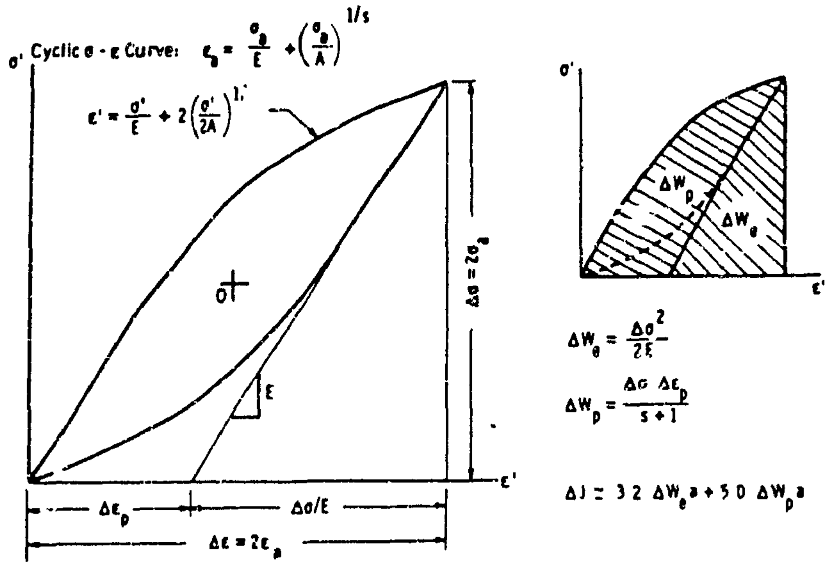

Figure 5.8: Estimation of Small Crack ΔJ from Stress-Strain Hysteresis Loops.

drawn and annealing conditions of this material are different from those reported. In addition, a strain hardening coefficient that fitted the hysteresis loops of specimens in this investigation is around 0.144 (with the exception of the softest specimen #302).

Nonetheless, as claimed by Dowling in the deduction of Eqn (5.3), errors in several areas were introduced in deriving cyclic J. One error concerns the strain-hardening exponent. In his deduction, it was assumed that the saturated hysteresis loops had the same strain hardening exponent as the cyclic one; hence the hysteresis loop in Figure 5.8 could have the expression of:

$$\varepsilon' = \frac{\sigma'}{E} + 2\,(\frac{\sigma'}{2A})^{1/s}, \tag{5.4}$$

where s is the conventional strain hardening exponent and A the conventional strength coefficient. But in reality, the two exponents do not match (refer to Figure 10 in Appendix C). As suggested by Dowling, Eqn (5.3) can be regarded as a rough estimate only. Since no better ΔJ solution is available at present, Eqn (5.3) was used in this investigation.

Determinations of the elastic and plastic strain energies were done mainly by measuring the area under the hysteresis loops and checking by the formulas given in Figure 5.8. The calculated ΔJ values were changed to $\sqrt{\Delta J \cdot E}$ in order to make it comparable with an equivalent unit of the stress intensity factor, ΔK.

Crack growth rate versus $\sqrt{\Delta J \cdot E}$ curves are shown in Figure 5.9. Despite the possible errors introduced in the derivation of Eqn (5.3) and also in the energy evaluation process, crack growth data versus $\sqrt{\Delta J \cdot E}$, on the whole, are better under ΔJ integral control, while the individual features of curves remain the same as under the ΔK parameter.

Even though the curves do not overlap, they are now gathered around the long crack curve and start to show some common characteristics. For example, the turning point from initiation to propagation of all specimens are pretty well at one $\sqrt{\Delta J \cdot E}$ level, which is the energy crack propagation threshold, $\sqrt{\Delta J \cdot E}_{pth}$. Therefore, $\sqrt{\Delta J \cdot E}_{pth}$ is indeed a material property, as proposed in the mechanical model. For the material investigated, $\sqrt{\Delta J \cdot E}_{pth}$ is determined from the Figure as 7.3 MPa$\sqrt{m}$ (compared to the crack propagation threshold obtained for a long crack of 4.9 MPa$\sqrt{m}$ [103]). This value is used to calculate the initial engineering crack size, a_0, in the following ΔK_p analysis.

Although they are not be as important as the plastic propagation thresholds in the mechanical model, the valleys of three low cycle fatigued specimen curves are also at one $\sqrt{\Delta J \cdot E}$ level, which is the sub-threshold, $\sqrt{\Delta J \cdot E}_{sth}$, proposed in Chapter 3. For this material, it is determined as 1.8 MPa$\sqrt{m}$. It is not as easy to include the two sub-thresholds of specimen #302 with the others, not only because it is under high cycle fatigue, but also because the crack recorded is a main crack not a fatal crack. In the sense that a sub-threshold can, however, be taken as an average of its two sub-thresholds, #302 can be included with the other three samples. Further investigation is necessary concerning the sub-threshold(s) of high cycle fatigued specimens.

The analysis of present results does not really match the ΔJ analysis of crack propagation results on smooth cyclindrical A 533B steel specimens by Dowling [92]. In his work, no such critical values as the energy crack propagation threshold $\sqrt{\Delta J \cdot E}_{pth}$ were found. Instead, all data fell in the big scatter band of the propagation line of CT or CCT specimens. Of course, the material and testing conditions in his investigation were different from the present ones, as well as in the experimental technique adopted. The plastic strain in Dowling's tests was not controlled by an strain extensometer in the testing section but were evaluated by the deflection of two threaded ends of the specimens; the replica thickness employed was 127 mm and no special treatment (such as coating and shadowing) was performed on the replicas. As stated in his paper, some of the replicas were checked with a low-power (X 20) optical microscope and the smallest crack lengths determined as "a few thousandths of an inch". Besides the questionable reliability of optical or naked eye measurement of crack lengths, for the strain ranges he tested (a total strain $\Delta\varepsilon/2$ from 0.25% to 2% with the longest fatigue life of less than 30,000 cycles), the smallest cracks he detected may well have passed the initiation region. From Figure 5.9, it is seen that

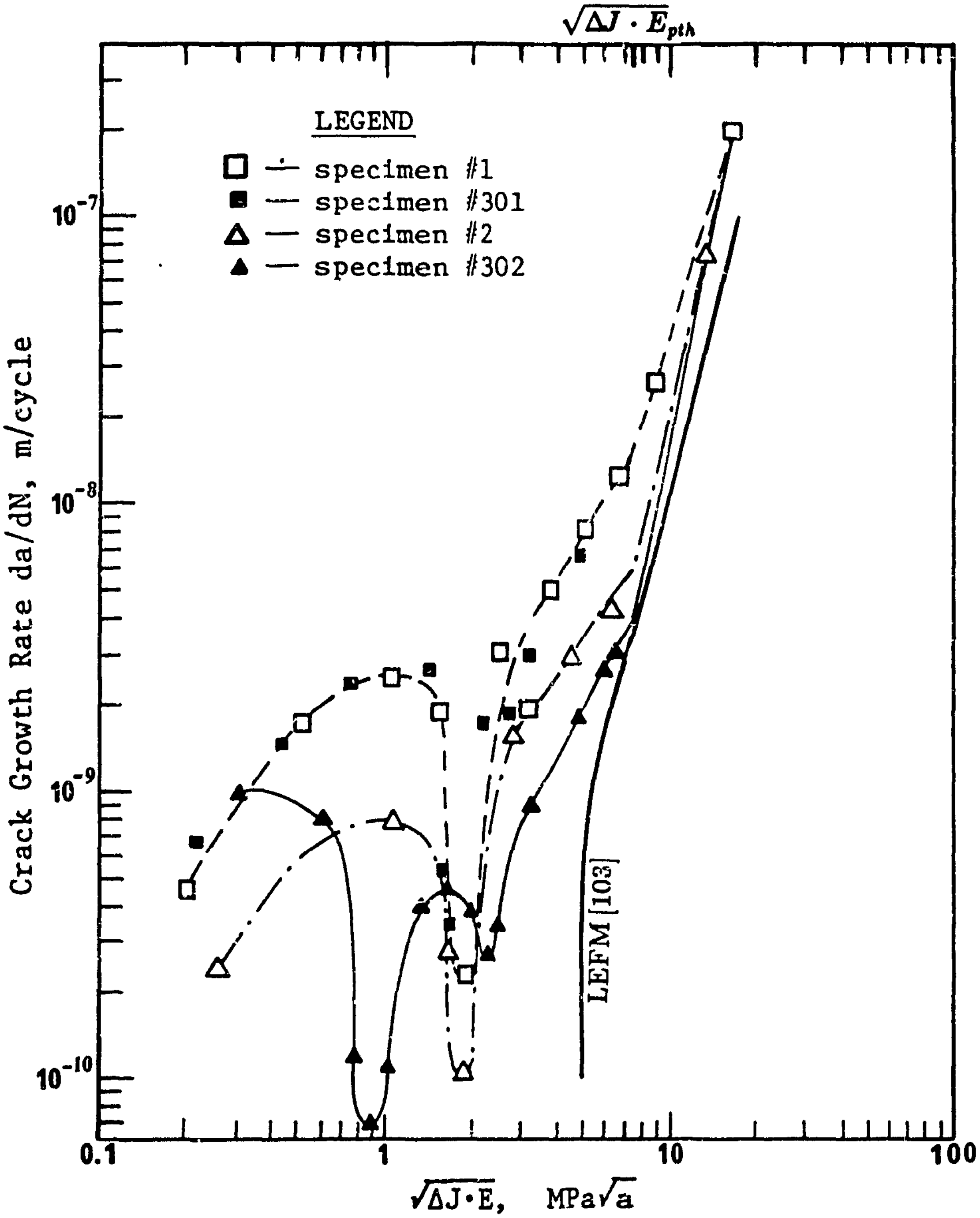

Figure 5.9: Crack Growth Rate versus $(\Delta J \cdot E)^{1/2}$.

the crack propagation data do come closer to the long crack curve after the plastic propagation threshold.

5.2.4 Plastic Strain Intensity Factor, ΔK_p, and the Proposed Model

What is presently lacking in fatigue analyses is a reliable quantitative estimation of fatigue life, both for initiation and propagation. Under ΔJ control, it seems impossible to accomplish this since no part of the curves can be expressed in one form. The new model based on the plastic strain intensity factor proposed in Chapter 3 is now applied to the crack initiation and early propagation analysis.

The plastic strain intensity factor is a new parameter, many considerations, such as the environment, temperature, etc., will interfere with the testing of the basic principle. However, the influence of material strength has to be included, since the annealing conditions led to different strengths of the specimens. Therefore, the function $\mathcal{F}(y,t,r,e,c)$ in Eqn (3.1) is limited to a function of the material strength in the present case. As mentioned in Section 5.1.4, specimen #2 was in an unusual heat treatment state in which its monotonic and cyclic yield strengths were the same. Taking this yield strength as the *standard cyclic* yield strength σ_{y_o} and comparing the yield strengths of all the other specimens with it, it was found that the influence of the hardness of material can be included through the following coefficient:

$$\mathcal{F}(y) = \left(\frac{\sigma_y}{\sigma_{y_o}}\right)^2, \tag{5.5}$$

where σ_y is the *current* cyclic yield strength of the specimen in consideration and σ_{y_o} the *standard cyclic* yield strength of this material.

Substituting $\mathcal{F}(y)$ of Eqn (5.5) to $\mathcal{F}(y,t,r,e,c)$ in Eqn (3.1), the plastic stress intensity factor now becomes:

$$\Delta K_p = \mathcal{F}(y)\ Q\ (2\Delta\varepsilon_p\ E)\sqrt{a}, \tag{5.6}$$

where $\mathcal{F}(y)$ takes the form in Eqn (5.5), Q takes the form in Eqn (5.1) with $\kappa = 1.2$, and the rest are as defined in Eqn (3.1). The crack propagation rates correlated by the plastic strain intensity factor ΔK_p are presented in Figure 5.10. Compared to ΔJ analysis, the plastic crack propagation threshold, ΔK_{pth}, of the curves are separated, so are the Region *II* crack propagation parts of the curves. However, the Region I_p parts, the crack initiation and Stage I propagation parts of the curves now look more promising. Despite the abnormal behaviours before and at the sub-thresholds, the Stage I microcrack propagation rates after the sub-threshold form a straight line with the expression of Eqn (3.2) proposed in the model. Values of the constants A and α are calculated as 6.92×10^{-10} and 1.377 respectively. Hence, the crack growth rate in the initiation and early propagation region is related to the plastic strain intensity factor by:

$$da/dN = 6.92 \times 10^{-10}(\Delta K_p)^{1\ 377}. \tag{5.7}$$

The seemingly big scatter in the early initiation region, with hills and valleys removed from the straight line, are worthy of further discussion. Besides all the violations of macroscopic engineering mechanics mentioned in the short crack section of Chapter 2, the fact that the crack lengths were only measured from the surface is also one factor in causing this phenomenon. While the hills represent a fast surface crack length increase, they do not necessarily represent an equally fast crack depth increase. As proposed in the mechanism models, the growth rate retardation at the sub-threshold occurred when the crack was developing mainly towards the inside of the material. If the real crack depth could be monitored, the data might not be so scattered. Unfortunately, there is not as yet an experimental method to measure the surface crack depth at such a small scale without destroying the specimen surface.

Nevertheless, this scatter is acceptable, since the steady growth parts in the initiation region indeed fell onto the line for every single specimen and a rough average of the hills and valleys on both sides of the line indicate a similar correlation. Therefore, the macroscopic driving force ΔK_p can indeed be used to monitor the Stage I sub-microcrack and microcrack nucleation behaviour in the initiation region, it can accurately monitor the Stage I microcrack propagation after the sub-threshold.

As a test of the proposed model, total crack initiation lives of specimens from a zero crack length to the initial engineering crack size a_0 are integrated. However, further work has to be done on Eqn (3.4) before it can be applied in this analysis. The main problem in completing Eqn (3.4) is in the geometry factor Q. Strictly speaking, Q is a function of the crack length and shape. An expression of Q as a function of crack length a in cyclindrical specimens is not available. Besides, within the crack initiation region where the crack length is small, the error caused by assuming Q as a constant should be very limited. Q is therefore simplified as a constant taking the form in Eqn (5.1) with $\kappa = 1.2$. The integration in Eqn (3.4) is thereby continued

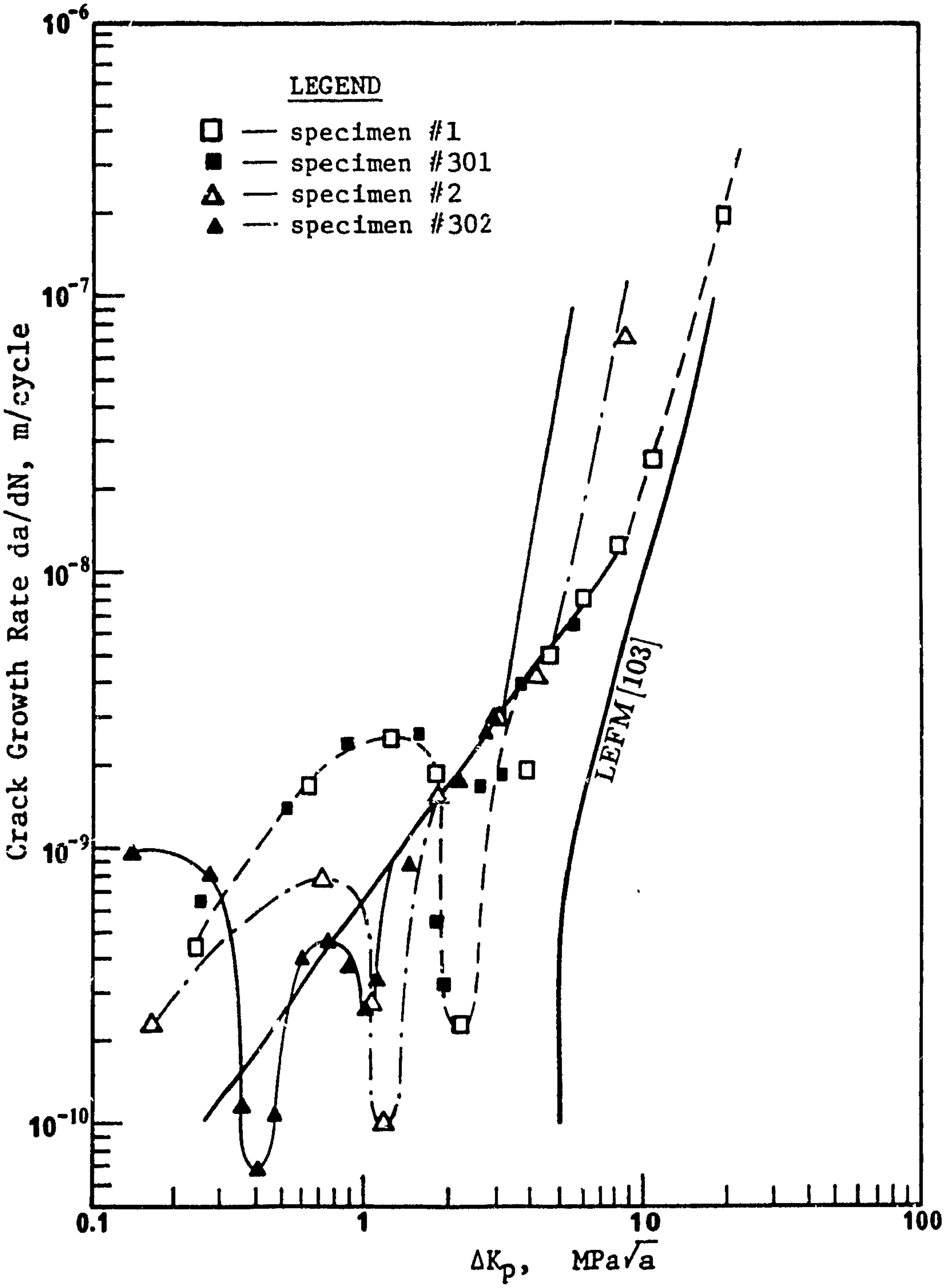

Figure 5.10: Crack Growth Rate versus Plastic Strain Intensity Factor ΔK_p.

as:

$$\begin{aligned} N_i &= C\,Q^{-\alpha} \int_0^{a_0} a^{-\alpha/2} da \\ &= C\,Q^{-\alpha} \frac{1}{-\alpha/2-1}\, a_0^{(-\alpha/2-1)} \\ &= C_1\, a_0^{(-\alpha/2-1)}, \end{aligned} \tag{5.8}$$

where $\alpha = 1.377$, C_1 is a product of all other constants, and a_0 is the initial engineering crack size. After a_0 was calculated at the $\sqrt{\Delta J \cdot E_{pth}}$ value of 7.3 MPa$\sqrt{m}$ for each specimen, the total crack initiation lives of specimens from a zero crack length to a_0 were integrated utilizing Eqn (5.8) where C_1 had been calculated for each specimen individually.

It should be pointed out that Eqn (5.8) not only can be used to predict the total crack initiation life of specimens at the plastic crack propagation threshold, but also may be extended to predict crack initiation life of specimens with ΔK_p values within the initiation region. For example, in the region from the sub-thresholds to the plastic crack propagation thresholds, the lives of the three specimens in the low cycle fatigue regime can be predicted from Eqn (5.8) by changing a_0 to the corresponding crack size. The specimen in high cycle regime, #302, is an exception. Noticing that the crack recorded in this specimen is only a main crack, it cannot be concluded that having two or more sub-thresholds is general for fatal cracks in high cycle fatigue.

The initial engineering crack sizes a_0 at crack initiation and the integrated and experimental crack initiation lives of specimens are listed in Table 5.3. As is seen from the Table, the initial engineering crack sizes at the plastic crack propagation threshold range from 59 to 247 μm for the plastic strains and material strengths investigated. The integration of crack initiation lives following the proposed model is accurate, the disparity between the predicted and measured initiation lives of all specimens being below 5%.

Before any discussion of the calculation of Region *II* crack propagation lives, the fact that the cracks monitored in specimens #301 and #302 were not fatal cracks but main cracks has to be considered again. For the purpose of crack initiation studies, main cracks are acceptable, because the difference in growth rates between main and fatal cracks does not become apparent until close to the plastic crack propagation threshold, as illustrated in Figure 5.4. But, after the fatal crack passes the plastic crack propagation threshold, its speed increases to such a rate that the non-fatal cracks become essentially dormant. Naturally, the crack propagation data in Region *II* for these two specimens are unattainable.

Although of no prime importance, different curves for Region *II* propagation were derived for all the specimens in order to estimate their propagation lives. Except for specimen #1 which had sufficient data for constructing its Region *II* propagation line, the propagation lines of other specimen in Figure 5.10 were constructed in such a way that the integration of the crack propagation life from Eqn (5.9) meets the real experimental crack propagation life.

Eqn (5.9) is a continuation of Eqn (3.5). In the derivation of Eqn (5.9), Q is again a problem as in the derivation of Eqn (5.8). Due to the larger crack sizes in Region *II* propagation, the error introduces by assuming Q as a constant is bigger. However, since there are no other choices in choosing another expression of Q and only a rough prediction of Region *II* fatigue lives are planned, the integration in Eqn (3.5) is continued with a great simplification of Q being a constant:

$$\begin{aligned} N_p &= D\,Q^{-\gamma} \int_{a_0}^{a_N} a^{-\gamma/2} da \qquad (5.9) \\ &= D\,Q^{-\gamma} \frac{1}{-\gamma/2-1} \left(a_N^{(-\gamma/2-1)} - a_0^{(-\gamma/2-1)}\right) \\ &= D_1 \left(a_N^{(-\gamma/2-1)} - a_0^{(-\gamma/2-1)}\right), \end{aligned}$$

where a_0 is the initial engineering crack size, a_N is the critical crack size at the transition from Region *II* to Region *III* crack propagation, γ and D_1 are different constants for each specimen. For the material and stress-strain range investigated, γ ranges from 3.34 to 6.00.

Similar to the determination of a_0, the critical crack size a_N in Eqn (5.9) was obtained at a constant $\sqrt{\Delta J \cdot E}$ value of 22 MPa$\sqrt{m}$. This number coincides with the conventional LEFM analysis, where the transition from Region *II* to Region *III* propagation in copper determined through CT tests did occur at a stress intensity factor ΔK value around 22 MPa$\sqrt{m}$ [9,103]. Besides that, it was found that whether this value is the true transition does not really matter in the prediction of crack propagation lives, at least within the strain ranges involved in this presentation. During the integration of Eqn (5.9), it was found that the term $a_N^{(\gamma/2-1)}$ is much smaller than the term $a_0^{(\gamma/2-1)}$. Changing a_1 from 0.538 mm to 5 mm would only cause 120 cycles difference in the total fatigue life for specimen #1 which is less than 0.7% of its total life, and the errors introduced by changing a_1 to 5 mm in other three specimens are all within 1.3% of their lives.

According to this investigation, the Region II crack growth remains an unresolved problem. No matter under what parameter control, even under the ΔJ analysis where the Region II cracks of the specimens were closest, not one common slope was detected. As is seen from Figure 5.10, the crack propagation lines constructed in the above way for the four specimens have four different slopes with a common trend of slope decreasing as the growth rate at the plastic crack propagation threshold increased. This problem was also observed by Usami [9], where all the curves for different materials showed a tendency toward slope change from steeper at close to the threshold to flatter at the end of the Region II growth. The long crack growth curve from [103] also showed the same tendency but was close to a straight line, as simplified in Figure 5.6. The free surface effect and the assumption of Q being a constant during Region II crack propagation are greatly responsible for this problem. The free surface effect to the Region II crack propagation will be further discussed in Section 5.3.

The total integrated fatigue lives were obtained by summing the initiation and the propagation lives. Comparison of integrated and experimental total fatigue lives of specimens and the proportion of crack initiation lives in total fatigue lives are listed in Table 5.3.

The error of predicted and experimental total fatigue lives is less than 5%. The new driving force and proposed model are thus proved by the sucessful application to the crack initiation analysis of present results. As for the proportion of initiation life to total life, three of the specimens have a crack initiation life of more than 80% of the total life, with the initiation lives increasing as the total fatigue lives increases.

Spec.	a_0	a_1	$N_i \times 10^{-4}$ (cycles)			$N_t \times 10^{-4}$ (cycles)			N_i/N_t
No.	(μm)	(μm)	Pred.	Exp.	Err.	Pred.	Exp.	Err.	(%)
#1	59	538	1.40	1.40	0	1.98	1.98	0	70.7
#301	70	641	1.77	1.70	4.1	2.21	2.13	3.6	79.8
#2	191	1750	10.55	10.3	2.4	12.8	12.2	4.9	84.4
#302	247	2260	23.22	22.5	3.2	26.7	25.8	3.5	87.2

Table 5.3: Predicted and Experimental Crack Initiation and Propagation Lives.

5.2.5 Analysis under Other Driving Forces

After the discussion of the newly proposed plastic strain intensity factor in the preceeding Section, the analysis shifts to other driving forces introduced in the short crack problem review in Chapter 2 for comparison. Because of limitations in the experimental technique, analysis in terms of promising parameters in short crack studies, such as the CTOD, is not yet viable, nor are analysis in terms of the crack depth, as has been discussed earlier. The modified ΔK or ΔJ analyses including the closure effect are also premature due to insufficient research. Moreover, if a closure effect analysis were possible, it would have already been included in the proposed model analysis.

The effective stress intensity factor proposed by El Hadded *et al* [93,94], Eqn

(2.3), is duplicated here:

$$\ell_o = \frac{1}{\pi} (\frac{\Delta K_{th}}{\sigma_o})^2, \tag{5.10}$$

where all the symbols are as defined earlier. Since the fatigue limit strengths for each specimen were not obtained, ℓ_o cannot be calculated from this formula. Nevertheless, to have a $\ell_o \leq 200\mu$m, an estimation from Eqn (5.10) indicates that σ_o has to be greater than 200 MPa, which is unrealistic for copper. Further decrease of σ_o causes an increase in ℓ_o making the crack growth curves versus the effective ΔK or ΔJ (especially in specimens #1 and #301) become straight vertical lines. The idea of ℓ_o as a material constant independent of applied strain level does not appear to be applicable in this case.

However, if the function of ℓ_o is to bring the short crack data closer to the long crack curve, this can be performed by a modified ℓ_o, designated as ℓ_1 hereafter, based on the ΔJ-integral analysis. This tentative ℓ_1 is constructed at the real crack length $a = 0$:

$$\sqrt{\Delta J \cdot E} = \Delta K_{th}, \tag{5.11}$$

where ΔJ has the form given in Eqn (5.3), while ΔK_{th} is the long crack propagation threshold determined by LEFM methods. For copper, it is 5 MPa. Therefore,

$$\sqrt{(3.0\, \Delta W_e + 5.0\, \Delta W_p)\, E\, \ell_1} = 5.0\,. \tag{5.12}$$

From Eqn (5.12), ℓ_1 is obtained as:

$$\ell_1 = \frac{25.0}{(3.0\ \Delta W_e + 5.0\ \Delta W_p)\ E}. \tag{5.13}$$

By replacing the half crack length, a, in Eqn (5.3) by $a + \ell_1$ and performing the modified $\sqrt{\Delta J \cdot E}$ analysis, it was found that the present crack initiation and early propagation results indeed became close to the long crack curve, as shown in Figure 5.11. The interesting feature of this modified fictitious initial crack length method is that all the crack propagation curves are parallel with the same slope in the propagation region with an expression of:

$$\frac{da}{dN} = \eta\ (\sqrt{\Delta J \cdot E})^{4.01}, \tag{5.14}$$

where η has different values for each specimen. For example, it takes the values of 2.14×10^{-12} and 5.89×10^{-13} in specimens #1 and #302 respectively. The integration of Eqn (5.14) from the crack lengths ℓ_1 obtained in Eqn (5.13) which are 27.8 μm and 117 μm for specimens #1 and #302, to a_N values of 538 μm and 2.26 mm for the two specimens respectively, gives a fatigue life of 19,300 cycles and 2.45×10^5 cycles, which are very close to their experimentally determined values.

On the other hand, there are uncertainties concerning this tentative method. For example, the physical meaning of ℓ_1 determined this way cannot be explained. Whether the accurate integration results are merely a coincidence or have some profound meaning, and how to interpret the fact that integration of only the crack

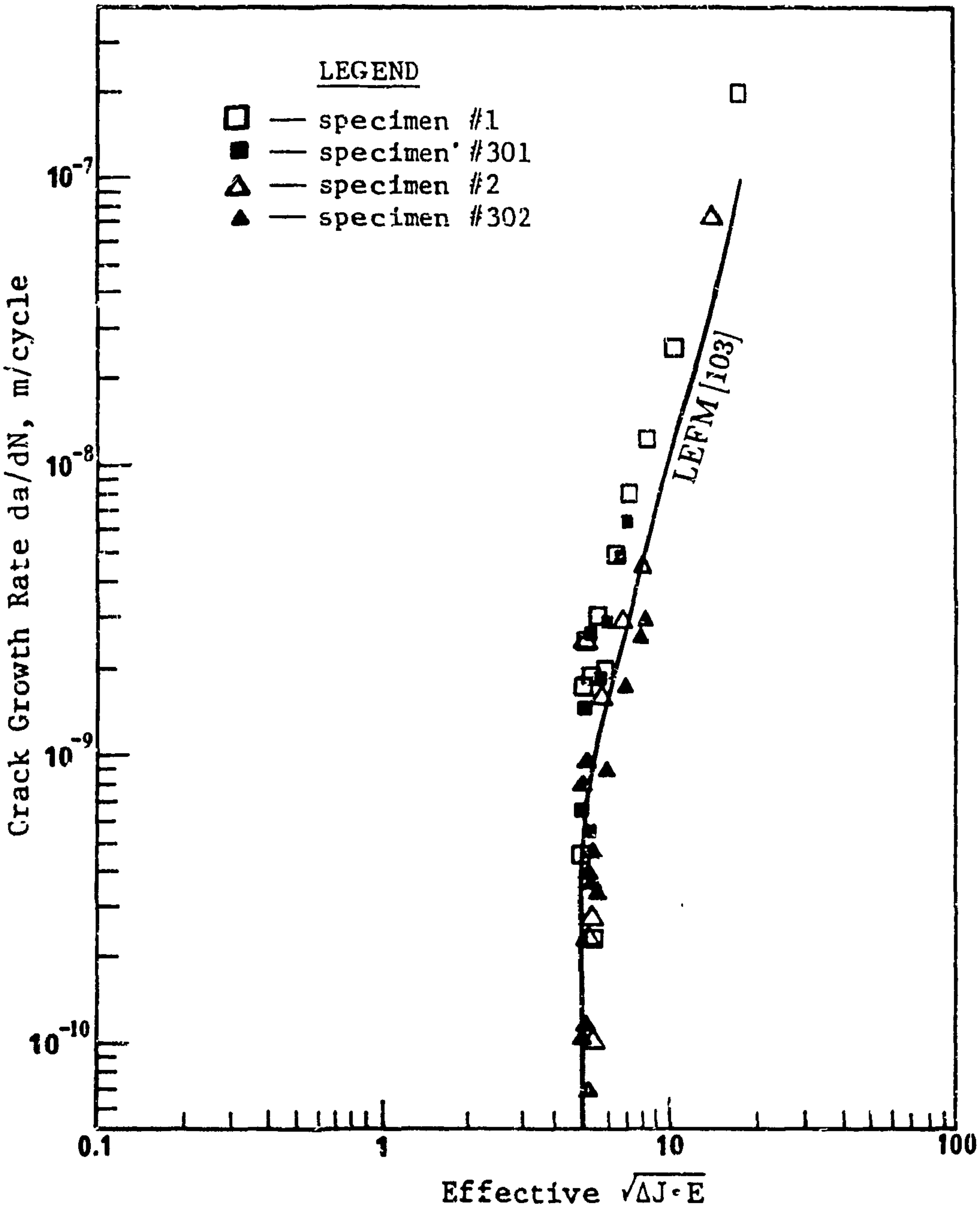

Figure 5.11: Crack Growth versus Modified Effective $(\Delta J \cdot E)^{1/2}$ in Relation with the ASTM E647 Determination of the LEFM Curve.

propagation part gives the total fatigue life of the sample are questions that cannot be answered. Besides, the way it compresses the whole initiation region into a vertical stright line is similar to the way the conventional crack propagation threshold was formulated by the conventional stress intensity factor in the LEFM analysis as has been discussed before. This compression not only erases the abnormal behaviour of the initiation region, it erases all the crack initiation features too, making the crack initiation and early propagation analysis impossible. Therefore, it can be concluded that the original or the modified fictitious initial crack length method is not as good as the proposed mechanical model in crack initiation and early propagation studies.

5.3 Testing of Mechanism Models

5.3.1 Introduction

Discussion in this Section will concentrate on two representative specimens, specimen #1 representing #1, #2 and #301 in low cycle fatigue where fatal cracks often initiate at grain boundaries, and specimen #302 representing high cycle fatigue where fatal cracks often initiate on slip bands or PSBs.

5.3.2 Sub-Microcrack Initiation and Nucleation and Microcrack Propagation Studies by Replica Technique

Strain Hardening/Softening and Slip Band Formation

Replica studies by both optical and scanning electron microscopes revealed that slip lines form early in the fatigue process, far before the strain hardening or softening processes are completed. The SEM photograph of slip lines in Figure 5.12 (b) of specimen #1 at 50 cycles (its strain softening process was completed at about 500 cycles) is one example, although these slip lines did not serve as fatal crack initiation sites. Another SEM photograph presented in Figure 5 12 (a) is from the earliest surface replica of specimen #302 which recorded the sub-microcrack formation on slip bands of this sample at N = 1000 cycles (its strain hardening process was completed around 1000 cycles). Those PSBs served as the main crack initiation site. Since the sub-microcracks in this sample were already clearly distinguishable at N = 1000 cycles, the slip bands must have formed earlier at the time strain hardening was taking place. The early formation of slip lines provided the foundation of earlier crack initiation on slip lines in high cycle fatigue compared to crack initiation at grain boundaries in low cycle fatigue.

Sub-Microcrack Initiation, Nucleation and Microcrack Propagation

Figure 5.13 presents a group of photographs from the replicas of specimen #1, showing the fatal crack evolution process. These photographs demonstrate the good quality of the replicas and their treatment. The surface topography in this low cycle fatigue sample is characterized by severe concave and convex grains.

At the end of its strain softening process (N = 500 cycles), the sub-microcracks at grain boundaries in specimen #1 were not as pronounced as some of the slip band cracks in the same photograph, refer to Figure 5.14. The fatal crack initiation in this sample is not early; however, the sub-microcracks nucleated fast as the test progressed, as proposed in the model. Figure 5.13 (a) demonstrates the fatal crack at N = 1000 cycles, when it looks as prominent as the slip band cracks. The sub-microcracks grew rapidly within a few thousand cycles until it reached the microcrack formation at N = 4000 cycles (Figure 5.13 (b)). The lengths of microcracks are less than the average grain size in this sample.

Now the microcrack was at its sub-threshold. Among the reasons given in the models for the growth retardation are: the shallow depth, the decay of free surface effects and the change of plane; of these the first two are clearly valid while the validity of the last doesn't seem to be as obvious for this specimen. As seen from Figure 5.13 (b), some of the microcracks are themselves not strictly on one plane because the grain boundaries are not straight.

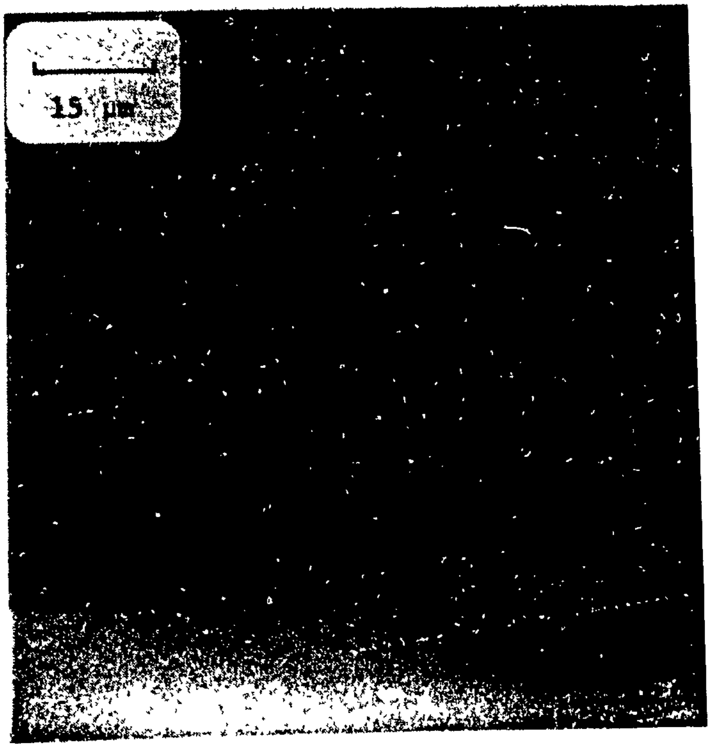

(a) Specimen #302 at N = 1000 cycles.

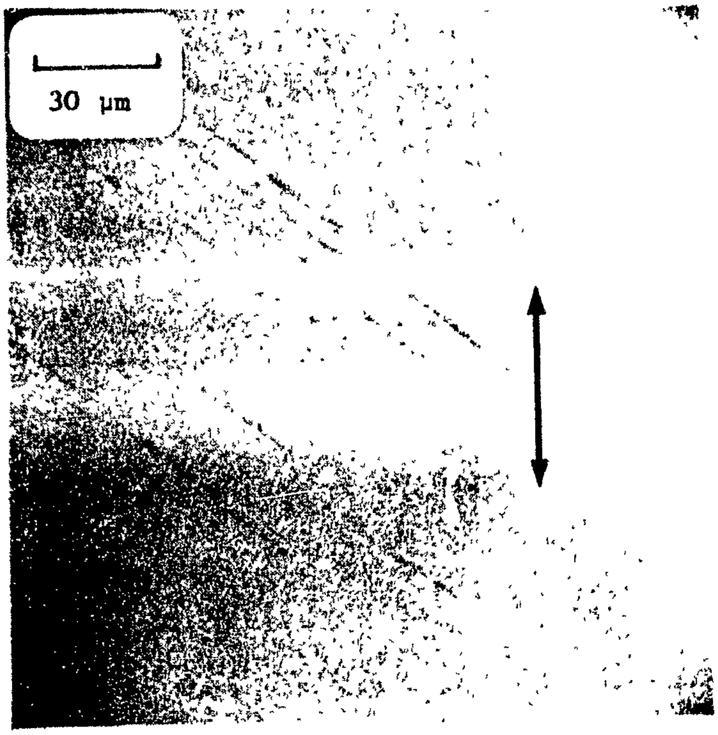

(b) Specimen #1 at N = 50 cycles.

Figure 5.12: Early Slip Band Formations. (load direction shown by double arrow)

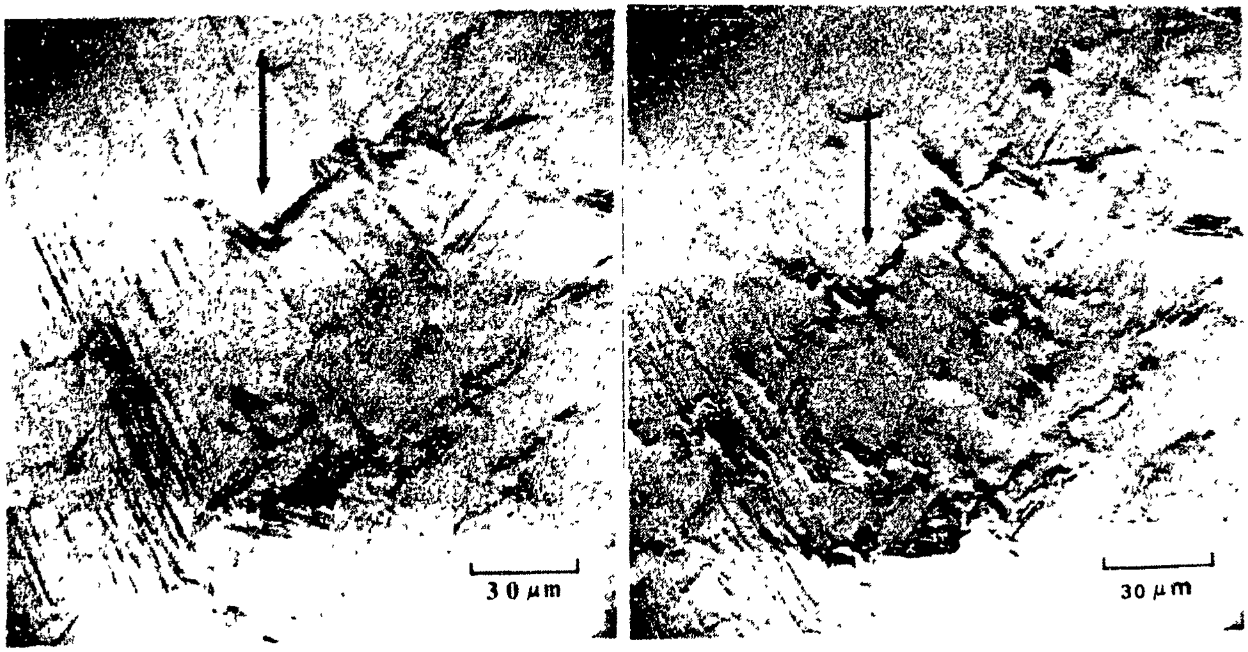

(a) Sub-microcrack formation and nucleation, N = 1000 cycles.

(b) Microcrack formation, N = 4000 cycles.

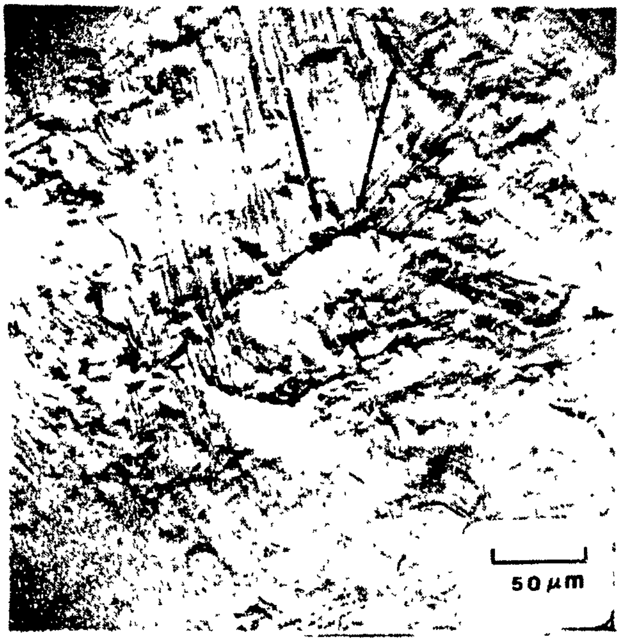

(c) Microcrack Propagation, N = 8000 cycles.

Figure 5.13: The Evolution of the Fatal Crack in Specimen #1, $N_f = 19,800$ Cycles. (crack shown by arrow and load direction shown by double arrow)

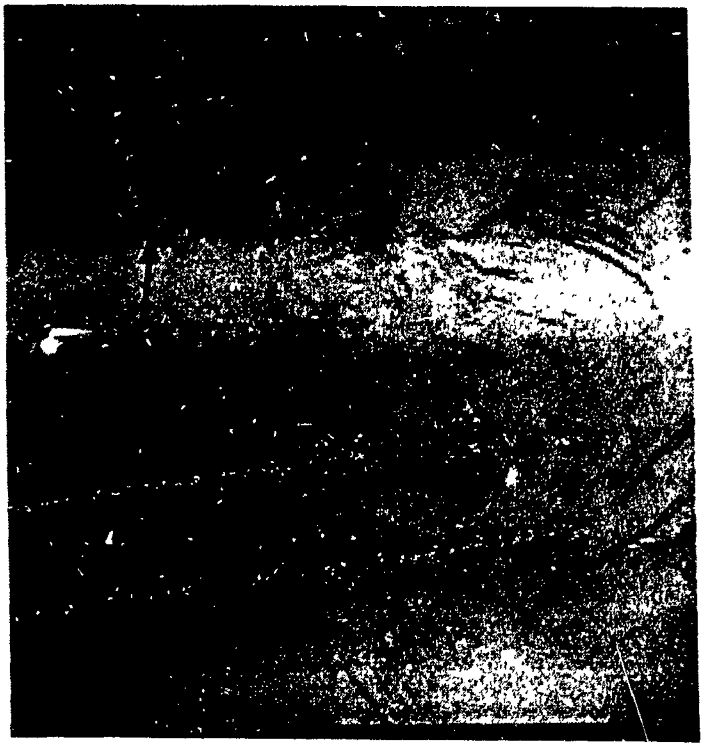

Figure 5.14: Crack Initiation site at N = 500 cycles in Specimen #1, $N_f = 19,800$ Cycles. (Crack shown by arrow and load direction shown by double arrow)

After overcoming the sub-threshold obstacles, the fatal crack resumed its growth. Although at microcrack initiation it was hard to say which was the larger and which was the major among those microcracks existing at the initiation site, since they look equally important (refer to Figure 5.13 (b)), the major part of the fatal crack became clear as the microcrack propagation continued. Figure 5.13 (c) depicts a stage in the growth of microcracks towards the plastic crack propagation threshold when the major part of the fatal crack became clear and predominant in comparison with the new microcracks initiated at the two ends of the major microcrack. This is the steady Stage I microcrack propagation between the sub-threshold and the plastic crack propagation threshold in the initiation region; it is also the stage when the three-dimensional Stage I propagation starts. In Figure 5.13 (c), the first microcrack expansion from the two sides of the "V" shape along the cone surface was just completed at the tip of the "V". The replicas of the fatal cracks in both specimen #1 and #2 clearly show a "V" shape on the specimen surface, an indication of the Stage I propagation proposed in Chapter 3. More discussions about Stage I propagation will be found in a later Section with the fractographic surface studies.

Figure 5.15 contains a group of SEM photographs of the specimen #302 surface replicas. The number of cycles from (a) to (d) are 4,000, 60,000, 100,000 and 130,000. No pronounced concave and convex grains are seen and the surface is much smoother than in the low cycle fatigued sample. Figure 5.15 (a) illustrates the early sub-microcracks initiating along the slip bands. From their behaviour, these slip bands may actually be PSBs However, since there is no experimental proof of the point, they are simply identified as slip bands.

The crack evolution process in #302 has some interesting features concerning how

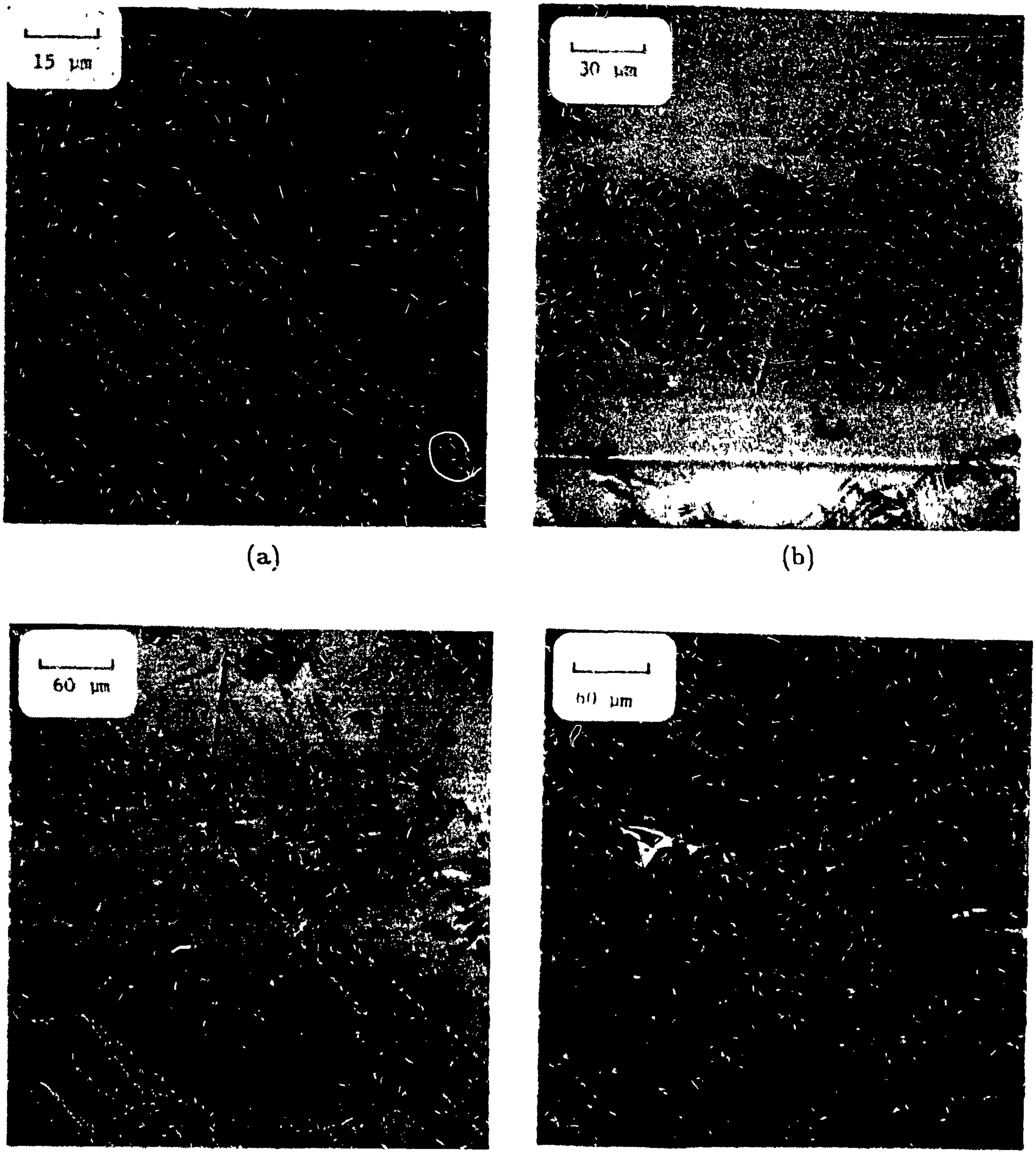

(a) (b)

(c) (d)

Figure 5.15: The Sub-Microcrack Nucleation of the Main Crack in Specimen #302, $N_f = 260,000$ Cycles. (load direction shown by double arrow)

sub-microcracks initiate and nucleate along slip bands or PSBs. As was demonstrated by Hunsche and Neumann [106], for annealed copper single crystals grown from 99.99% OFHC copper, cracks initiated throughout PSBs, but the preferred positions where cracks may grow deep and lead to failure, are along the interface between PSB and matrix (Figure 5.16).

The sub-microcracks of the main crack in specimen #302 initiated on two sides of the slip bands in grains with larger than average grain sizes. The sub-microcrack initiation and independent growth in this sample was fast, until the sub-microcracks overlapped, one on top of the other. Figure 5.15 (b) illustrates the microcrack in between the first sub-threshold and the second sub-threshold, revealing the unbroken layer between the two parts of the sub-microcracks with the left half running parallel and on top of the right half. Meanwhile, the left half was already joined by the sub-microcrack in the next grain crossing the grain boundary. Grain boundaries are not necessarily better crack inhibitors than the slip band width which separates the sub-microcracks in a grain.

Due to the difficulties in crossing unfavourable slip planes, as discussed in Chapter 3, the high cycle specimen #302 not only experienced two sub-thresholds, but also had a long sub-microcrack nucleation time. While the coalescence of sub-microcracks to form a microcrack in the three low cycle fatigue specimens occurred in less than 20% of their total lives, it took the high cycle specimen #302 70% of its total life to complete this process.

The replicas of specimen #302 do not indicate clear Stage I crack propagation. Therefore, although the crack growth rates of a main crack are not much lower

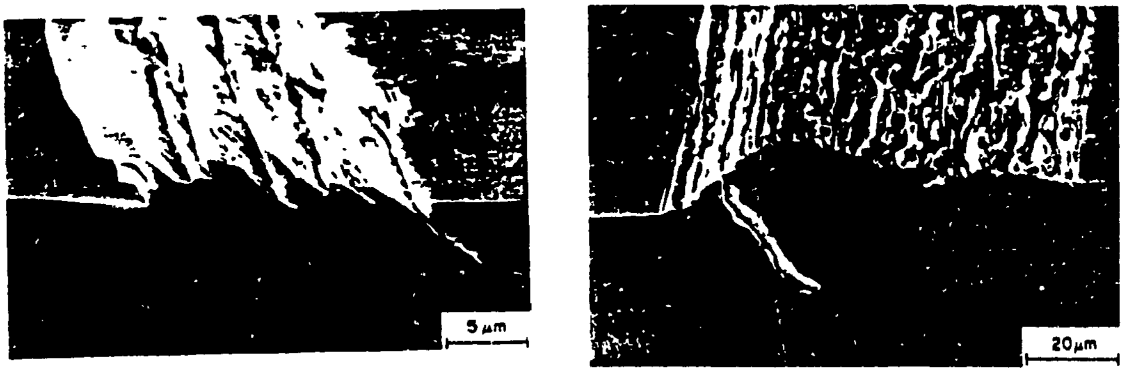

Figure 5.16: Crack Initiation and Propagation Close to the Edge of Extrusion on PSBs. *ref* 106

than those of a fatal crack in the initiation region, the mechanisms of main crack propagation are essentially different from the ones of fatal crack propagation.

Crack Initiation Characteristics

Of the three grain boundary crack initiations, the sites of #1 and #2 were at slip band interacted grain boundaries, with one side heavily marked with slip bands while the other side was relatively free of them. The initiation site of #301 was at a grain boundary where neither side showed much slip deformation (Figure 5.17). These coincide with the crack initiation site for low cycle fatigue proposed in Chapter 3. It is evident that the plastic deformation in these slip line free grains was highly constrained. This, in turn, provoked a localized strain concentration at grain boundaries, which facilitated crack initiation. Whether the grain on the slip free side has a cell structure, or has only a main slip system unfavorable to the applied load, cannot be determined from these replicas.

In this investigation, however, grain boundary cracks were not found to be associated with grain boundary steps in all cases. Instead, grain boundaries were simply opened by the highly localized shear strain. In some cases several sub-microcracks were first initiated along the grain boundary, as indicated by Figure 5.17, prior to their rapidly joining to become one microcrack along the grain boundary, as described by the Stage I sub-microcrack propagation model in Chapter 3.

Compared to 3% which is the average percentage of sub-microcrack initiation in total life in the low cycle specimen samples, the percentage is 0.4% in the high cycle specimen. The crack initiation characteristics at the slip band within the large grain is also as described by the model. Although it has been demonstrated in Figure 5.15 that the sub-microcracks initiated from both sides of the slip band, the replicas did not provide further information about whether the sub-microcracks were initiated from a intrusion or the interface between an extrusion and the bulk material. However, the post-experimental real specimen surface examination discussed in the next Section answered this question.

5.3.3 Post-Experimental Specimen Surface and Sub-Microcrack Initiation Site Examination

There is no doubt that the replica technique facilitated crack initiation studies. Unfortunately, like every experimental technique, it has its limitations. For example, replicas cannot record the depth of the crack beyond a certain limit because they either cannot penetrate to the bottom of the crack, or get torn when peeled off from

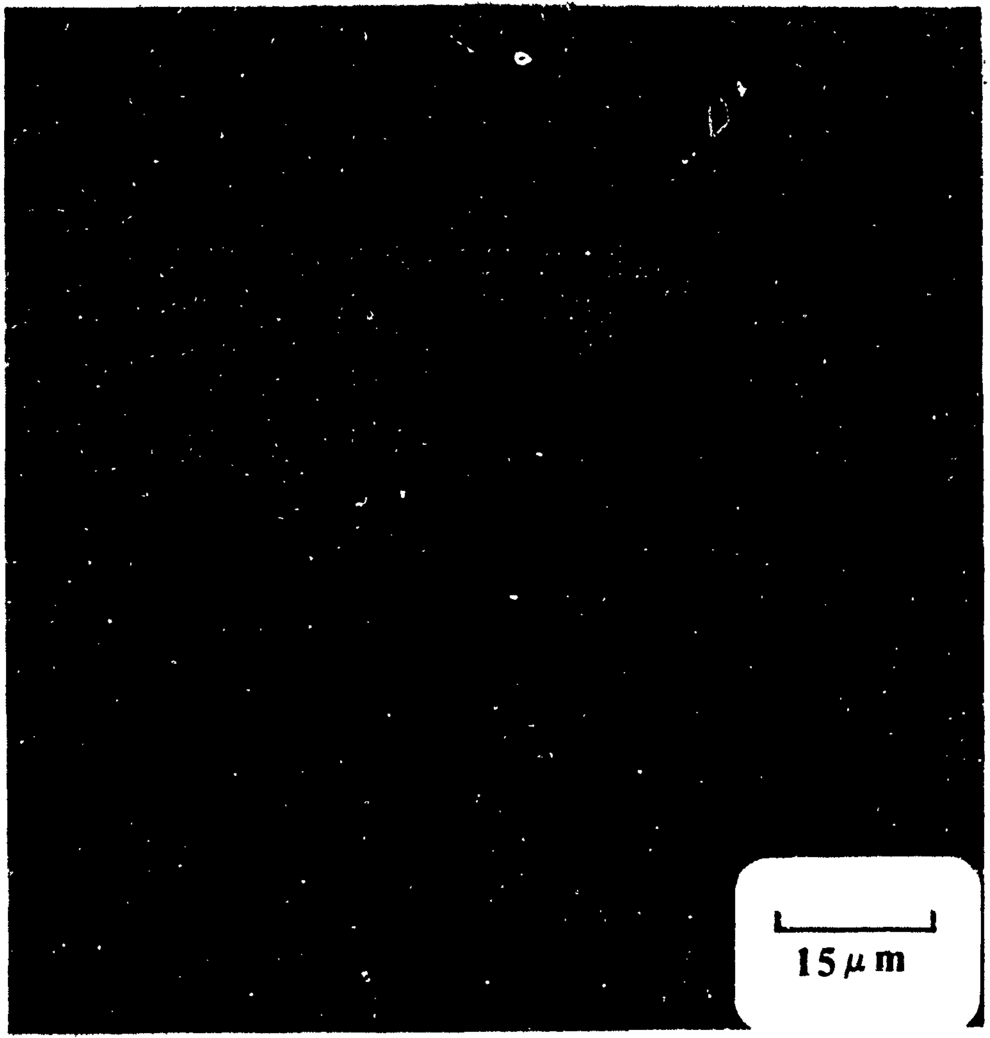

Figure 5.17: Sub-Microcrack Initiation Developing Into a Main Crack at a Grain Boundary. Specimen #301, N = 400. (crack shown by arrow and load direction shown by double arrow)

the surface. They cannot record sharp extrusions either, for the same reason. Moreover, as the specimen surface becomes rougher and the fatal crack grows deeper, plastic replicas became even less reliable. It was found during testing that when the specimen surface damage became more pronounced under fatigue loading, air bubbles were more difficult to avoid when depositing replicas onto the specimen surface, longer time was needed for them to dry, and peeling them off from the surface was more difficult, suggesting that the replicas were caught at some rough places. Nontheless, replicas were mainly used for recording crack lengths, especially at the earlier stages of the tests. To obtain first-hand knowledge about the mechanisms of crack initiation, general surface observations were performed on the specimens after testing.

Successfully tested specimens were cut to smaller sizes, to fit the chamber of the SEM and were viewed. Figure 5.18 is the photograph of the surface of specimen #1 taken at the edge of one small part of its fatal crack, illustrating typical surface features of a low cycle fatigue specimen. Generally speaking, the characteristics shown here are similar to the ones elicited by replicas (further proving the reliability of the replicas), except that the surface topography near the edge of the fatal crack looks even more concave and convex than it does in the replicas. Microcracks along grain boundaries and slip bands exist at the same time, marking the surface as a combination of profuse total grain deformation and dense slip band formation within the grains in this specimen. It is not that cracks fail to initiate along slip bands in low cycle fatigue; on the contrary, initially the slip band induced cracks initiate earlier and grow faster than the grain boundary cracks, but after a certain point, the grain boundary cracks grow faster than the slip band cracks. As has been discussed in the case of specimen #302, slip band crack nucleation and growth took a long time. It is quite possible that while slip band cracks are still attempting to change planes or cross grain boundaries, the grain boundary cracks had already passed through the plastic crack propagation threshold.

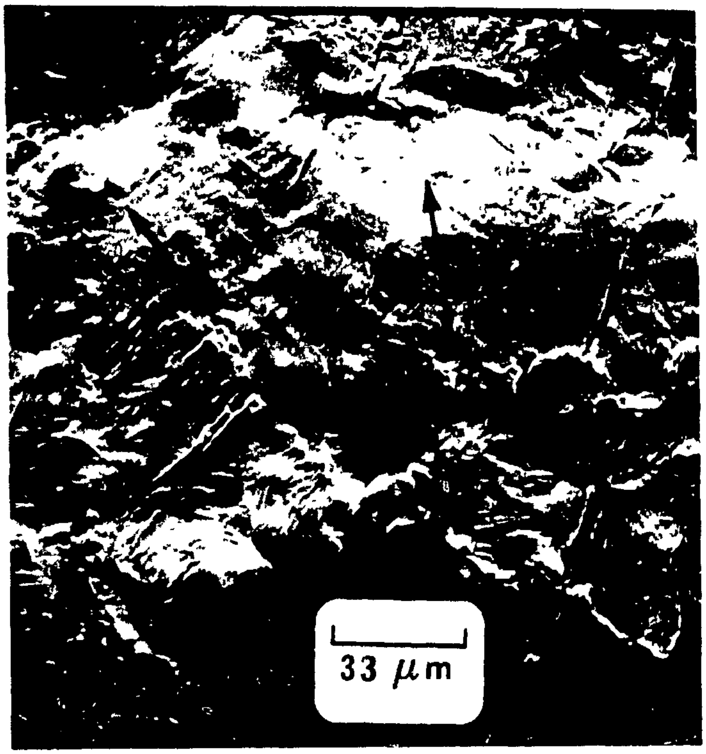

Figure 5.18: Surface Topography of Specimen #1. (Flower-like extrusion indicated by arrow and load direction shown by double arrow)

The Region *II* crack propagation in specimen #1 alternated from intergranular to transgranular, as indicated in Figure 5.18. At the lower right corner of the picture, the crack path runs along a slip band prior to running along grain boundaries. Once the crack is established, it goes through what lies ahead of it by choosing the smallest angles between grain boundaries or slip systems.

Flower-like extrusions were found at the left upper corner of the photograph in Figure 5.18. This is not the only spot with this kind of extrusions, since many can be found on the surface of this specimen. These excessive extrusions must be encouraged by the bigger strain amplitude which provided a much larger compressive stress than in the case of specimen #302 since no similar flower-like extrusions were detected on the surface of #302.

Figure 5.19 contains two pictures of specimen #302, one taken at a place where slip bands are very dense and another at the main crack initiation site so that the remaining question about the crack initiation can be answered. As indicated in Figure 5.19 (a), even in the highly damaged part of specimen #302, the surface still looks much flatter than that of #1. No overall grain dents and bumps were observed, for damage is well localized within the grains. Long grain boundary microcracks are seldom seen, guaranteeing that slip induced cracks had enough time to develop and lead to final failure.

From Figure 5.19 (b), in the large grain where the main crack was initiated, it is clearly seen that the main crack developed from intrusions. Although one may argue that the possibility exists of later crack development destroying the extrusion, all the other slip band intrusions remaining in the grain are sufficient to highlight the point that crack initiation developed from intrusions in this case.

As to how the sub-microcracks were initiated on PSBs, previous discussion of

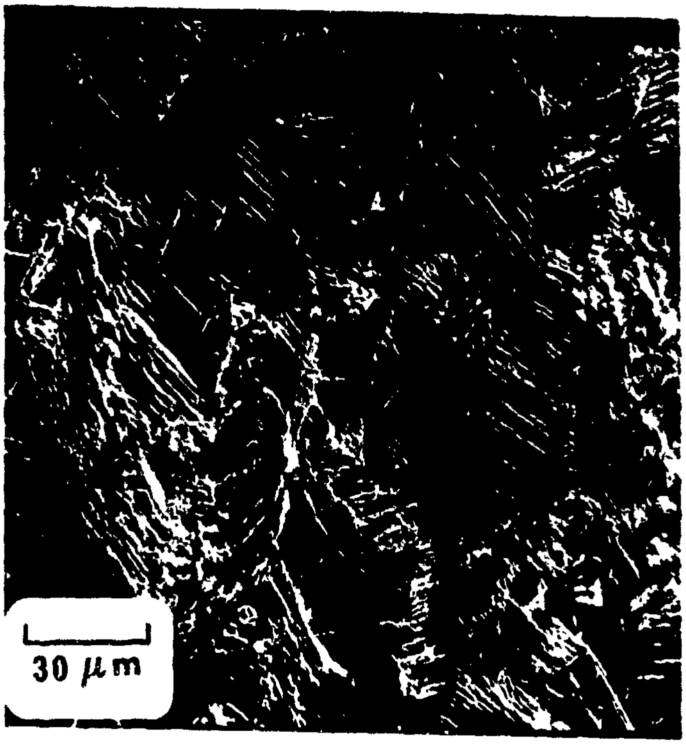

(a) General surface topohgraph

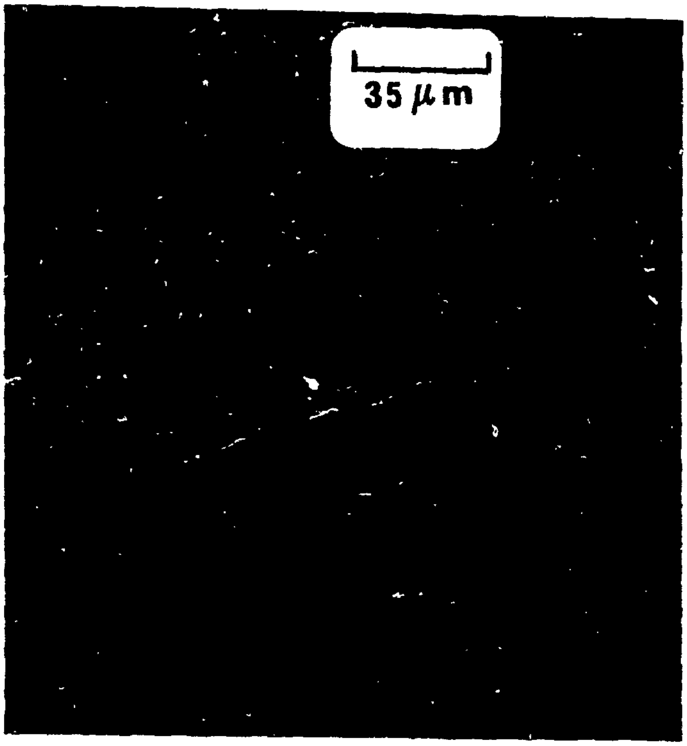

(b) The main crack initiation site

Figure 5.19: Surface Topography of Specimen #302. (load direction shown by double arrow)

replicas revealed that sub-microcracks were initiated on the two sides of the slip band. This is further verified by Figure 5.19 (b), where the large piece of debris left on the lower bank of the crack indicates that a sub-microcrack must have initiated at the upper side of the slip band, while other sub-microcracks initiated on its lower side. The slip band width had separated the sub-microcracks before they managed to cross the plane and join each other. Thus, the crack initiation site in high cycle fatigue has also been showed to follow the model.

SEM examinations at a higher magnification of the surfaces of the two specimens are given in Figure 5.20, where (a) is from specimen #1 and (b) from #302. In both of the specimens, extrusions and intrusions are observed while intrusions appear often in partnering the extrusions at their roots. Even though specimen #1 was expected to be more extrusion dominated than specimen #302 due to the higher hardness of the specimen, it is difficult to conclude this after a careful surface search. Since these two specimens are the two extreme cases (one is the hardest and the other is the softest), it can be concluded that extrusion and intrusion both develop at the surface of specimens under the material condition and stress-strain levels investigated.

Despite the similarity of the two specimens in regard to extrusions and intrusions, the enlarged photograph of the surface of specimen #1 in Figure 5.20 (a) does show a microscopic feature different from that of specimen #302 in Figure 5.20 (b). This is the secondary slip in some of the smaller grains due to the higher stress-strain level applied in the case of specimen #1. In those grains showing secondary slip, localized plastic strain within slip band is limited; hence no severe extrusion and intrusions are observed.

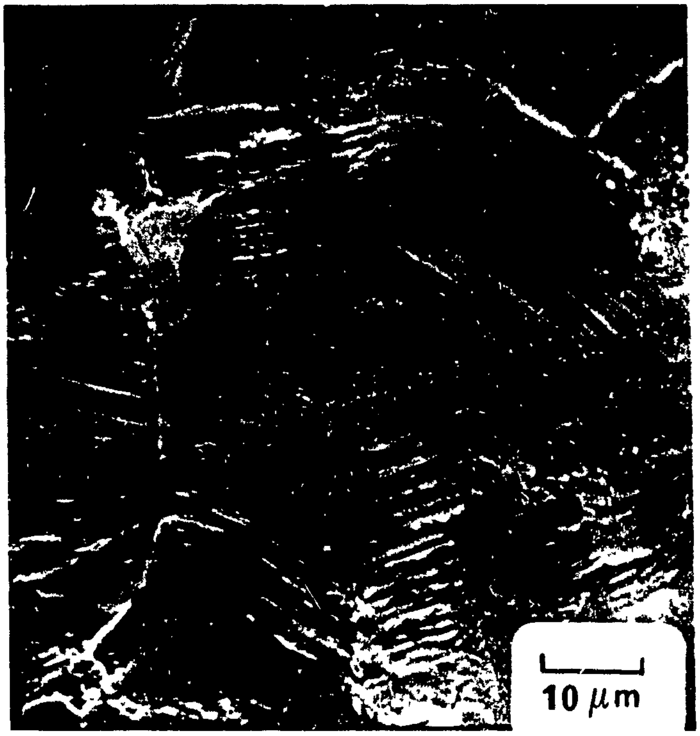

(a) Specimen #1

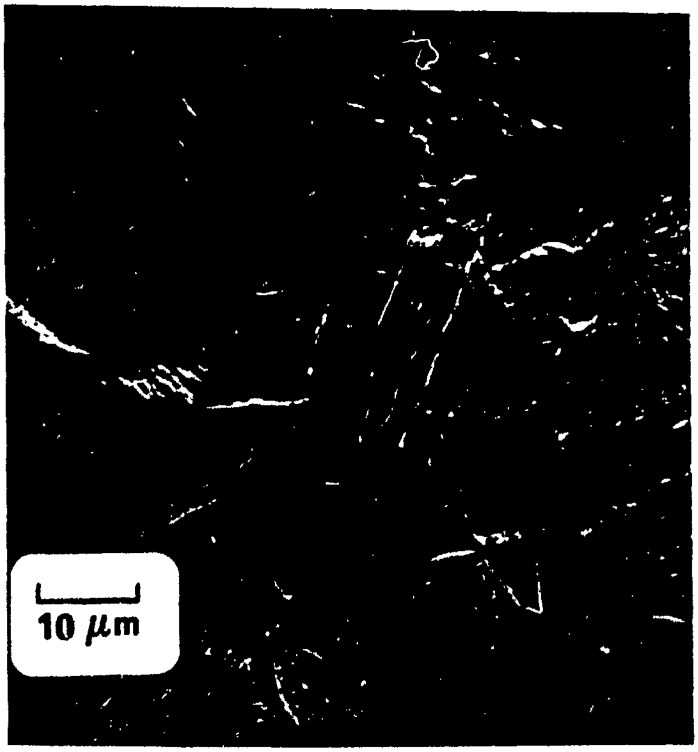

(b) Specimen #302

Figure 5.20: Detailed Extrusion and Intrusion of Specimen Surfaces. (load direction shown by double arrow)

5.3.4 Testing of Stage I Propagation Model and Crack Profile Changes by Fractographic Studies

Macroscopic Observation of Fractographic Surface

After surface viewing, the specimens were pulled apart for fracture surface examination. Figure 5.21 shows the fractographic surfaces around the fatal crack initiation region of specimens #1 (Figure 5.21 (a)) and #302 (Figure 5.21 (b)) under low magnification. The irregular line close to the edge in #302 is either surface damage due to corrosion or the trace of a replica or solvent left on the surface during the replica making process.

Both of the fractographic surfaces in Figure 5.21 can be divided into two parts:

1. the relatively featureless part located in the center of the photograph with a half circle shape, designated as part I, and
2. the rest of the surface with radiation lines, designated as part II.

The radius of the half circle in Figure 5.21 (a) is about 0.5 mm, while it is about 1.4 mm in Figure 5.21 (b). Both are much larger than the initial engineering crack sizes, a_0, of 59 and 247 μm of specimens #1 and #302. On the other hand, the estimated critical crack lengths, a_N, at the transition from Region II to Region III propagation obtained from the analysis for the two specimens are 0.538 mm (very close to 0.5 mm) and 2.26 mm (much closer to 1.4 mm than 247 μm) respectively. Therefore, part 1 is the site where Region I_p and Region II crack initiation and propagation took place while part II is the site where Region III crack propagation took place.

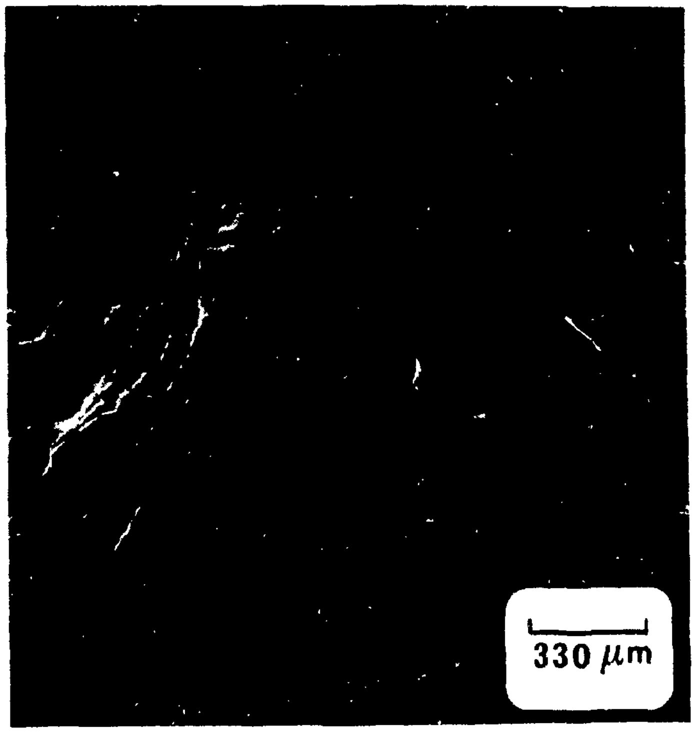

(a) Specimen #1

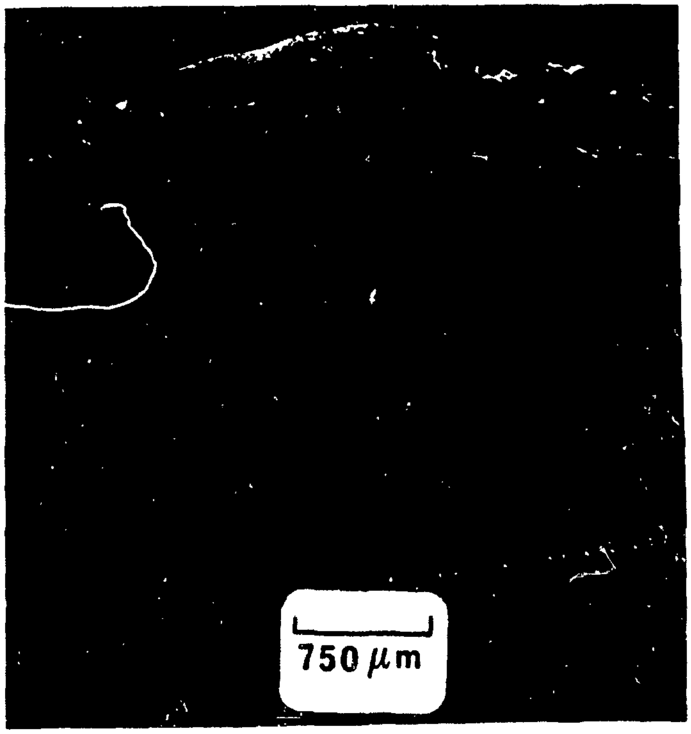

(b) Specimen #302

Figure 5.21: Fractographic Surfaces of Specimens under Low Magnification. (crack initiation sites indicated by arrows)

The actual crack length of specimen #302 at the transition of the two parts, from the measurement, is considerably smaller than that derived from the energy method. The cause of this discrepancy is mainly the error in the evaluation of ΔJ introduced by the large crack size at the plastic crack propagation threshold. However, this discrepancy does not mean that the energy level ΔJ as a control measurement in the transition of crack initiation and propagation should be denied since it does perform well in controlling the transition from Region I_p to Region II, a point which will be further demonstrated in the following Section.

Testing of Stage I Propagation Model

The analysis of Section 5.2 revealed the correct size of the crack initiation site, which can be *very* small depending on the applied stress level. With patience, skill, and this important information, the white, lightly indented spots (indicated by arrow) on the fractographic surface in Figure 5.21 were identified as initiation sites for the two specimens. Enlarged photographs of the initiation site of specimen #1 are presented in Figure 5.22.

With the stage holding the specimen mount tilted at 10°, the crack initiation and early propagation site appears as a shallow "V" in Figure 5.22 (a). To better analyse Figure 5.22, the corresponding photograph of the replica at close to crack initiation is presented in Figure 5.23 which clearly indicates the "V" shape of the crack origin. The combination of the fractographic surface observation and replicas gives very good pictures of crack initiation and early propagation and is the basis of the model proposed in Section 3.3.

The replicas of this specimen (refer to Figure 5.13) indicated that the sub-

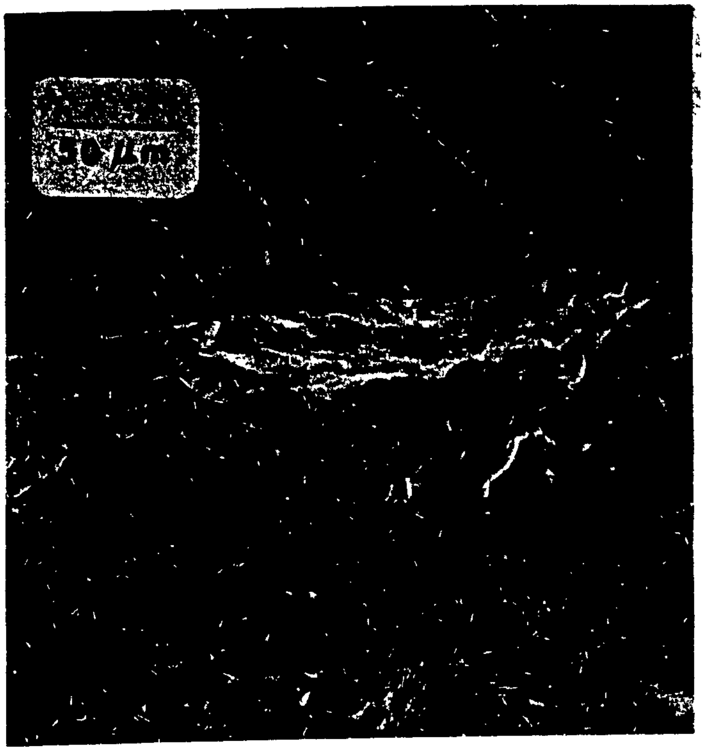

(a) Crack initiation site

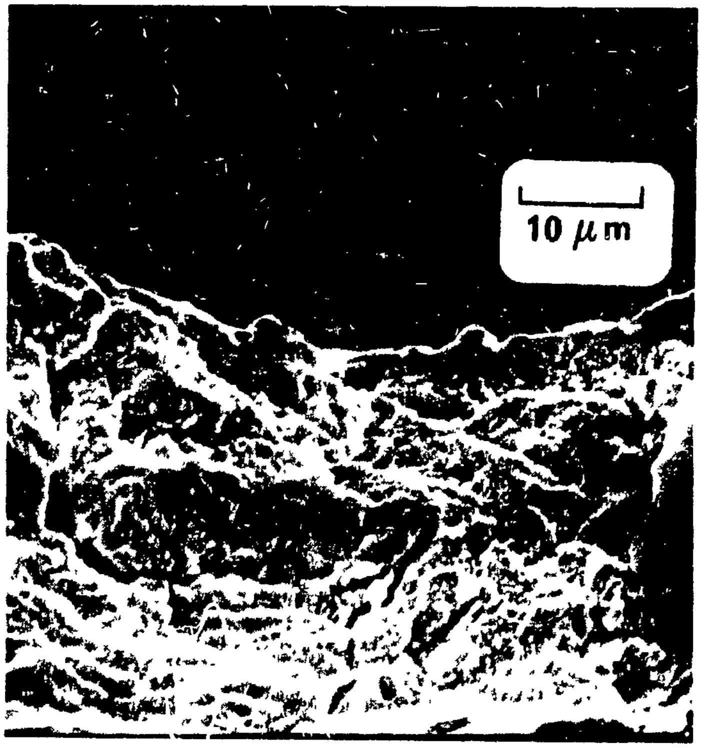

(b) Details of crack initiation site

Figure 5.22: Crack Initiation Site on Fractographic Surfaces of Specimen #1.

Figure 5.23: Crack Initiation Site Recorded by Replicas of Specimen #1, N =14,000 Cycles. (crack shown by arrow and load direction shown by double arrow)

microcracks and microcracks initiated on both banks of the "V", as proposed in Chapter 3. While the coalescence of the microcracks was taking place on both banks, it was more advanced on the right side than the left side. When the coalescence on the right side was completed, the tip of the "V" was formed. A three-dimensional Stage I propagation cannot be observed from the replicas, but thanks to the ripple lines (which are the white lines at the crack origin in Figure 5.22) left on the fractographic surface, the Stage I propagation can be discerned on fractographic surfaces in Figure 5.22. Taking the newly formed "V" tip as the base, another part of the joined microcrack on the right bank expanded along a surface (one of the two surfaces discussed in Section 3.3) to the left side. According to the ripple lines, there are four similar expansions in the Stage I crack propagation process of this sample. After the fourth expansion was completed, the crack reached the plastic crack propagation threshold and the Stage I propagation came to an end.

The half crack length, a, as measured from the widest white ripple line bands on the left end of the "V" to the first ripple line on the right side of "V" in Figure 5.22 (a) and divided by 2, is 60 μm, in comparison with the predicted initial engineering crack size a_0 value of 59 μm. Therefore, the transition of Stage I to Stage II crack propagation indeed takes place at the proposed plastic crack propagation threshold in specimen #1.

The examination of replicas of the fatal crack in another low cycle fatigued specimen, #2, showed Stage I propagation similar to that of #1 with slight differences in the process. In specimen #2, microcracks were developing on one side of the "V" for quite a period before the tip of the "V" appeared and the tip of the "V" is not as sharp as the one of specimen #1.

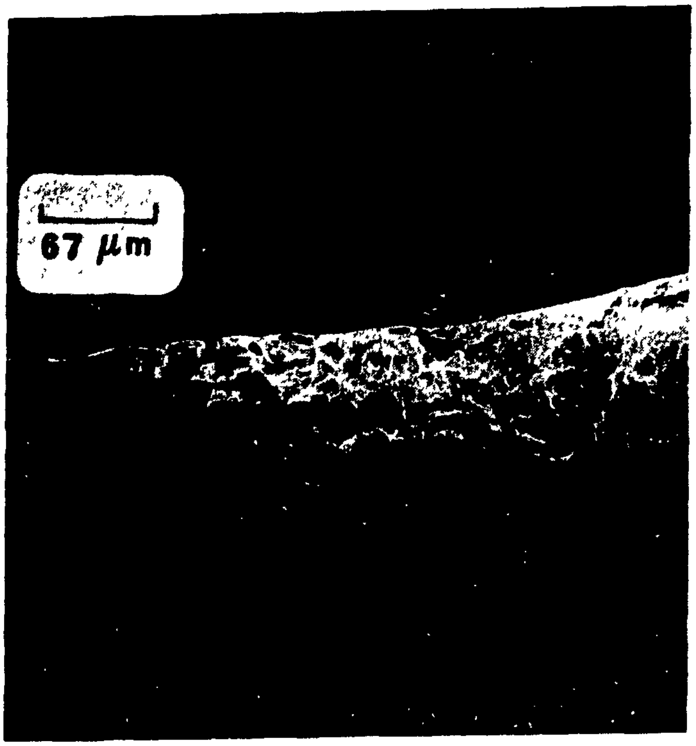

(a) Crack initiation site

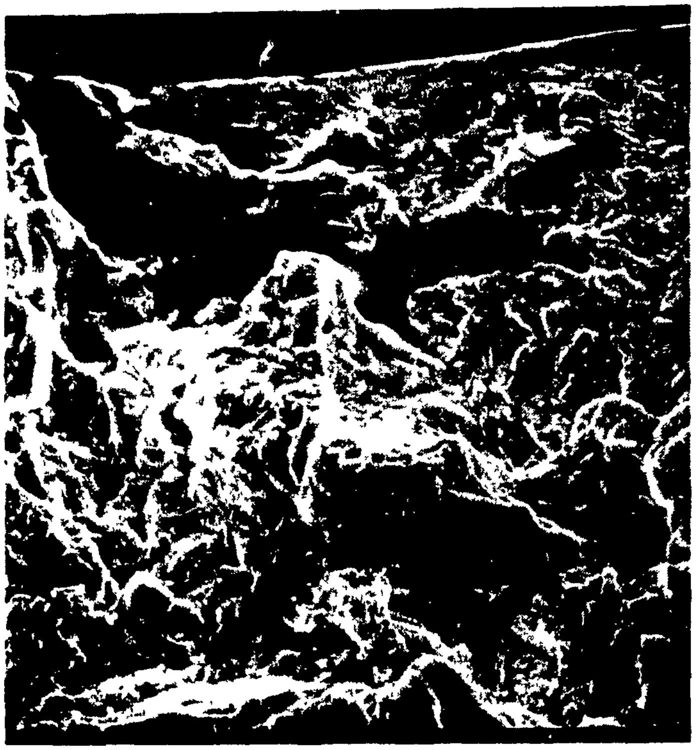

(b) Details of crack initiation site

Figure 5.24: Crack Initiation Site on Fractographic Surfaces of Specimen #302.

The fractographic surface studies of specimen #302 provided more evidence for the Stage I propagation model. Figure 5.24 presents the fatal crack initiation site of specimen #302. Unfortunately, the initiation site is partly damaged, and there are also no corresponding replicas accompanying this fatal crack. Nevertheless, it still reveals several important features. One of them is the "V" shape of the initiation region. The Stage I crack propagation surface also seems to be a combination of a cone surface and an elliptical plane, in much the same way as in specimen #1. The "V" is shallower than on specimen #1, indicating a bigger portion of the two-dimensional plane in Figure 3.5 (b).

The above discussion of Stage I crack propagation thus proved the Stage I crack propagation model in cylindrical specimens proposed in Chapter 3. This model works not only in grain boundary crack initiation, but also in slip band crack initiation. At the same time, the above quantitative analysis of the crack size at the transition from stage I to stage II propagation also further proves the definition of the plastic crack propagation threshold and the initial engineering crack size to be on a solid foundation. A semi-elliptical crack profile is indeed formed at the plastic crack propagation threshold, even though its aspect ratio may be small, as in the case of specimen #1.

Crack Shape Changes in the Initiation Region

Furthermore, the fractographic study provides information about the crack profile changes at very short crack lengths. Ripple lines in Figure 5.22 (a) showed some shallow semi-ellipses in the Stage I microcrack propagation of specimen #1. An estimation of λ, the aspect ratio, values of the four discernible semi-ellipses indicated that these values are similar and range from $0.4 \sim 0.5$. However, these values cannot be considered as the aspect ratio of the crack since the "handle" sticking out at one vertex of the semi-ellipse (refer to Chapter 3) considerably reduced the λ value of the microcrack, especially at the beginning of Stage I propagation when the "handle" is much longer than the depth of the semi-ellipse.

Further quantitative analysis of crack shape versus number of cycles in Stage I propagation is premature, since when the expansions from one side to the other were completed cannot be determined individually from the present fractographic surface and the replica studies. However, if what Newman [90] observed is true ($P_o/P_{max} = -1$ at small crack length and transfers to $0.3 \sim 0.4$), the aspect ratio λ must have changed smoothly from zero to close to 0.4 at the threshold.

The last λ value that could be determined from the ripple lines is 0.34 taken right after the threshold. Although λ can no longer be convincingly obtained beyond this point, an upper limit of the crack size when the ratio λ can be determined with confidence to be close to unity is 500 μm. This upper limit is the diameter of the half circle zone before radiation lines start. The subsequent specimen shape keeps its half penny configuration.

Despite the damage to the fractographic surface in specimen #302, ripple lines showing crack profile and microcrack nucleation processes are still clear (Figure 5.24 (a)). The λ values of early semi-ellipses descernible on the fractographic surface from the ripple lines are around $0.4 \sim 0.5$, similar to specimen #1. Comparing specimen #302 and #1, there is a major difference in the last λ values of the semi-ellipse on the fractographic surfaces. The semi-ellipse of specimen #302 became nearly a half circle at the end of Stage I propagation with the help of the indicated circle at the center of the crack which connected the two previous microcracks. After this event, the aspect ratio λ was raised from 0.4 to 0.83.

The small value of λ at the microcrack propagation region is apparently caused by free surface effect. Complete free surface decay is when the crack shape changes from long and shallow to half circular, i.e., λ increases to above 0.8. In the present investigation, this change occurred from about half surface crack lengths a 220 μm to a = 500 μm. The former is roughly estimated from specimen #302, while the latter is an upper limit from specimen #1. These values match Newman's results for the closure analysis in Figure 2.10 [90], where the free surface effect decayed in about 450 μm, with a tendency to decay faster for a smaller applied stress level.

The prolonged free surface effect after the plastic crack propagation threshold may well cause the different slopes of the crack propagation curves in Region II. Note that at the plastic crack propagation threshold, λ of Specimen #1, determined from the ripple lines on fractographic surfaces, is about 0.44, while it is about 0.84 in #302. Therefore, after the fatal crack in specimen #1 entered Stage II propagation, under a still strong free surface effect, it propagated faster than it should have. The closer to the threshold, the faster it propagated. Since the free surface effect decay is not completed until almost the transition from Region *II* to the fast propagation Region *III*, the whole Region *II* crack propagation curve is affected and appeared as having a flatter slope than other samples.

Microscopic Observation of Fractographic Crack Initiation Characteristics

Figure 5.22 (b) is a detailed photograph of the initiation site in specimen #1 which depicts an intergranular crack initiation site and Stage I crack propagation path. As can be seen, no striations are found at the site and cracking is clean cleavage along grain boundaries or slip band planes, instead of only on the so-called "well-defined crystallographic plane". Steps that formed when microcracks coalesced by crossing planes are well defined.

Despite the damage at the initiation site, "step marks" within isolated grains in the initiation region of specimen #302 are recognized from Figure 5.24 (b), supporting the analysis of the Stage I crack propagation path proposed in Chapter 3. "Step marks" are not found at the edges but always deeper in the crack, suggesting that the crack initiation and Stage I propagation at surfaces are along favourable main slip systems (crystallographic planes).

Summary

Some important figures and commands in the mechanism study are summarized in Table 5.4.

Category	Low cycle fatigue (specimen #1, #2, and #302)	High cycle fatigue (specimen #302)
Crack initiation site	grain boundary	slip band
Percentage of crack initiation in total life	$\sim 3.0\%$	$\sim 0.4\%$
Percentage of sub-microcrack initiation in total life	#1 and #301, 20% #2, 40%	70%
Surface topograph	grain protuberances and indentions	smoother overall surface
Slip lines	extensive plus secondary slip lines	extensive
Extrusions and (or) intrusions	both; flower-like extrusions	both
Crack aspect ratio, λ	~ 0.35 and up	~ 0.8
Half crack length at which λ becomes greater than 0.8	$< 500\ \mu m$	$\sim 220\ \mu m$

Table 5.4: Summary of Characteristics of Low and High Cycle Fatigue.

Chapter 6

CONCLUSIONS AND STATEMENT OF ORIGINALITY

6.1 Conclusions

The findings of this research effort are best detailed as follows.

1. A mechanical model of fatigue crack initiation and early propagation based on a plastic strain intensity factor, ΔK_p, has been proposed and substantiated. In this model, the crack initiation region, Region I_p, is simplified as a straight line with a different slope on the log-log scale of the da/dN versus ΔK_p curve. The transition point from Region I_p to the crack propagation region, Region II, is defined by the plastic crack propagation threshold, ΔK_{pth} and the initial engineering crack size, a_0, has been defined as the crack size at ΔK_{pth}.

2. It has been experimentally confirmed that a fatal crack experiences two thresholds in its propagation process, namely, the sub-threshold and the plastic crack

propagation threshold, ΔK_{pth}. Both are in the initiation region, Region I_p. The sub-regions in the initiation region before the sub-threshold are defined as the sub-microcrack initiation and propagation region, Region I_i, and the sub-region in the initiation region between the sub-threshold and the ΔK_{pth} is defined as the microcrack propagation region. Both thresholds are controlled by the ΔJ-integral level. The energy crack propagation threshold, $\sqrt{\Delta J \cdot E}_{pth}$, is a material constant which controls all other forms of the plastic crack propagation threshold.

3. Substantial evidence has been obtained to indicate that crack initiation mechanisms are mainly surface deterioration resulting from free irreversible dislocations sliding on favourable slip planes (in high cycle fatigue) and weakest link opening at grain boundaries (in low cycle fatigue). The driving force for crack initiation is the maximum shear strain.

4. Crack propagation in the initiation region takes the form of Stage I propagation. The model of Stage I sub-microcrack nucleation in Region I_i and the model of Stage I microcrack propagation in Region I_{ii} proposed have been shown to warrant serious consideration. Stage I sub-microcrack propagation is two-dimensional and mainly along a line, while Stage I microcrack propagation is three-dimensional and along a cone surface at 45° to the applied load. Stage I microcrack propagation produces semi-elliptical shaped cracks.

5. The proposed models were successfully verified by experimental results. Under the proposed mechanical model, the crack initiation life can be quantitatively predicted by integration. The comparison of fatigue crack initiation life predicted by the mechanical model and from experiments indicated an error of

less than 5%. The total crack initiation lives ranged from 70% to 87% in the sequence of increasing total fatigue life. For the material under discussion, the ΔJ value for the sub-threshold is 1.8 MPa$\sqrt{m}$, and $\sqrt{\Delta J \cdot E_{pth}}$, the energy crack propagation threshold is 7.3 MPa$\sqrt{m}$. The initial engineering crack size, a_0, determined at the $\sqrt{\Delta J \cdot E_{pth}}$ value, ranges from 59 μm to 247 μm. The qualitative and quantitative studies of replicas and the fractographic surface support the Stage I propagation models and provide solid physical foundations for the mechanical model of fatigue crack initiation and early propagation proposed.

6. The studies of crack profile changes in this investigation indicated that the free surface effect carries into the crack propagation region, Region *II*. Complete free surface effect decay takes place between half crack lengths of 220 to 500 μm for the material and strain levels investigated.

On the basis of these findings future research efforts will be concentrated on: 1) extending the formula for ΔJ-integral estimation to surface cracks in limited bodies, 2) testing more specimens under both low and high cycle fatigue conditions in order to learn more about the sub-microcrack nucleation mechanism, 3) testing a wider range of specimens with different material properties to improve the accuracy of the material strength factor, 4) testing samples of different sizes for different materials under different environments to determine other factors in the model, and 5) continuing the investigation of the free surface effect.

6.2 Statement of Originality

1. A new driving force, the plastic strain intensity factor ΔK_p, has been substantiated for crack initiation and propagation research.
2. A quantitative model of crack initiation and early propagation based on ΔK_p has been proposed and successfully verified by experiments.
3. A plastic crack propagation threshold, ΔK_{pth}, has been defined as the transition from crack initiation to propagation whose value was shown to occur at $\sqrt{\Delta J \cdot E}_{pth}$. The initial engineering crack size, a_0, has been defined as the crack size at the plastic crack propagation threshold.
4. A systematic model of Stage I crack propagation in smooth cylindrical specimens has been proposed and experimentally substantiated.
5. The features of crack initiation and stage I propagation sites on fractographic surfaces have been documented.
6. The relation of the crack propagation threshold and the similitude condition violations between short and long cracks, such as the closure effect, has been analysed for short crack lengths within the initiation region.

References

[1] ASTM Standard E647-86 "Standard Test Method for Constant Load Amplitude Fatigue Crack Growth Rates above 10^{-8}m/cycle", **Annual Book of ASTM Standards**, Vol. 03.01, (1986), pp. 714-736.

[2] Paris, P.C., and Erdogan, F., "A Critical Analysis of Crack Propagation Laws", **J. Basic Engrg.**, Vol. 88, (1963), pp. 528-535.

[3] Buck, O., Morris, W.L. and James, M.R., "Remaining Life Prediction in the Microcrack Initiation Regime," in **Fracture and Failure: Analyses, Mechanisms and Applications**, P.P. Tung *et al* Eds., American Society for Metals, (1981), pp. 55-64.

[4] Field, J.L., Behnaz, F, and Pangborn, R.N., "Characterization of Microplasticity Developed During Fatigue," in **Fatigue Mechanisms: Advances in Quantitative Measurement of Physical Damage**, ASTM STP 811, American Society for Testing and Materials, (1983), pp. 71-94.

[5] Lukáš, P. and Kunz, L., "Mechanisns of Near-Threshold Fatigue Crack Propagation and High Cycle Fatigue in Copper", **Acta Technica ČSAV**, No. 4, (1986), pp. 460-488.

[6] Müllner, H. Weiss, B. and Stickler, R., "The Effect of Microstructure on the Fatigue Threshold in Copper", **Fatigue Thresholds**, the Proceedings of an International Conference held in Stockholm, June 1-3, Vol. I, (1981), pp. 423-441.

[7] Guerra Rosa, L., Branco, C.M. and Radon, J.C., "Prediction of Threshold and Ultra-Low Fatigue Crack Growth Rates", **Int. J. Fatigue**, No. 4, Oct. (1985), pp. 183-190.

[8] Radon, J.C., "Fatigue Crack Growth in the Threshold Region", **Fatigue Thresholds**, the Proceedings of an International Conference held in Stockholm, June 1-3, Vol. I, (1981), pp. 113-133.

[9] Ūsami, S., "Application of Threshold Cyclic-Plastic- Zone-Size Criterion to Some Fatigue Limit Problems", **Fatigue Thresholds**, the Proceedings of an International Conference held in Stockholm, June 1-3, Vol. I, (1981), pp. 205-239.

[10] ASTM Standard E466-82 "Standard Practice for Conducting Constant Amplitude Axial Fatigue Tests of Metallic Materials", **Annual Book of ASTM Standards**, Vol. 03.01, (1986), pp. 571-576.

[11] ASTM Standard E606-80 "Standard Recommanded Practice for Constant Amplitude Practice for Constant Amplitude Low Cycle Fatigue Testing", **Annual Book of ASTM Standards**, Vol. 03.01, (1986), pp. 656-673.

[12] Leis, B.N., Hopper, A. T. Ahmad, J., Broek, D. and Kanninen, M.F., "Critical Review of the Fatigue Growth of Short Cracks", **Engineering Fracture Mechanics**, Vol. 23, No. 5, (1986), pp. 883-898.

[13] Schijve, J., "Significance of Fatigue Cracks in Micro-Range and Macro-Range", in **Fatigue Crack Propagation**, ASTM STP 415, American Society for Testing and Materials, (1967), pp. 415-457.

[14] Tanaka, K. Hojo, M., and Nakai, Y., "Fatigue Crack Initiation and Early Propagation in 3% Silicon Iron", in **Fatigue Mechanisms: Advances in Quantitative Measurement of Physical Damage**, ASTM STP 811, J. Landford, D.L. Davidson, W.L. Morris, and R.P. Wei, Eds., American Society for Testing and Materials, (1983), pp. 207-232.

[15] Pearson, S., "Initiation of Fatigue Cracks in Commercial Aluminum Alloys and the Subsequent Propagation of Very Short Cracks", **Engineering Fracture Mechanics**, Vol. 7, No. 2, (1975), pp. 235-247.

[16] Provan. J.W., and Zhai, Z.H., "A Review of Fatigue Crack Initiation", in **Time Dependent Fracture**, A. Krausz, Ed., Martinus Nijhoff, (1984), pp. 201-212.

[17] Provan. J.W., and Zhai, Z.H., "Short Crack Initiation and Propagation on Smooth Surfaces — Modelling and Experimentation", Paper presented at **Symposium on Surface-Crack Growth: Models, Experiments, and Structures**, ASTM, April 25, Sparks, Navada, U.S.A., (1988).

[18] Provan, J.W., "The Micromechanics of Fatigue Crack Initiation", in **Modelling Problems in Crack Tip Mechanics**, J.T. Pindera, Ed., Martinus Nijhoff, (1984), pp. 131-154.

[19] Wadsworth, N.J., "Work Hardening of Copper Crystals under Cyclic Straining", **Acta Metall.**, Vol. 11, (1963), pp. 663-673.

[20] Basinski, S.J., Basinski, Z.S. and Howie, A., "Early States of Fatigue in Copper Single Crystals", **Philosophical Magazine**, Vol. 19, (1969), pp. 899-924.

[21] Starke, E.A., Jr., "Cyclic Plastic Deformation and Microstructure", in **Fatigue and Microstructure**: Papers presented at the 1978 ASM Materials Science Seminar, 14-15 Oct., St. Louis, Missouri, (1978), pp. 205-235.

[22] Ho, N.J., Chen, C.M. and Tjong, S.C., "Cyclic Softening of Age Hardened FE-MN-AL-C Alloys Containing Coherent Precipitates", **Scrip. Metall.**, Vol. 21, (1987), PP. 1319-1322.

[23] Finney, J.M., "Strain Localization in Cyclic Deformation", Ph.D. Thesis, Univ. of Pennsylvania, (1974).

[24] Polak, M.K. and Lakas, P., "On the Cyclic Stress-Strain Curve Evaluation in Low Cycle Fatigue", **Mater. Sci. Engr.**, Vol. 28, (1977), pp. 109-117.

[25] Neumann, P., "Strain Bursts and Coarse Slip During Cyclic Deformation", **Z. Metallkd.**, Vol. 59, (1968), pp. 927-934.

[26] Alden, T.H. and Bachofen, W.A., "The Formation of Fatigue Cracks in Aluminum Single Crystals", **Acta Metall.**, Vol. 9, (1961), pp. 352-366.

[27] Mughrabi, H., "The Cyclic Hardening and Saturation Behaviour of Copper Single Crystals", **Mater. Sci. Eng.**, Vol. 33, (1978), pp. 207-223.

[28] Laird, C., "Mechanisms and Theories of Fatigue", in **Fatigue and Microstructure, Material Science Seminar**, St. Louis, 1978, American Society for Metals, (1979), pp. 149-203.

[29] Kuokkala, V. T., and Kettunen, P., "Cyclic Stress-Strain Response of Polycrystalline Copper in Constant and Variable Amplitude Fatigue", **Acta Metall.**, Vol. 33, No. 11, (1985), pp. 2041-2047.

[30] Kemsley, D.S., "Crack Paths in Fatigued Copper", **J. Inst. Metals.**, Vol. 185, (1957), pp. 420-421.

[31] Kim, W.H. and Laird, C., "Crack Nucleation and Stage I Propagation in High Strain Fatigue, I", **Acta Metall.**, Vol. 26, (1978), pp. 777-787.

[32] Kim, W.H. and Laird, C., "Crack Nucleation and Stage I Propagation in High Strain Fatigue, II", **Acta Metall.**, Vol. 26, (1978), pp. 789-799.

[33] Thompson, N., Wadsworth, N. and Louat, N., "The Origin of Fatigue Fracture in Copper", **Phil. Mag.**, Vol. 1, (1956), pp. 113-126.

[34] Awatani, J., Katagiri, K., Omura, A. and Shiraishi, T., "A Study of the Fatigue Limit of Copper", **Metallurgical Transactions A**, Vol. 6, (1975), pp. 1029-1034.

[35] Hessler. W., Mullner, H., Weiss, B. and Stickler, R., "Near-Threshold Behaviour of Polycrystalline Copper", **Metal Science**, Vol.15, (1981), pp. 225-230.

[36] Pohl, K., Mayr, P. and Macherauch, E., "Shape and Structure of Persistent Slip Bands in Iron Carbon Alloys", in **Defects, Fracture and Fatigue**, eds., G.C. Sih and J.W. Provan, Martinus Nijhoff Publishers, The Hague, (1983), pp. 147-159.

[37] Mughrabi, H., Ackermann, F. and Herz, K., "Persistent Slip Bands in Fatigued Face-Centered and Body-Centered Cubic Metals", in **Fatigue Mechanisms**, ed., J.T. Fong, ASTM STP 675, American Society for Testing and Materials, (1979), pp. 69-105.

[38] Mughrabi, H. and Wang, R., "Cyclic Strain Localization and Fatigue Crack Initiation in Persistent Slip Bands in Face-Centered Cubic Metal and Single-Phase Alloys", in **Defects and Fracture**, eds., G.C. Sih and H. Zorski, Martinus Nijhoff Publishers, The Hague, (1982), pp. 15-28.

[39] Kuhlmann-Wilsdorf, D. and Laird, C., "Dislocation Behavior in Fatigue", **Mat. Sci. Eng.**, Vol. 27, (1977), pp. 137- 156.

[40] Finney, J.M. and Laird, C., "Strain Localization in Cyclic Deformation of Copper Single Crystals", **Phil. Mag.**, Vol. 31, 8th Series, (1975), pp. 339-366.

[41] Woods, P.J., "Low-Amplitude Fatigue of Copper and Copper-5 at.% Aluminum Single Crystals", **Phil. Mag.**, Vol. 28, No. 1, (1973), pp. 155-191.

[42] Antonopoulos, J.G. and Winter, A.T., "Weak-Beam Study of Dislocation Structures in Fatigued Copper", **Phil. Mag.**, Vol, 33, (1976), pp. 87-95.

[43] Neumann, P., "Coarse Slip Model of Fatigue", **Acta Metall.**, Vol. 17, (1969), pp. 1219-1225.

[44] Kuhlmann-Wilsdorf, D. and Laird, C., "Dislocation Behaviour in Fatigue V: Breakdown of Loop Patches and Formation of Persistent Slip Bands and of Dislocation Cells". **Mat. Sci. Eng.**, Vol. 46, (1980), pp. 209-219.

[45] Winter, A.T., "Nucleation of Persistent Slip Bands in Cyclically Deformed Copper Crystals", **Phil. Mag.**, Vol. 37, (1978), pp. 457-463.

[46] Forsyth, P.J.E., "Exudation of Material from Slip Bands at the Surface of Fatigued Crystals of an Aluminium-Copper Alloy", **Nature**, Vol. 171, (1953), pp. 172-173.

[47] Cottrell, A.H. and Hull, D., "Extrusion and Intrusion by Cyclic Slip in Copper", **Proc. Roy. Soc. A**, Vol. 242, (1957), pp. 211-213.

[48] Forsyth, P.J.E., "Slip-Band Damage and Extrusion", **Proc. Roy. Soc. A**, Vol. 242, (1957), pp. 198-202.

[49] Mughrabi, H., Wang, R., Differt, K., and Essmann, U., "Fatigue Crack Initiation by Cyclic Slip Irreversibilities in High-Cycle Fatigue," in **Fatigue Mechanisms: Advances in Quantitative Measurement of Physical Damage**, ASTM STP 811, J. Landford, D.L. Davidson, W.L. Morris, and R.P. Wei, Eds., American Society for Testing and Materials, (1983), pp. 5-45.

[50] Essmann, U., Goesele, U. and Mughrabi, H., "A Model of Extrusion and Intrusion in Fatigued Metals, Part 1", **Phil. Mag., A.** Vol. 44, (1981), pp. 405-426.

[51] Margolin, H., Mahajan, Y. and Saleh, Y., "Grain Boundaries, Stress Gradients and Fatigue Crack Initiation". **Scripta Met.**, Vol. 10, (1976), pp. 1115-1118.

[52] Essmann, U., "Irreversibility of Cyclic Slip in Persistent Slip Bands of Fatigued Pure F.C.C. Metals", **Phil. Mag. A**, Vol. 45, (1982), pp. 171-190.

[53] Rémy, L., "Cyclic Deformation and Crack Initiation Processes," in **Fatigue,** Conference Proceedings, Papers Presented at the 2nd International Conference on Fatigue and Fatigue Thresholds, 3-7 Sept., Vol. 1, (1984), pp. 15-33.

[54] Laird, C., "The Fatigue Limits of Metals", **Material Science and Engineering,** Vol. 22, (1976), pp. 231-236.

[55] Forsyth, P.J.E., "A Two Stage Process of Fatigue Crack Growth", **Proc. Symp. Crack Propagation,** Cranfield, England, (1961), pp. 76-94.

[56] Revised by Antolovich, S.D. and Saxena, A., "Fatigue Failures", **Failure Analysis and Prevention,** Metals Handbook, 9th Edition, Vol. 11, American Society for Metals, (1986), pp. 102-135.

[57] Li, C.S., "Shear Deformation at Stage I Short Crack Tip", **Scripta Metall.,** Vol. 22, (1988), pp. 163-166.

[58] Cheng A.S. and Laird, C., "The Transition from Stage I to Stage II Fatigue Crack Propagation in Copper Single Crystals Cycled at Constant Strain Amplitudes", **Mat. Sci. Eng.,** Vol. 60, (1983), pp. 177-183.

[59] Tanaka, K, Akiniwa, Y., Nakai, Y. and Wei, R.P., "Modelling of Small Fatigue Crack Growth Interacting with Grain Boundary", **Engineering Fracture Mechanics,** Vol. 24, No. 6, (1986), pp. 803-819.

[60] Gerdes, C., Gysler, A. and Lütjering, G., "Propagation of Small Surface Cracks in Ti-Alloys", **Fatigue Crack Growth Threshold Concepts,** AIME, D. Davidson and S. Suresh Eds., (1984), pp. 465-478.

[61] Reemsnyder, H.S., "Constant Amplitude Fatigue Life Assessment Models", **SAE Paper**, No. 820688, (1982), pp. 121-132.

[62] Mattos, R.J. and Lawrence, F.V., "Estimation of the Fatigue Crack Initiation Life in Welds Using Low Cycle Fatigue Concepts", **SAE SP**, No. 424, (1977).

[63] Lawrence, F.V. Jr., Mattos, R.J., Higashhida Y. and Burk, J.D., "Estimating the Fatigue Crack Initiation Life of Welds." in **Fatigue Testing of Weldments**, ASTM STP 648, (1978), pp. 134-158.

[64] Schijve, J., "Significance of Fatigue Cracks in Micro-Range and Macro-Range," **Fatigue Crack Propagation**, ASTM STP 415, Am. Soc. Testing Mats., (1967), pp. 415-453.

[65] Maiya, P.S., "Consideration of Crack Initiation and Crack Propagation in Low-Cycle Fatigue", **Scripta Metallurgica**, Vol. 9, (1975), pp. 1141-1146.

[66] Maiya, P.S., "Observations of Crack Initiation in Low-Cycle Fatigue Specimens of Type 304 Stainless Steel", **Scripta Metallurgica**, Vol 11, (1977), pp. 331-334.

[67] Boardman, B.E., "Crack Initiation Fatigue – Data, Analysis, Trends and Estimation", **SAE Paper**, No. 820682, Society of Automotive Engineers, Warren, PA, (1982), pp. 59-73.

[68] in't Veld Huis, A.J. and De Hosson, J.Th.M., "Crack Initiation in a Ni-Base Superalloy", **Scripta Metall.**, Vol. 21, (1987), pp. 1481-1486.

[69] Coffin, L.F., "Notch Fatigue Crack Initiation Studies in a High Strength Nickel Base Superalloy", **Eng. Frac. Mech.**, Vol 28, (1987), pp. 485-503.

[70] Hoshide, T. and Socie, D.F., "Crack Nucleation and growth Modeling in Biaxial Fatigue", **Eng. Frac. Mech.**, Vol. 29, No. 3, (1988), pp. 287-299.

[71] Jolles, M. and Tortoriello, V., "Grometry Variations During Fatigue Growth of Surface Flaws", **Fracture Mechanics: Fourteenth Symposium—Volume I: Theory and Analysis**, ASTM STP 791, J.C. Lewis and G. Slines, Eds., American Society for Testing and Materials, (1983), pp. I-297–I-307.

[72] Wu, S.X., "Shape Change of Surface Crack During Fatigue Growth", **Engng. Frac. Mech.**, Vol. 22, No. 5, (1985), pp. 897-913.

[73] Hoshide, T., Yamada, T., Fujimura, S., and Hayashi, T., "Short Crack Growth and Life Prediction in Low-Cycle Fatigue of Smooth Specimens", **Engng. Frac. Mech.**, Vol. 21, No. 1, (1985), pp. 85-101.

[74] Lankford, J., Cook, T.S., and Sheldon, G.P., "Fatigue Microcrack Growth in a Nickel-Base Superalloy", **Int. J. Frac.**, Vol. 17, No. 2, (1981), pp. 143-155.

[75] Taylor, D. and Knott, J.F., "Fatigue and Propagation Behaviour of Short Cracks; The Effect of Microstructure", **Fatigue of Engng Mater. and Structures**, Vol.4, (1981), pp. 147-155.

[76] Leis, B.N., "Microcrack Initiation and Growth in a Pearlitic Steel–Experiments and Analysis", **Fracture Mechanics**: Fifteenth Symposium, ASTM STP 833, R.J. Sanford Ed., American Society for Testing and Materials, (1984), pp. 449-480.

[77] Leis B.N. and Forte T.P., "Fatigue growth of initially physically short cracks in notched aluminum and steel plates", **Fracture Mechanics**, 13th confer-

ence, ASTM STP 743, Lane and Otten Eds., American Society for Testing and Materials, (1981), pp. 100-124.

[78] Morris, W.L., "The Noncontinuum Crack Tip Deformation Behaviour of Surface Microcracks", **Metall. Trans.**, Vol. 11A, No. 7, (1980), pp. 1117-1123.

[79] Smith, R.A., "Short Fatigue Cracks", in **Fatigue Mechanisms: Advances in Quantitative Measurement of Physical Damage**, ASTM STP 811, J. Landford, D.L. Davidson, W.L. Morris, and R.P. Wei, Eds., American Society for Testing and Materials, (1983), pp. 264- 279.

[80] Suresh, S. and Ritchie, R. O., "Mechanics and Physics of the Growth of Small Cracks", in **Behavior of Short Cracks in Airframe Components**, AGARD Conference Proceeding No. 328, (1983), pp. 1.1 - 1.14.

[81] Suresh, S. and Ritchie, R. O., "Propagation of Short Fatigue Cracks", **International Metals Reviews**, Vol. 29, No. 6, (1984), pp. 445-476.

[82] Elber, W., "The Significance of Fatigue Crack Closure", in **Damage tolerance on aircraft structures**, STP 496, Philadelphia, Pa, American Society for Testing and Materials, (1971), pp. 230-242.

[83] Suresh, S., Zamiski, G.F. and Ritchie, R.O., "Oxide-Induced Crack Closure", **Metall. Trans. A**, Vol. 12A, (1981), pp. 1435-1443.

[84] Suresh, S. and Ritchie, R.O., "A Geometric Model for Fatigue Crack Closure Induced by Fracture Surface Roughness", **Metall. Trans. A**, Vol. 13A, (1982), pp. 1627-1631.

[85] Minakawa, K. and McEvily, A.J., "On Crack Closure in the Near-Threshold Regime", **Scripta Metallurgica.**, Vol. 15, (1981), pp. 633-636.

[86] Frandsen, J.D., Inman, R.V., and Buck, O., "A Comparison of Acoustic and Strain Gauge Techniques for Crack Closure", **Inter. J. Frac.**, Vol. 11, No. 2, (1975), pp. 345-348.

[87] Ohta, A., Kosuge, M. and Sasaki, E., "Fatigue Crack Closure Over the Range of Stress Ratios from −1 to 0.8 Down to Stress Intensity Factor Threshold Level in HT80 Steel and SUS 304 Stainless Steel", **Inter. J. Frac.**, Vol. 14, No. 3, (1978), pp. 251-264.

[88] Minakawa, K. and McEvily, A.J., "On Near-Threshold Fatigue Crack Growth in Steels and Aluminum Alloys", in **Fatigue Thresholds: Fundamentals and Engineering Applications**, J. Backlund, A.F. Blom and C.J. Beevers, Eds., EMAS, U.K., (1982), pp. 373-390.

[89] Ohta, A., Kosurge, M. and Sasaki, E., "A Method for Determining the Stress Intensity Threshold Level for Fatigue Crack Propagation", **Engineering Fracture Mechanics**, Vol. 9, No. 3, (1977), pp. 655-662.

[90] Newman, J.C. Jr., "A Nonlinear Fracture Mechanics Approach to the Growth of Small Cracks", in **Behavior of Short Cracks in Airframe Components**, AGARD Conference Proceeding No. 328, 1983, pp. 6.1 - 6.26.

[91] Rice, J.R., "A Path Independent Integral and the Approximate Analysis of Strain Concentration by Notches and Cracks", **J. Appl. Mech.**, Trans. ASME, Vol. 35, (1968), pp. 379-386.

[92] Dowling, N.E., "Crack Growth During Low Cycle Fatigue of Smooth Axial Specimens", in **Cyclic Stress-Strain and Plastic Deformation Aspects of Fatigue Crack Growth**, ASTM STP 637, American Society for Testing and Materials, (1977), pp. 97-121.

[93] El Haddad, M.H. Smith, K.N. and Topper, T.H., "Fatigue Crack Propagation of Short Cracks", **Journal of Engineering Materials and Technology**, Transactions ASME Series H, Vol. 101, (1979), pp. 42-46.

[94] El Haddad, M.H., Dowling, N.E., Topper, T.H. and Smith, K.N., "J-Integral Applications for Short Cracks at Notches", **International Journal of Fracture**, Vol. 16, No. 1, (1980), pp. 15-30.

[95] Lankford, J., Davidson, D.L. and Chan, K.S., "The Influence of Crack Tip Plasticity in the Growth of Small Fatigue Cracks", **Metallurgical Transactions A**, Vol. 15A, (1984), pp. 1579-1588.

[96] McEvily, A.J., "On the Quantitative Analysis of Fatigue Crack Propagation," in **Fatigue Mechanisms: Advancement in Quantitative Measurement of Physical Damage**, J. Lankford, D.L. Davidson, W.L., Morris, and R.P. Wei, Eds., ASTM STP 811, American Society for Testing and Materials, (1983), pp. 283-312.

[97] Hayashi, K. and Abe, H., "Stress Intensity Factors for a Semi-Elliptical Crack in the Surface of a Semi-Infinite Solid", **International Journal of Fracture**, Vol. 16, No. 3, (1980), pp. 275-285.

[98] Isida, M., Noguchi, H., and Yoshida, T., "Tension and Bending of Finite Thickness Plates with a Semi-Elliptical Surface Crack", **International Journal of**

Fracture, Vol. 26, (1984), pp. 157-188.

[99] Achard, L., "Procedure for Strain controlled Fatigue Tests of Smooth Specimens", **D.E.W. Report**, No. 1296-11, (1983).

[100] "Heat Treating of Copper Alloys", in **Heat Treating**, Metals Handbook, Ninth Edi., Vol. 4, American Society for Metals, (1981), pp. 719.

[101] Hartranft, R.T., and Sih, G.C., "Alternating Method Applied to Edge and Surface Crack Problems," in **Mechanics of Fracture 1: Methods of Analysis of Crack Problems**, G.C. Sih, Ed., Noordhoff, (1973), pp. 179-238.

[102] Usami, S., "Applications of Threshold Cyclic-Plastic-Zone-Size Criterion to Some Fatigue Limit Problems", in **Fatigue Thresholds**, Proceedings of the First International Conference on Fatigue Thresholds, Vol. 2, J. Backland, Ed., EMAS, (1981), pp. 205-238.

[103] Pandher, I.S., "Threshold and the Initial Stages of Fatigue Crack Propagation", **Master B Project**, McGill University, Montreal, Canada, (1986).

[104] Mowbray, D.F., "Derivation of a Low-Cycle Fatigue Relationship Employing the J-Integral Approach to Crack Growth", **Cracks and Fracture**, ASTM STP 601, American Society for Testing and Materials, (1976), pp. 33-46.

[105] Mbanugo, Chinwendu.C.Ike., "Stochastic Fatigue Crack Growth—An Experimental Study", **Ph.D. Thesis**, McGill University, (1979).

[106] Hunsche, A. and Neumann, P., "Quantitative Measurement of Persistent Slip Band Profiles and Crack Initiation", **Acta Metall.**, Vol. 34, No. 2, (1986), pp. 207-217.

Appendix A

CATMP PROGRAM

```
CATMP      MTS BASIC V01B-02C

5 REM        -*- CONSTANT AMPLITUDE COMPLETELY REVERSED -*-
10 REM       -*- PLASTIC STRAIN CONTROLLED FATIGUE TEST -*-
20 DIM N(100),X(100),Y(100),X0(75),Y0(75)
25 DIM X5(75),Y5(75),X7(75),Y7(75)
30 DIM N1(75),X8(75),Y8(75),P(100),X2(20),Y2(20),N3(20)
35 DIM F8(75),B(3)
37 MSW1(0)\TIME(20)\EDMP
40 FG1(0)\QUIT\MSW1(1)\FG1(0)\U0=1
45 X$='STRAIN'\Y$='STRESS'\N$='CYCLES'
50 I9=1\C6=0\X1=0
55 C(0)=100\C(1)=50\C(2)=20\C(3)=10
60 C(4)=10\C(5)=5\C(6)=2\C(7)=1
200 GOSUB 2000
300 GOSUB 3000
400 GOSUB 5000
500 QUIT\B=-1\CNTR(4)\GOSUB 8000
600 REM    GOSUB 15000
700 GOSUB 12000
800 GOSUB 16000
900 CNTR(3)\STOP
1000 END
1900 REM       -*- INPUT OF TEST PARAMETERS -*-
2000 CNTR(3)\PRINT \PRINT 'INPUT STRAIN TRANSDUCER AMPLITUDE ';\INPUT S1
2005 PRINT \PRINT 'INPUT LOAD TRANSDUCER AMPLITUDE (N) ';\INPUT L1
2010 PRINT \PRINT 'INPUT SPECIMEN DIAMETER (MM) ';\INPUT D1
2015 A1=(3.1416*D1^2)/4
2020 PRINT \PRINT 'INPUT FREQUENCY (HZ)';\INPUT R1
2035 PRINT \PRINT 'INPUT PLASTIC STRAIN LIMIT ';\INPUT S2
2040 PRINT \PRINT 'INPUT STRESS SCALE (MPA) ';\INPUT L2
2042 PRINT \PRINT 'INPUT STRAIN SCALE ';\INPUT S3
2045 PRINT \PRINT 'INPUT YIELD STRENGTH (MPA) ';\INPUT Y1
2046 PRINT \PRINT 'INPUT ELASTIC MODULUS (MPA) ';\INPUT E0
2050 Y1=Y1*.666*2047*A1/L1\R4=Y1/25
2055 PRINT \PRINT 'INPUT MATERIAL ';\INPUT M$
2060 PRINT \PRINT 'INPUT SPECIMEN # ';\INPUT S$
2065 PRINT \PRINT 'INPUT DATE ';\INPUT D$
2070 PRINT \PRINT 'INPUT YOUR INITIALS ';\INPUT I$
2071 PRINT \PRINT 'INPUT NUMBER OF CYCLES TO STOP(S7) ';\INPUT S7
2075 B(1)=R1\R2=B(1)\R3=.1\R5=1.00000E-03
2080 IF R3>=R2 THEN R3=R2
```

```
2085 FOR I=0 TO 7\IF C(I)<=R2 THEN 2090\NEXT I\I=8
2090 N5=I-1
2095 R2=R2*4095/C(N5)\R3=R3*4095/C(N5)\R5=R5*4095/C(N5)
2100 R6=S2*2047/S1\B(2)=2.00000E-03*2047/S1\B(3)=0
2105 CNTR(4)\GOSUB 8000\RETURN
2900 REM        -*- SET UP GRAPHICS & LABEL TEST SHEET -*-
3000 CNTR(3)
3030 PHYL(100,900,55,560)
3035 SCAL(0,-S3,S3,-L2,L2)\LABL(X$,Y$,S3/2,L2/2,0)
3040 CNTR(2)
3045 SCAL(0,-S3*2047/S1,S3*2047/S1,-L2*2047*A1/L1,L2*2047*A1/L1)
3048 CNTR(1)
3050 RETURN
3150 CNTR(5)\PRINT \PRINT TAB(15);'FATIGUE TEST OF SPECIMEN #';
3155 PRINT S$;' OF ';M$
3160 PRINT TAB(35);I$;TAB(45);D$
3165 PRINT \PRINT TAB(15);'FREQUENCY = ';R1;TAB(35);'PLASTIC STRAIN = ';S2
3170 IF E0>0 THEN 3175\PRINT \GO TO 3180
3175 PRINT TAB(15);'ELASTIC MODULUS = ';E0;' MPA'
3180 PRINT TAB(15);'***** STRESS IN MPA UNITS'
3185 IF B=-1 THEN 3190\PRINT TAB(15);'***** LOOPS RECORDED @ 0.1 HZ'
3190 PRINT \IF F$='Y' THEN 3230
3230 RETURN
3900 REM        -*- START DATA AQUISITION -*-
4000 CALL 'DACQ'(3,S,1,1,S)\CALL 'DACQ'(3,L,0,1,L)
4005 CALL 'DACQ'(1,X5,1,25)\CALL 'DACQ'(6,Y5,0,0)
4010 IF X1=1 THEN 4020
4015 X1=1\CALL 'DACQ'(2,Y0,0,R4)\CALL 'DACQ'(6,X0,1,0)
4020 STAR\RETURN
4900 REM        -*- REAL TIME CONTROL -*-
5000 PHYL(100,900,55,560)\CNTR(2)
5001 C2=16\C3=1\GOSUB 4000\IF E0>0 THEN 5006
5002 B(1)=INT(R3)\B=3\FG1(B,2,7,N5)
5003 PLOT(S,L)\S8=ABS(S)
5004 IF S8>=5.00000E-04*2047/S1 THEN 5005\GO TO 5003
5005 FG1(S8)\GOSUB 10000
5006 A8=L1/A1/E0/S1\B(1)=INT(R3)\B(2)=S3*2047/S1\B(3)=-B(2)
5007 B=3\FG1(B,2,7,N5)
5008 PLOT(S,L)\S8=ABS(S)\L8=ABS(L)\R7=S8-L8*A8
5009 IF R7>=R6 THEN 5010\GO TO 5008
5010 FG1(S8)\B(2)=S8\B(3)=-S8
5011 B(1)=INT(R3)\B=3\FG1(B,S7,7,N5)
5014 FOR I=1 TO 8
5020 PLOT(S,L)\LEF1(G1,G2,G3,G4)\IF G3=S7-I-1 THEN 5021\GO TO 5020
5021 R7=R6+(Y5(2*I-1)-Y5(2*I))*A8/2\B(2)=INT(R7)\B(3)=INT(-R7)
5023 NEXT I
5025 LEF1(G1,G2,G3,G4)\IF G3=S7-10 THEN 5030\GO TO 5025
5030 QUIT\FOR 1=1 TO 16\X(I)=X5(I)\Y(I)=Y5(I)\NEXT I\K1=K1+16
5035 B(1)=INT(R2)\GOSUB 7000
5040 LEF1(G1,G2,G3,G4)\N2=T5+S7+1-G3\IF N2>=C2-2 THEN 5060
5045 IF G3<=1 THEN  GOSUB 5500
5050 REM   IF N2>=150 THEN RETURN
5051 GOSUB 6000
5055 GO TO 5040
5060 QUIT\B(1)=INT(R3)\GOSUB 4000
5065 C3=C3+1
```

```
5085 PHYL(100,900,55,560)
5095 CNTR(2)
5100 LEF1(G1,G2,G3,G4)\N2=T5+S7+1-G3\IF N2>=C2 THEN 5110
5105 GO TO 5100
5110 PLOT(S,L)\LEF1(H1,H2,H3,H4)\IF H3<G3 THEN 5115\GO TO 5110
5115 LEF1(T1,T2,T3,T4)\IF T3<H3 THEN 5120\GO TO 5115
5120 QUIT\I1=1\FOR I=X5-2 TO X5-1\X(I1+K1)=X5(I)
5125 Y(I1+K1)=Y5(I)\I1=I1+1\NEXT I\K1=K1+2\N(C3)=T5+S7+1-G3
5130 CNTR(1)
5140 C2=C2*2\GO TO 5035
5145 RETURN
5400 REM        -*- RESTART FUNCTION GENERATION -*-
5500 QUIT\B=-1\CNTR(5)
5501 PRINT 'S7,R1,N5';\PRINT \INPUT S7,R1,N5
5502 R2=R1\R2=R2*4095/C(N5)\R3=.1*4095/C(N5)
5503 B(1)=INT(R2)\B=3\CNTR(2)
5505 FG1(B,S7,7,N5)\T5=N2
5506 GOSUB 7000
5510 LEF1(G1,G2,G3,G4)\IF G3<1 THEN 5520\GO TO 5510
5520 RETURN
5900 REM        -*- FAILURE CHECK -*-
6000 IF X7=Z9 THEN 6005\Q5=0\GO TO 6020
6005 IF L5=0 THEN 6020\IF N2<L5 THEN Q5=Q5+1
6010 IF Q5<40 THEN 6020\C4=C4+1\GOSUB 3150\CNTR(5)\FOR I=1 TO 8
6015 PRINT \NEXT I\PRINT TAB(15);'TEST STOPPED ON CYCLE';N2\GO TO 500
6020 Z7=X7\Z9=Z7\L5=N2\IF Z7<2 THEN RETURN
6025 Z1=Y7(Z7)\Z2=X7(Z7)\Z3=Y7(Z7-1)\Z4=X7(Z7-1)
6030 IF N2<12*2^C6 THEN 6045
6035 N1(2*C6)=N2\X8(2*C6)=Z2\X8(2*C6+1)=Z4
6040 Y8(2*C6)=Z1\Y8(2*C6+1)=Z3\C6=C6+1
6041 B(2)=INT(R6+ABS(Z1-Z3)*L1/A1/2/E0/S1)\B(3)=INT(-B(2))
6045 IF Z1<0 THEN 6055
6050 IF Z1<=(1-.1*I9)*Y(K1-1) THEN 6065\RETURN
6055 IF Z3 0 THEN RETURN
6060 IF Z3 =(1-.1*I9)*Y(K1-1) THEN 6065\RETURN
6065 B(1)=INT(R3)\QUIT\IF I9<1 THEN 6100
6075 GOSUB 3150\CNTR(4)\GOSUB 8000\CNTR(3)\F$='Y'\GOSUB 3150
6080 C2=10^9
6085 PHYL(250,750,0,500)\SCAL(0,-S3,S3,-L2,L2)
6090 LABL(X$,'STRESS MPA',S3/2,L2/2,0)\CNTR(2)
6095 LABL(S3/10,L2/10,3)
6096 SCAL(0,-S3*2047/S1,S3*2047/S1,-L2*2047*A1/L1,L2*2047*A1/L1)
6100 CNTR(2)\GOSUB 4000\LEF1(G1,G2,G3,G4)
6105 LEF1(H1,H2,H3,H4)\IF H3<G3 THEN 6110\GO TO 6105
6110 PLOT(S,L)\LEF1(T1,T2,T3,T4)\IF T3<H3 THEN 6115\GO TO 6110
6115 LEF1(H1,H2,H3,H4)\IF H3<T3 THEN 6120\GO TO 6115
6120 QUIT\N3(2*I9)=T5+S7+1-G3
6125 CNTR(1)
6130 X2(2*I9)=X5(X5-2)\X2(2*I9+1)=X5(X5-1)
6135 Y2(2*I9)=Y5(X5-2)\Y2(2*I9+1)=Y5(X5-1)
6140 COMM(' -',X2(2*I9),Y2(2*I9))\PRINT N3(2*I9)
6145 I9=I9+1\IF I9=5 THEN 500
6150 IF Y2(2*I9-2)<5 THEN 500
6155 B(1)=INT(R2)
6160 GOSUB 7000\RETURN
```

```
6900 REM        -*- DATA AQUISITION -*-
7000 CALL 'DACQ'(1,X7,1,50,X7)\CALL 'DACQ'(6,Y7,0,0,Y7)
7100 STAR\RETURN
7900 REM        -*- DELAY LOOP -*-
8000 FOR I=1 TO 1200\M4=SIN(I)\NEXT I\RETURN
9900 REM        -*- MODULUS CALCULATION -*-
10000 W1=0\W2=0\W3=0\W4=0\W6=0\J9=0
10005 A9=A9+1\IF A9>1 THEN 10030
10010 FOR I=1 TO 50\IF YO(I)>Y1 THEN 10025
10015 REM IF YO(I)<YO(I-1) THEN 10025
10020 NEXT I
10025 I3=I-1\I7=5
10030 FOR I=I7 TO I3\W1=W1+XO(I)^2\W2=W2+XO(I)
10035 W3=W3+XO(I)*YO(I)\W4=W4+YO(I)\J9=J9+1
10040 W6=W6+YO(I)^2
10045 NEXT I\EO=(J9*W3-W2*W4)/(J9*W1-W2^2)\EO=EO*L1/(A1*S1)
10050 E5=(J9*W3-W2*W4)/((J9*W1-W2^2)*(J9*W6-W4^2))^.5
10055 RETURN
11900 REM        -*- DATA REDUCTION -*-
12000 CNTR(3)\IF I9>2 THEN 12005
12005 V$='N'\T6=0
12010 F$='Y'
12015 IF R$='Y' THEN 12075
12020 R$='Y'\FOR I=1 TO 20
12025 Y2(I)=Y2(I)*L1/(A1*2047)\X2(I)=X2(I)*S1/2047
12030 NEXT I
12035 FOR I=1 TO K1
12040 X(I)=X(I)*S1/2047\Y(I)=Y(I)*L1/(A1*2047)
12045 P(I)=X(I)-Y(I)/EO
12050 NEXT I
12055 FOR I=0 TO 2*C6-1
12060 X8(I)=X8(I)*S1/2047\Y8(I)=Y8(I)*L1/(A1*2047)
12065 P8(I)=X8(I)-Y8(I)/EO
12070 NEXT I
12075 Q$=' O.1 HZ'
12080 GOSUB 3150
12085 PRINT TAB(15);'DATA TAKEN @';Q$
12090 PRINT
12095 PRINT '*************** AMPLITUDES ***************';
12100 PRINT '--******** MEANS ********'
12105 PRINT TAB(1);'CYC';TAB(8);'STRAIN';TAB(21);'STRESS';
12110 PRINT TAB(32);'PL. STRAIN';TAB(47);'STRAIN';TAB(60);'STRESS'
12115 IF V$='Y' THEN 12480
12120 IF T6=16 THEN 12155
12125 FOR I=1 TO 16 STEP 2
12130 PRINT TAB(1);(I+1)/2;TAB(5);(X(I)-X(I+1))/2;TAB(18);
12135 PRINT (Y(I)-Y(I+1))/2;TAB(29);(P(I)-P(I+1))/2;TAB(44);
12140 PRINT (X(I)+X(I+1))/2;TAB(57);(Y(I)+Y(I+1))/2
12145 NEXT I
12150 L9=2
12155 FOR I=17+T6 TO 31+T6 STEP 2\IF X(I+1)=0 THEN 12180
12160 PRINT N(L9);TAB(5);(X(I)-X(I+1))/2;TAB(18);
12165 PRINT (Y(I)-Y(I+1))/2;TAB(29);(P(I)-P(I+1))/2;TAB(44);
12170 PRINT (X(I)+X(I+1))/2;TAB(57);(Y(I)+Y(I+1))/2\L9=L9+1
```

```
12175 NEXT I\CNTR(4)\GOSUB 8000\CNTR(3)\T6=16\GO TO 12080
12180 IF I9=1 THEN 12215\IF T6=16 THEN 12190
12185 CNTR(4)\GOSUB 8000\CNTR(3)\GOSUB 3150
12190 PRINT \PRINT "***** FAILURE PEAKS : DATA TAKEN @ 0.1 HZ"
12195 PRINT TAB(1);"CYC";TAB(13);"*** STRESS ***";TAB(41);"*** STRAIN ***"
12200 FOR I=2 TO I9-1\PRINT N3(2*I);
12205 PRINT TAB(10);Y2(2*I);TAB(20);Y2(2*I+1);TAB(35);X2(2*I);
12210 PRINT TAB(50);X2(2*I+1)\NEXT I
12215 V$="Y"
12220 GOSUB 8000\CNTR(4)\GOSUB 8000
12225 GO TO 12475
12230 CNTR(3)\GOSUB 3150
12235 PRINT \PRINT TAB(20);"'*'- AMPLITUDES @ 0.1 HZ (LOOPS)"
12240 PRINT TAB(20);"'+'- AMPLITUDES @ THE SPECIFIED PL. STRAIN RATE"
12245 PRINT TAB(20);"'X'- TENSILE PEAKS (FAILURE)"
12250 PHYL(200,850,0,500)\SCAL(2,1,10^7,0,L2)
12255 LABL(N$,"STRESS MPA",10,L2/5,0)\LABL(1,L2/10,3)
12260 CNTR(2)\PLOT(1,L2)\PLOT(1,0)\CNTR(2)
12265 PLOT(10^7,L2)\PLOT(10^7,0)\CNTR(2)
12270 FOR I=1 TO 16 STEP 2
12275 MARK("*",(I+1)/2,(Y(I)-Y(I+1))/2)
12280 NEXT I
12285 L9=2
12290 FOR I=17 TO K1 STEP 2
12295 MARK("*",N(L9),(Y(I)-Y(I+1))/2)
12300 L9=L9+1\NEXT I
12305 CNTR(2)
12310 FOR I=0 TO C6-1
12315 PLOT(N1(I*2),ABS(Y8(2*I)-Y8(2*I+1))/2)
12320 MARK("+",N1(2*I),(Y8(2*I)-Y8(2*I+1))/2)
12325 NEXT I
12330 IF I9=4 THEN 12350
12335 FOR I=2 TO I9-1
12340 MARK("X",N3(2*I),Y2(2*I))
12345 NEXT I
12350 CNTR(4)\GOSUB 8000\CNTR(3)
12355 GOSUB 3150\PRINT
12360 PRINT TAB(20);"'*'- AMPLITUDES @ 0.1 HZ (LOOPS)"
12365 PRINT TAB(20);"'+'- AMPLITUDES @ SPECIFIED PL. STRAIN RATE"
12370 PHYL(200,850,0,500)\SCAL(3,1,10^7,1.00000E-05,.1)
12375 LABL(N$,"PL. STRAIN AMP.",10,10,0)\LABL(1,1,3)
12380 CNTR(2)
12385 PLOT(1,.1)\PLOT(1,1.00000E-05)\PLOT(10^7,1.00000E-05)
12390 PLOT(10^7,.1)\CNTR(2)
12395 FOR I=1 TO 16 STEP 2
12400 IF (P(I)-P(I+1))/2<1.00000E-05 THEN 12410
12405 MARK("*",(I+1)/2,(P(I)-P(I+1))/2)
12410 NEXT I
12415 L9=2
12420 FOR I=17 TO K1 STEP 2
12425 IF (P(I)-P(I+1))/2<1.00000E-05 THEN 12435
12430 MARK("*",N(L9),(P(I)-P(I+1))/2)
12435 L9=L9+1\NEXT I
12440 CNTR(2)\FOR I=0 TO C6-1
```

```
12445 IF ABS(P8(2*I)-P8(2*I+1))/2<1.00000E-05 THEN 12460
12450 PLOT(N1(2*I),ABS(P8(2*I)-P8(2*I+1))/2)
12455 MARK('+',N1(2*I),ABS(P8(2*I)-P8(2*I+1))/2)
12460 NEXT I
12465 GOSUB 8000\CNTR(4)\GOSUB 8000
12470 RETURN
12475 CNTR(3)\Q$=' THE SPECIFIED PL. STRAIN RATE'\GO TO 12080
12480 FOR I=0 TO C6-1
12485 PRINT N1(2*I);TAB(5);ABS(X8(2*I)-X8(2*I+1))/2;
12490 PRINT TAB(18);ABS(Y8(I*2)-Y8(I*2+1))/2;TAB(29);
12495 PRINT ABS(P8(2*I)-P8(2*I+1))/2;TAB(44);(X8(I*2)+X8(I*2+1))/2;
12500 PRINT TAB(57);(Y8(I*2)+Y8(I*2+1))/2
12505 NEXT I
12510 GOSUB 8000\CNTR(4)\GOSUB 8000
12515 GO TO 12230
14900 REM        -*- PLOT FOR MODULUS CALCULATION -*-
15000 CNTR(3)
15005 Z5=5
15010 PHYL(250,750,0,500)\SCAL(0,0,S1,0,L2)
15015 LABL(X$,Y$,S1/5,L2/5,0)\SCAL(0,0,2047,0,L2*2047*A1/L1)
15020 CNTR(2)
15025 FOR I=1 TO 50\IF I<10 THEN 15035
15026 F$='Y'
15030 REM  IF YO(I)<YO(I-1) THEN 15055
15035 PLOT(XO(I),YO(I))\MARK('+',XO(I),YO(I))
15040 IF I<Z5 THEN 15050\Z5=Z5+5
15045 CNTR(1)\COMM(' -',XO(I),YO(I))\PRINT I
15050 NEXT I
15055 GOSUB 3150\PRINT \PRINT TAB(10);'DATA FOR MODULUS CALCULATION'
15060 PRINT TAB(10);'MODULUS =';EO;' MPA';' USING REF POINTS';
15065 PRINT I7;' - ';I3
15070 CNTR(4)\GOSUB 8000
15075 RETURN
15900 REM        -*- DO DATA REDUCTION AGAIN ? -*-
16000 CNTR(3)\PRINT 'IS THIS MODULUS OK';\INPUT A$
16010 IF A$='Y' THEN RETURN

READY
```

Appendix B

TEST RESULTS OF SPECIMEN #1

```
INPUT STRAIN TRANSDUCER AMPLITUDE ?.02
INPUT LOAD TRANSDUCER AMPLITUDE (N) ?50000
INPUT SPECIMEN DIAMETER (MM) ?9.4
INPUT FREQUENCY (HZ)?1 3
INPUT PLASTIC STRAIN LIMIT ?.0015
INPUT STRESS SCALE (MPA) ?250
INPUT STRAIN SCALE ?.0035
INPUT YIELD STRENGTH (MPA) ?50
INPUT MATERIAL ?OFHCCOP
INPUT SPECIMEN # ?1
INPUT DATE ?1/03/87
INPUT YOUR INITIALS ?ZH
INPUT NUMBER OF CYCLES TO STOP(S?) ?50
```

FATIGUE TEST OF SPECIMEN #3 OF OFHCCOP
ZH 1/03/87

FREQUENCY = 1.3 PLASTIC STRAIN = 1.50000E-03
ELASTIC MODULUS = 120185 MPA
***** STRESS IN MPA UNITS
***** LOOPS RECORDED @ 0.1 HZ

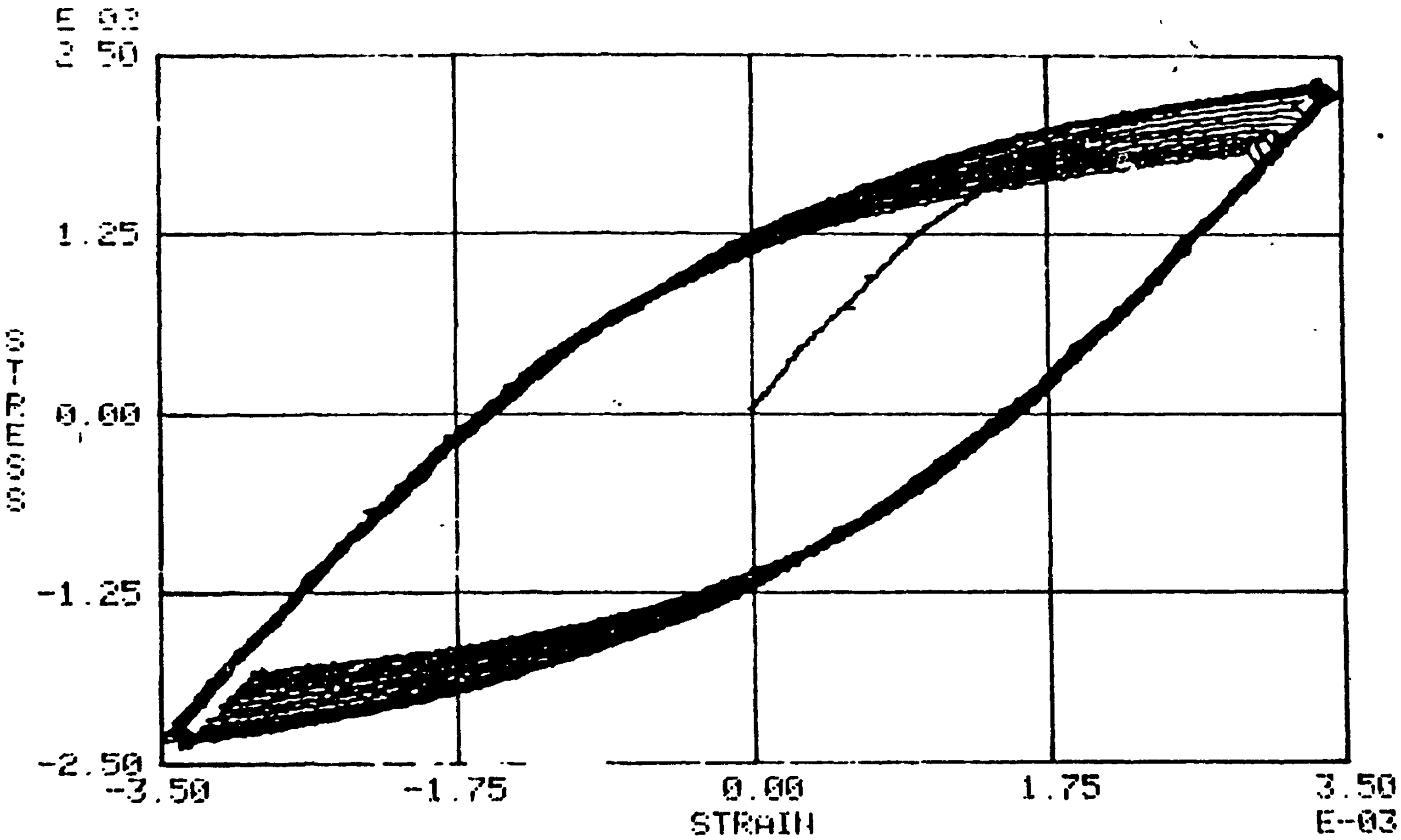

FATIGUE TEST OF SPECIMEN #3 OF OFHCCOP
ZH 1/03/87

FREQUENCY = 1.3 PLASTIC STRAIN = 1.50000E-03
ELASTIC MODULUS = 120185 MPA
STRESS IN MPA UNITS
LOOPS RECORDED @ 0.1 HZ

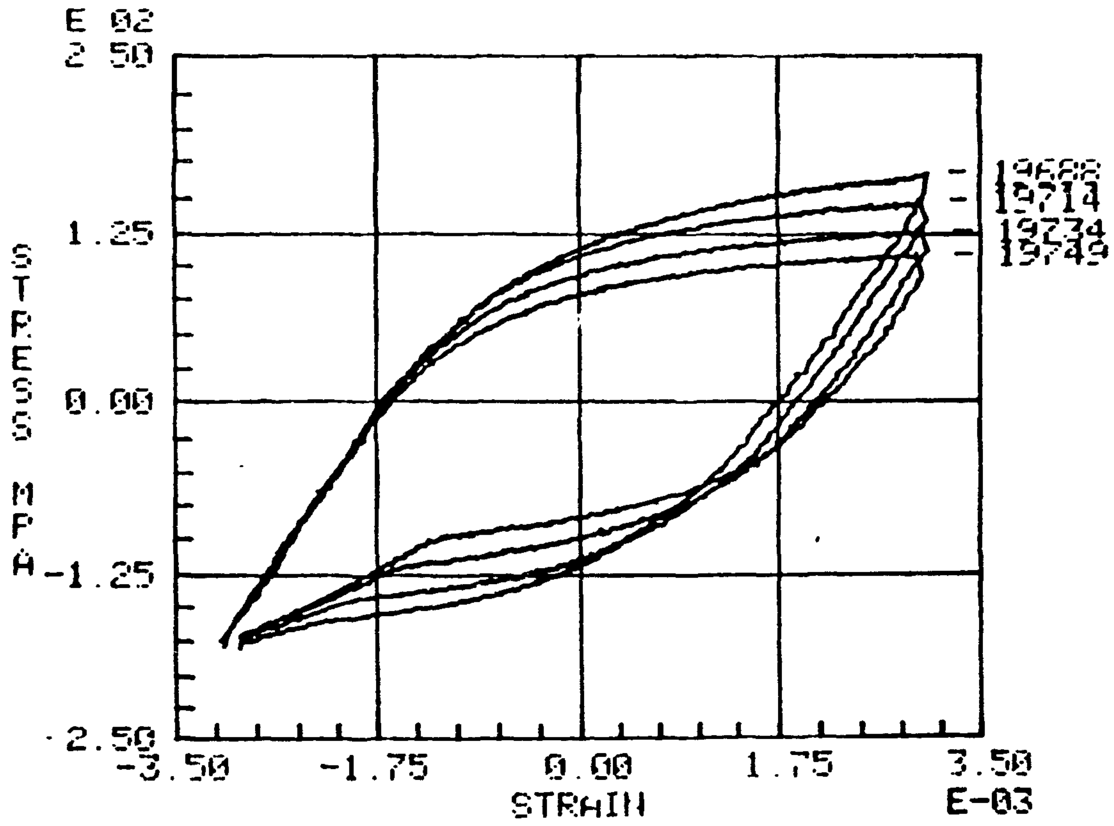

```
FATIGUE TEST OF SPECIMEN #3 OF OFHCCOP
                              ZH        1/03/87

FREQUENCY =  1.3    PLASTIC STRAIN =  1.50000E-03
ELASTIC MODULUS =  120185  MPA
***** STRESS IN MPA UNITS

DATA TAKEN @ 0.1 HZ

*************** AMPLITUDES **************--******** MEANS ********
CYC      STRAIN          STRESS         PL  STRAIN         STRAIN        STRESS
  1    3.47836E-03    230.188        1.56297E-03   -1.95408E-05  -5.27956
  2    3.48315E-03    235.116        1.52686E-03   -4.88525E-06  -1.05591
  3    3.48803E-03    236.172        1.52296E-03    9.77039E-06  -.703934
  4    3.46361E-03    235.468        1.50439E-03    4.88525E-06  -.351967
  5    3.51734E-03    235.644        1.55666E-03    0             -.527954
  6    3.53200E-03    235.996        1.56839E-03    4.88514E-06  -.175987
  7    3.53688E-03    235.468        1.57767E-03    0               0
  8    3.52711E-03    236.172        1.56204E-03    9.77039E-06  -.351974
 16    3.50757E-03    232.3          1.57471E-03    0             -.351974
 32    3.48803E-03    230.188        1.57274E-03    9.77039E-06   .351974
 64    3.43918E-03    224.557        1.57075E-03   -9.77039E-06   0
128    3.40498E-03    219.981        1.57462E-03    1.46556E-05  -1.40788
256    3.35125E-03    212.942        1.57946E-03    9.77039E-06  -.351967
512    3.29751E-03    207.486        1.57111E-03    1.46555E-05  -.879921
1024    3.27308E-03    202.383       1.58915E-03   -9.77039E-06  -1.05591
2048    3.22912E-03    198.335       1.57886E-03   -2.44259E-05  -1.58386
```

```
                    FATIGUE TEST OF SPECIMEN #3 OF OFHCCOP
                                           ZH        1/03/87

                    FREQUENCY =  1.3    PLASTIC STRAIN =  1.50000E-03
                    ELASTIC MODULUS =  120185  MPA
                    ***** STRESS IN MPA UNITS

                    DATA TAKEN @ 0.1 HZ

*************** AMPLITUDES ****************--********* MEANS ********
 CYC     STRAIN        STRESS      PL. STRAIN      STRAIN        STRESS
 4096  3.17538E-03  193 232   1.56759E-03    0               -1.05591
 8192  3.13630E-03  190.24    1.55340E-03    0               -.879929
 16384  3 12164E-03  186 544  1.56950E-03    1 46556E-05 - 703941

***** FAILURE PEAKS : DATA TAKEN @ 0.1 HZ
 CYC          *** STRESS ***                *** STRAIN ***
 19714       148.883  -178.801         3.12653E-03   -3.09722E-03
 19734       127.413  -177.393         3.15584E-03   -3.07767E-03
 19749       109.463  -177 393         3.16561E-03   -3.07767E-03
```

```
                 FATIGUE TEST OF SPECIMEN #3 OF OFHCCOP
                                   ZH        1/03/87

                 FREQUENCY =  1.3    PLASTIC STRAIN =  1.50000E-03
                 ELASTIC MODULUS =  120185  MPa
                 ***** STRESS IN MPa UNITS

                 DATA TAKEN @ THE SPECIFIED PL  STRAIN RATE

**************** AMPLITUDES ***************--******** MEANS ********
 CYC     STRAIN         STRESS       PL  STRAIN        STRAIN       STRESS
 12    3.48315E-03  233.356      1.54150E-03    4.39668E-05  0
 24    3.47338E-03  231.069      1.55077E-03   -4.88514E-06 -.527954
 48    3.43918E-03  227.021      1.55025E-03   -9.77039E-06 -1.40788
 96    3.40498E-03  221.389      1.56291E-03   -4.88514E-06 -1.40788
 192   3.38056E-03  215.23       1.58973E-03   -2.93113E-05 -1.58386
 384   3.31705E-03  210.302      1.56723E-03   -4.88525E-06 -.879929
 768   3.27797E-03  204.495      1.57647E-03   -4.88525E-06 -1.05592
 1536   3.23889E-03  199.039     1.58278E-03   -2.44260E-05 -1.2319
 3072   3.19492E-03  195.519     1.56810E-03   -1.95408E-05 -1.58386
 6144   3.16072E-03  190.768     1.57344E-03    2.44260E-05 -1.40788
 12288  3.10210E-03  187.248     1.54410E-03   -1.46555E-05 -1.40788
```

FATIGUE TEST OF SPECIMEN #3 OF OFHCCOP
ZH 1/03/87

FREQUENCY = 1.3 PLASTIC STRAIN = 1.50000E-03
ELASTIC MODULUS = 120185 MPA
***** STRESS IN MPA UNITS

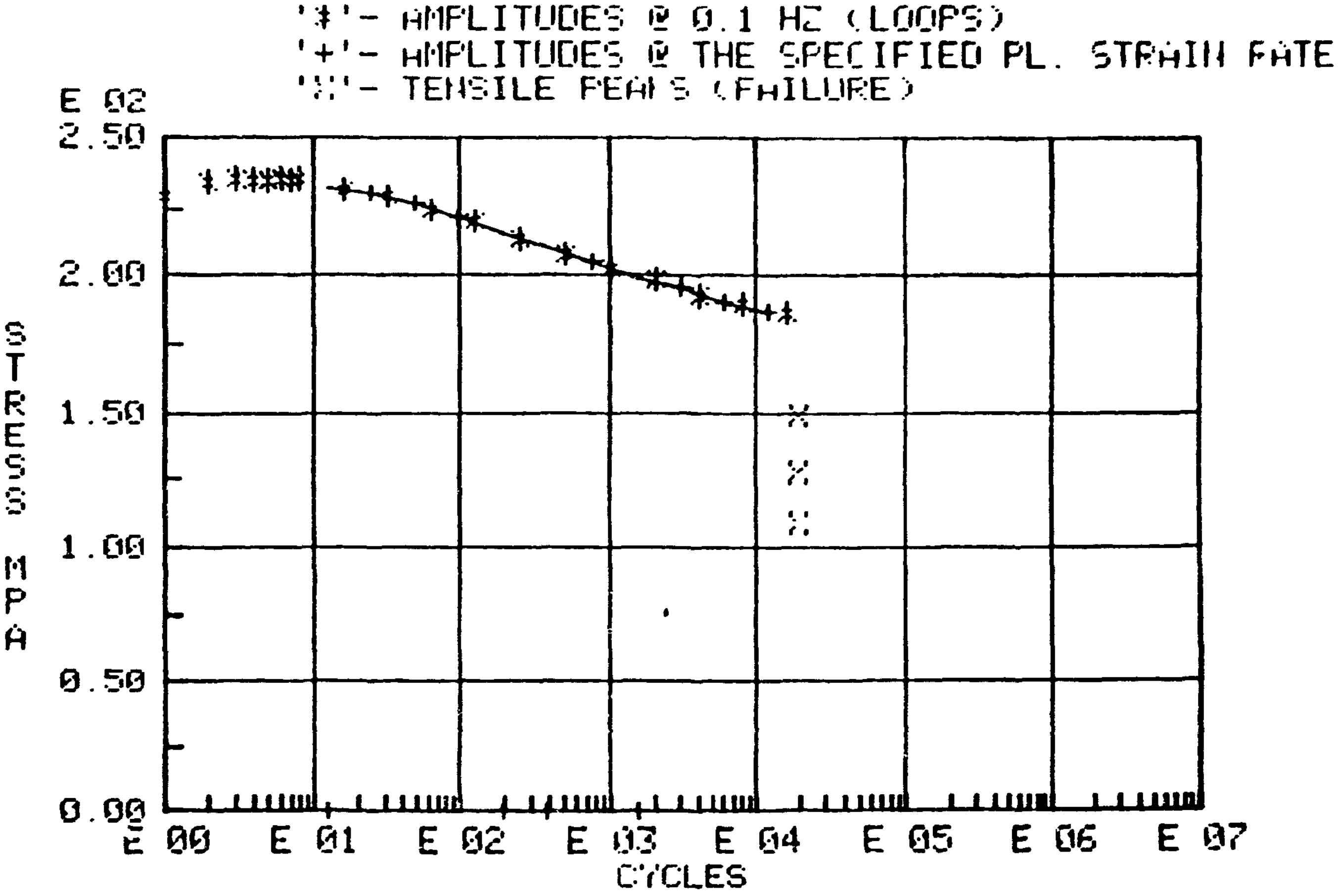

FATIGUE TEST OF SPECIMEN #3 OF OFHCCOP
ZH 1/03/87

FREQUENCY = 1.3 PLASTIC STRAIN = 1.50000E-03
ELASTIC MODULUS = 120185 MPA
***** STRESS IN MPA UNITS

'*'- AMPLITUDES @ 0.1 HZ (LOOPS)
'+'- AMPLITUDES @ SPECIFIED PL. STRAIN RATE

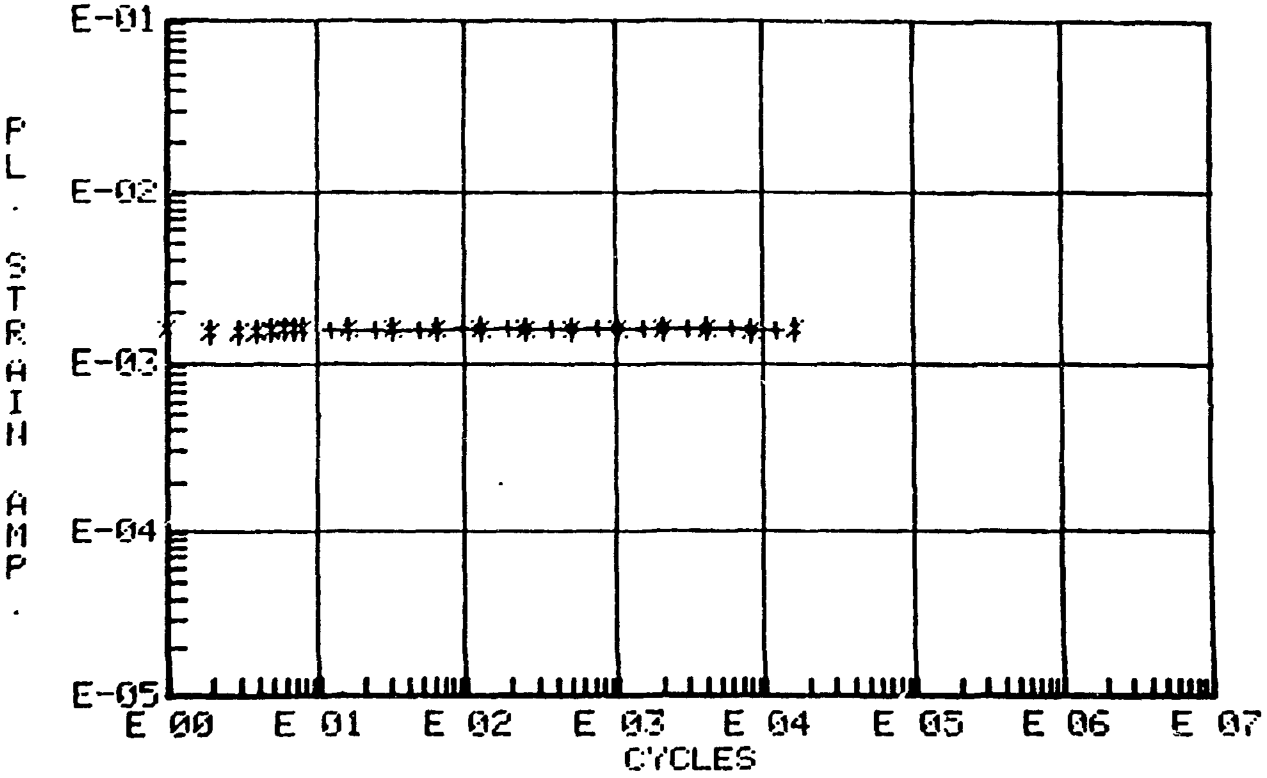

Appendix C

THE EXTIMATION OF ΔJ-INTEGRAL

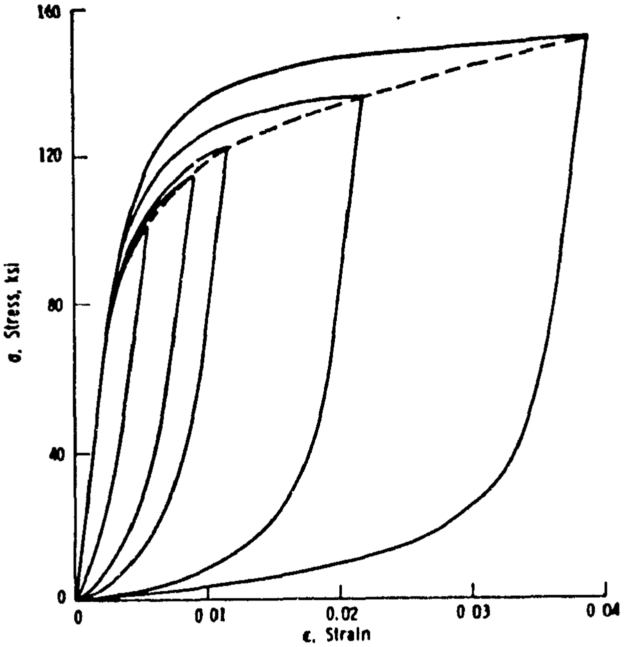

FIG 10—*Stress-strain hysteresis loops plotted on shifted axes*

In making this estimate, the linear elastic and exponential hardening plastic cases will be considered separately, and then combined for the more general elastic-plastic Ramberg-Osgood type of stress-strain behavior. These three idealized stress-strain relationships are illustrated in Fig. 19.

Consider the classical case of a crack in a wide plate remotely loaded in tension, Fig. 20*a*. The stress intensity is obtained [*23*] from the familiar expression

$$K = \sigma\sqrt{\pi a} \tag{2}$$

where σ = remote tension stress. Noting that the remote strain energy density, W, is given by the expression in Fig. 19*a*, Eqs 1 and 2 combine to give

$$J_{\text{elastic}} = 2\pi W a \tag{3}$$

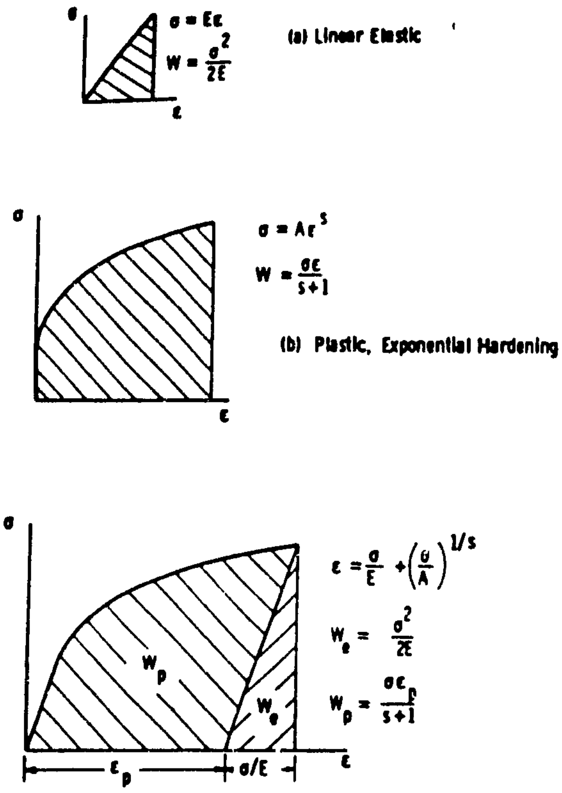

(a) Linear Elastic

(b) Plastic, Exponential Hardening

(c) Elastic-Plastic With Exponential Hardening

FIG. 19—*Three types of idealized stress-strain behavior.*

If the geometry of Fig. 20*a* is bisected to obtain a surface crack as in Fig. 20*b*, the stress intensity is elevated slightly [*23*]

$$K = 1.12\sigma\sqrt{\pi a} \tag{4}$$

Now consider the expression for an embedded circular crack [*23*]

$$K = \frac{2}{\pi}\,\sigma\sqrt{\pi a} \tag{5}$$

Again bisect to obtain a surface crack, in this case a half-circular surface crack, Fig. 20*c*. Note that this geometry approximates the geometry encountered in the laboratory tests, as long as the crack size is small compared to the specimen diameter. It is reasonable to assume that the surface correction factor of 1.12 implied by Eq 4 is at least approximately applicable here also, resulting in

$$K = 0.714\sigma\sqrt{\pi a} \tag{6}$$

The combined surface and flaw shape correction factor of 0.714 in Eq 6 must be squared to obtain the corresponding correction factor for J of 0.51. Applying this factor to Eq 3 gives

$$J_{elastic} = 3.2Wa \tag{7}$$

Rigorous J solutions for the exponential-hardening plastic case are not available for tension-loaded cracked members of infinite dimension. However, an estimate has

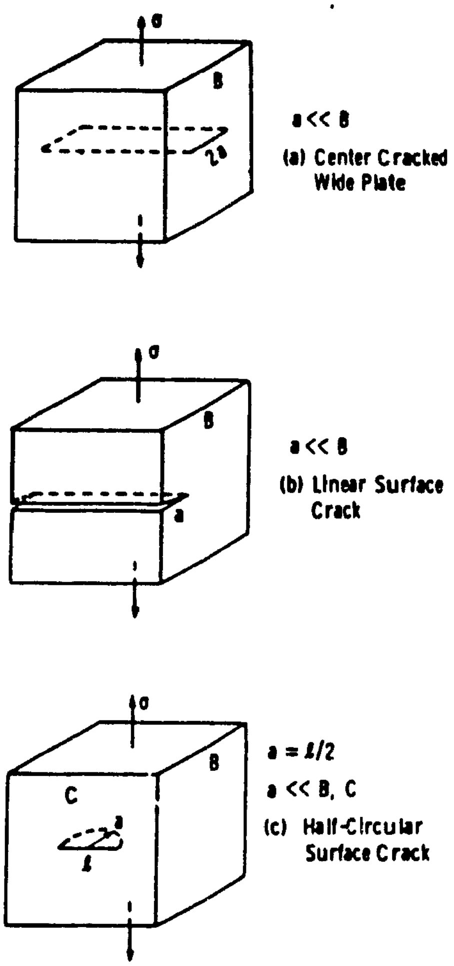

FIG. 20—*Various idealized crack geometries.*

been made by Shih and Hutchinson [*24*] for the geometry of Fig 20*a* under plane stress

$$J_{\text{plastic}} = 2\pi f(s)\; Wa \tag{8}$$

where $f(s)$ is a function of the strain-hardening exponent For $s = 0.165$ from Fig 1, the analysis of Ref *24* implies a value $f(s) = 1.56$ Note that J is still proportional to both the strain energy density and the crack size. To obtain an expression for the half-circular surface crack geometry of Fig 20*c*, assume that the combined surface and flaw shape correction factor of 0.51 used for the linear elastic case is applicable here also. Equation 8 is thus modified to give

$$J_{\text{plastic}} = 5.0\,Wa \tag{9}$$

An estimate qualitatively similar to Eq 9 was applied previously by Mowbray [*25*]

Consider the Ramberg-Osgood type elastic-plastic, stress-strain relationship, Fig 19*c*. The work of Shih [*26*] and also that of Shih and Hutchinson [*24*] suggests that J solutions for this case may be approximated by simply adding the separately computed elastic and plastic solutions. Equations 7 and 9 thus result in the following estimate of J for the half-circular surface crack geometry

$$J = 3.2\,W_e a + 5.0\,W_p a \tag{10}$$

where W_e and W_p = elastic and plastic components of the remote strain energy density, as illustrated in Fig. 19c.

For application to cyclic loading, it will be assumed valid to compute J for the loading portion of a cycle. The procedure used is illustrated in Fig. 17. Note that ranges of stress and plastic strain obtained from hysteresis loops such as those in Fig. 10 are used to compute the quantity here called ΔJ. The particular expression for ΔW_p which is shown depends on the assumption that hysteresis loop curves may be obtained by expanding the cyclic stress-strain curve with a scale factor of two, as indicated in Fig. 17 by the stress-strain equation involving primed quantities. If this assumption were valid for A533B, the dashed locus of loop tips line in Fig. 10 and all of the upper loop curves would fall together along a single line. However, this difficulty never affects the value of J by more than about 10 percent, and, in view of the fact that the J expression used is only an estimate, refinements in this area are inappropriate.

Note that the analysis [24] used as a basis for this estimate is for plane stress. A degree of approximation is thus involved in this regard also. The specimens tested were free to contract transversely so that the nominal plastic strain in any transverse direction was approximately half that in the axial direction. But a degree of constraint violating the plane stress assumption exists near the crack due to the strain being locally elevated there

Ideally, ΔJ should be computed only for that portion of the cycle during which the crack is open. An attempt was made to observe crack opening with a low-power microscope, but no well-defined opening event could be resolved. The only evidence available was the effect on the load versus deflection behavior of cracks that had grown relatively large near the end of the fatigue life. In such cases, stiffness changes indicating the closing and opening of the crack were observed only at high compressive loads. Thus, it was decided, as illustrated in Fig. 17, to use the entire compressive loading portion of the hysteresis loop in estimating ΔJ. Until additional experimental or analytical work clarifies the details of the crack closure effect, this uncertainty will exist in all fracture mechanics type approaches to the fatigue problem, including the familiar linear elastic approach

Thus, the method used in obtaining cyclic J involves approximations in several areas and can be regarded as a rough estimate only.

References

[23] Paris, P C and Sih, G C in *Symposium on Fracture Toughness Testing and its Applications, ASTM STP 381*, American Society for Testing and Materials, 1965, pp. 30-83.

[24] Shih, C. F. and Hutchinson, J W., "Fully Plastic Solutions and Large Scale Yielding Estimates for Plane Stress Crack Problems," Report No. DEAP-S-14, Division of Engineering and Applied Physics, Harvard University, Cambridge, Mass., July 1975.

[25] Mowbray, D. F. in *Cracks and Fracture, ASTM STP 601*, American Society for Testing and Materials, 1976, pp. 33-46.

[26] Shih, C. F. in *Mechanics of Crack Growth, ASTM STP 590*, American Society for Testing and Materials, 1976, pp. 3-26.